UNIVERSITY
OF OSLO

Bastian Zapf

Inverse mathematical modeling of solute transport in the human brain

Thesis submitted for the degree of Philosophiae Doctor

Department of Mathematics
Faculty of Mathematics and Natural Sciences

Department of Numerical Analysis and Scientific Computing
Simula Research Laboratory

2023

Series of dissertations submitted to the
Faculty of Mathematics and Natural Sciences, University of Oslo
No. 2629

ISSN 1501-7710

Cover: UiO.
Print production: Graphic Center, University of Oslo.

Preface

This thesis is submitted in partial fulfillment of the requirements for the degree of *Philosophiae Doctor* at the University of Oslo. The research presented here was conducted at the University of Oslo and at Simula Research Laboratory, under the supervision of Professor Kent-Andre Mardal as well as Geir Ringstad, Miroslav Kuchta and Simon Funke.

This work was supported by the Norwegian Research Council through grant 300305.

The thesis is a collection of three papers and a book chapter, presented in chronological order of writing. The common theme to the papers is the *inverse* modeling of human brain mechanics from magnetic resonance images using numerical optimization algorithms. The book chapter provides an in-depth technical description of some tools needed in this process. The papers are preceded by an introductory chapter that relates them to each other and provides background information and motivation for the work.

Acknowledgements

First and foremost, I would like to thank my supervisor Kent-Andre Mardal for the support and guidance during my work on the exciting problems that are now covered in this thesis. He was always available for discussing new ideas or problems and always made sure I had a good environment of collaborators to work with.

Next, I want to thank Johannes Haubner for his interest and tremendous support during the work on Paper I. He also invited me to join one of his ongoing research projects which led to Paper III. Working together on this project in Oslo and Salzburg was both interesting and instructive. It was a project with lots of drawbacks but crowned with great success in the end.

Also my co–supervisor Miroslav Kuchta contributed a lot during my work on this thesis, both with ideas and programming support, and I want to thank him for that.

I also want to thank my co–supervisor Geir Ringstad for improving my usage of medical terminology during our joint works. Discussing our mathematical results with him and Per Kristian Eide was always informative and added new perspectives to my thinking about the processes modelled in this thesis.

There are many technicalities to learn when starting to work with magnetic resonance images, and I am very thankful to Lars Magnus Valnes for always sharing his great expertise with me when I ran into a questions. I also want to thank Vegard Vinje and Marie E. Rognes for inviting me to present the results of our joint work in Paper II on several occasions.

Further, I would also like to thank my co–supervisor Simon Funke as well as Sebastian Mitusch for their contributions in the initial discussion during the work on Paper I. My colleagues Marius Causemann, Martin Hornkjøl, Florian Arbes and Marius Zeinhofer also contributed via various scientific and technical discussions during my work on this thesis.

Bastian Zapf
Oslo, June 2023

Abstract

Ten years ago, a new hypothesis for the development of neurodegenerative diseases was proposed. This hypothesis, known as the glymphatic system, suggests that a malfunction of fluid transport in the brain causes aggregation of toxic proteins in the brain and thereby causes diseases such as Alzheimer's disease. Today, the glymphatic system is understood as a physiologically regulated pathway by which cerebrospinal fluid (CSF) distributes molecules to and from the brain, but several aspects of this system are not yet understood. This includes the fundamental question if molecules are transported within the brain interstitium by diffusion or advection.

Contrast–enhanced medical imaging in rodents and humans has in the last ten years improved the understanding of molecular transport in the brain. Yet, determining the physical mechanism driving these processes only based on images has remained challenging. Given the potential significance of the glymphatic system in diseases, a substantially better understanding of the underlying fluid dynamics is urgently needed. Mathematical modeling bears the potential to enhance this understanding by providing quantitative tests of physiological hypotheses.

This thesis is concerned with uncovering the underlying physical laws of molecular transport in the human brain from novel medical imaging data sets. The data under consideration consist of time series of magnetic resonance images (MRI) taken after a tracer was injected intrathecally into the CSF of patients with various neurological diseases. Such time series reveal, in a qualitative way, how molecules are distributed from the CSF to the whole brain. Building on these data sets, this thesis performs both mathematical tests of concrete physiological hypotheses, and develops new numerical methods for such modeling.

Quantitative modeling requires quantitative data, and Paper IV of this thesis provides a systematic description of the methods needed to estimate the CSF tracer concentration from qualitative MRI. In Paper II, the methodology is applied to imaging data from 24 patients, and it is found that on average one quarter of the tracer enters the brain – demonstrating that injection of molecules into the CSF possibly represents an effective pathway to administer drugs to the brain.

This data is modeled by numerically solving partial differential equations (PDE) describing the diffusion of tracer in patient–specific brain geometries derived from the imaging data. The results show clearly that diffusion alone is insufficient to explain the tracer dynamics seen in the images. Hence, more advanced models including advection and degradation as well as dispersion of tracer in the brain are tested. These models contain several unknown parameters, and the method of PDE–constrained optimization is applied to determine these

from data specifically for each patient. This represents an ill–posed problem, but careful testing demonstrates the stability of the numerically determined transport parameters. It is found that a model including diffusion and advection as well as a model including enhanced diffusion and reaction results in reasonable agreement with the data. Again, these findings demonstrate that other transport mechanisms additional to diffusion play a significant role in molecular transport in the brain.

Numerical modeling of the brain's fluid dynamics has several drawbacks. Firstly, they can be computational expensive and thus limit progress in the research field. Secondly, patient–specific computational meshes describing the brain geometry need to be generated from MRI. This is both time–consuming and requires expertise.

To address both drawbacks at the same time, a new method combining artificial intelligence and PDE known as physics–informed neural networks (PINN) is applied in Paper I of this thesis. It is shown how to properly use the method to deal with challenges due to noise and temporal sparsity of the available images. When applied to the imaging data, the method finds that molecular transport appears faster than predicted by diffusion, supporting the results found with traditional numerical methods in Paper II.

This thesis also introduces an approach to simplify patient–specific mesh generation in Paper III by creating meshes for a new patient using a template mesh matching a template MRI. An image registration algorithm is introduced which deforms the template image such that it anatomically matches the image of the new patient. Numerical examples demonstrate that the image registration algorithm can also deform the template mesh to create a new mesh which matches the new patient. This represent a new, promising approach to reduce the manual work needed to perform computer simulations of the human brain.

In conclusion, this thesis has combined mathematical modeling and novel contrast–enhanced MRI from humans to assess which physical laws describe the transport of molecules in the human brain. The central finding is that diffusion alone is not sufficient to describe what is seen in the images. The computational and methodological advances made will enable efficient analysis of additional molecular transport mechanisms at play on data sets with higher resolution than used in this thesis. Thereby, this thesis contributes to an improved understanding of the fundamental processes underlying the movement of molecules in the human brain, both in health and disease.

Norwegian Abstract

For 10 år siden ble det lansert en ny hypotese om utviklingen av nevrodegenerative sykdommer. Denne hypotesen, kjent som det glymfatiske systemet, påstår at en feil i transport av hjernevæske fører til opphopning av giftige proteiner i hjernen og dermed forårsaker sykdommer som bl.a. Alzheimer's sykdom. I dag er det glymfatiske systemet definert som en fysiologisk regulert mekanisme som beskriver hvordan cerebrospinalvæske (CSF) fordeler molekyler i hjernen. Allikevel er grunnleggende spørsmål som hvorvidt molekyler transporteres gjennom diffusjon eller adveksjon inne i hjernen fremdeles ikke avklart.

Kontrastforsterkede medisinske bilder av rotter og mennesker har i de siste ti årene betydelig endret forståelsen av molekylærtransport i hjernen. Allikevel har det vært utfordrende å bestemme de fysiske mekanismene som driver de underliggende prosessene utelukkende fra bilder. Gitt den potensielle betydningen av det glymfatiske systemet i sykdomsutvikligen, er det et stort behov for å forbedre forståelsen av den underliggende væske–dynamikken. Matematisk modellering kan være behjelpelig med å gi kvantitative tester av fysiologiske hypoteser.

Denne avhandlingen handler om å avdekke de underliggende fysiske lovene for molekylær transport i menneskehjernen fra en ny type medisinske bilder. Disse bildene er tidsserier av magnetiske resonansbilder (MRI) som ble tatt etter at et kontrastmiddel har blitt injisert i CSF til pasienter med ulike nevrologiske sykdommer.

Slike tidsserier viser, på en kvalitativ måte, hvordan molekyler blir fordelt fra CSF til hele hjernen. Bygget på disse datasettene utfører denne avhandlingen matematiske tester av konkrete fysiologiske hypoteser og utvikler nye numeriske metoder for slik modellering.

Kvantitativ modellering krever kvantitative data, og Paper IV i denne avhandlingen gir en systematisk beskrivelse av metodene som trengs for å estimere konsentrasjonen av kontrastvæske fra kvalitative MRI. I Paper II blir metoden brukt på MRI fra 24 pasienter, og det blir funnet at gjennomsnittlig en fjerdedel av kontrastmiddelet går inn i hjernen – noe som viser at injeksjon av molekyler i CSF muligens representerer en effektiv vei for å administrere medisiner til hjernen.

Disse dataene modelleres ved å løse partielle differensialligninger (PDE) som beskriver spredning av kontrastvæske i pasientspesifikke hjernegeometrier som er laget fra MRI. Resultatene viser tydelig at diffusjon alene er utilstrekkelig for å forklare det som sees i bildene. Derfor blir mer avanserte modeller som inkluderer adveksjon og nedbrytning, samt spredning av kontrastvæske i hjernen, testet.

Disse modellene inneholder flere ukjente parametere, og PDE–constrained

optimalisering blir brukt for å bestemme de fra bildene for hver pasient. Dette representerer et matematisk sett dårlig stillt problem, men grundig testing viser stabiliteten av de numerisk bestemte transportparametrene. Det blir funnet at en modell som inkluderer diffusjon og adveksjon, samt en modell som inkluderer økt diffusjon og reaksjon, gir god overensstemmelse med dataene. Igjen viser disse funnene at andre transportmekanismer, i tillegg til diffusjon, spiller en betydelig rolle i molekylærtransporten i hjernen.

Numerisk modellering av hjernens væskedynamikk har flere ulemper. For det første kan de være beregningsmessig kostbare og dermed begrense fremgangen innen forskningsfeltet. Videre må pasientspesifikke geometrier som beskriver hjernen genereres fra MRI. Dette er både tidskrevende og krever ekspertise.

For å takle begge ulempene samtidig, brukes det en ny metode som kombinerer kunstig intelligens og PDE kjent som physics–informed neural networks i Paper I i denne avhandlingen. Det blir vist hvordan man kan bruke metoden til å håndtere utfordringene som forårsakes av støy og dårlig oppløsning i tid av de tilgjengelige MRI. Når metoden blir brukt på MRI, finner den at molekylær transport ser ut til å være raskere enn ved bare diffusjon, og støtter derfor resultatene som ble funnet med tradisjonelle numeriske metoder i Paper II.

For det andre introduserer denne avhandlingen en ny tilnærming for å takle den tidligere nevnte begrensningen med pasientspesifikk geometrier i Paper III. Her lages det geometrier for en ny pasient ved hjelp av en målgeometri som matcher en mål–MRI. For å oppnå dette introduseres det en ny bilde–registreringsalgoritme som deformerer målbildet slik at det anatomisk matcher bildet av den nye pasienten. Numeriske eksempler viser at algoritmen også kan deformere målgeometrien for å lage en ny geometri som matcher den nye pasienten. Dette representerer en ny og lovende tilnærming for å forenkle det tekniske arbeidet som kreves for å utføre simulering av menneskehjernen.

For å konkludere, har denne avhandlingen kombinert matematisk modellering og ny kontrastforsterket MRI fra mennesker for å vurdere hvilke fysiske lover som beskriver transporten av molekyler i hjernen. Det ble funnet at diffusjon alene ikke er tilstrekkelig for å beskrive det som sees på bildene. Dette indikerer at andre molekylære transportmekanismer spiller en betydelig rolle og åpner opp for det interessante forskningsproblemet av å bestemme de fra data med høyere oppløsning enn det som ble analysert i denne avhandlingen. Dermed vil metodene utviklet i denne avhandlingen bidra til en bedre forståelse av de grunnleggende prosessene som ligger til grunn for bevegelsen av molekyler i hjernen hos både friske og syke personer.

List of Papers

Paper I

Bastian Zapf, Johannes Haubner, Miroslav Kuchta, Geir Ringstad, Per Kristian Eide, Kent-Andre Mardal "Investigating molecular transport in the human brain from MRI with physics-informed neural networks". In: *Scientific Reports*, September 2022, volume 12, issue 1, pp. p.15475-15475. DOI: 10.1038/s41598-022-19157-w.

Paper II

Vegard Vinje, Bastian Zapf, Geir Ringstad, Per Kristian Eide, Marie E. Rognes, Kent-Andre Mardal "Human brain solute transport quantified by glymphatic MRI-informed biophysics during sleep and sleep deprivation". Submitted for publication.

Paper III

Bastian Zapf, Johannes Haubner, Lukas Baumgärtner, Stephan Schmidt "Medical Image Registration using optimal control of a linear hyperbolic transport equation with a DG discretization". Submitted for publication.

Paper IV

Bastian Zapf, Lars Magnus Valnes, Kent-Andre Mardal "Quantifying cerebrospinal fluid tracer concentration in the brain". Under revision for *MRI2FEM II: from magnetic resonance images to computational brain mechanics*, Simula Springer Briefs on Computing

Contents

List of Figures

List of Acronyms

ADC Apparent diffusion coefficient

CG Continuous Galerkin method

CSF Cerebrospinal fluid

DG Discontinuous Galerkin method

DTI Diffusion tensor imaging

ECS Extracellular space

FEM Finite element method

gMRI Glymphatic magnetic resonance imaging

GPU Graphics processing unit

iNPH Idiopathic normal pressure hydrocephalus

ISF Interstitial fluid

MRI Magnetic resonance image

PDE Partial differential equation

PINN Physics-informed neural network

PVS Perivascular space

Chapter 1

Introduction

1.1 Motivation and aim

Alzheimer's disease is the most common form of dementia and affected an estimated 55 million people world–wide in 2021 [56]. This figure is expected to grow rapidly due to demographic change and increasing life expectancy in developing countries. Also, the disease is considered to be one of the most expensive for society [56]. The disease is incurable [99] and currently only two drugs, with limited efficacy to slow down cognitive decline, have been approved [106, 152, 183]. These drugs reduce the concentration of protein aggregates of Amyloid–β found in the brain of Alzheimer patients [164]. According to the "Amyloid hypothesis", the aggregation of Amyloid–β in the brain is the cause of the disease [57, 162], but it has been debated whether it is truly the cause or merely an effect of the disease [133, 164].

Results from diverse imaging studies in recent years suggest that the aggregation of these proteins may be secondary to a disturbance of the cerebrospinal fluid (CSF) pathways in the brain [75, 128, 146, 176]. The currently dominant model for the dynamics and roles of CSF in brain homeostasis is the "glymphatic system" [75, 145]. It describes a brain-wide, physiologically regulated pathway by which CSF distributes molecules to and from the brain along perivascular spaces, CSF–filled spaces that surround the brain vasculature.

A decade after its initial description [75], several aspects of the glymphatic system are still being actively investigated [2, 70, 112]. Given the significance of the glymphatic system in brain homeostasis [21, 98, 127] and as a potential drug administration pathway [98], it is clear that a more detailed understanding is urgently needed.

This thesis aims to contribute to a better understanding of molecular transport in the human brain from two different angles:

(a) Firstly, by applying mathematical methods to test physiological hypotheses about molecular transport in the human brain.

(b) Secondly, by developing and exploring new methods and tools to simplify future modeling studies.

The methods are applied to unique data sets of CSF tracer–enhanced magnetic resonance images (MRI) acquired in clinical studies at the Oslo University Hospital in Oslo, Norway [45, 159]. In detail, this thesis is concerned with physics–based models in the form of partial differential equations (PDE). These models can be broadly categorized into two categories, namely *forward* and *inverse* models. Forward modeling, e.g., [5, 14, 16, 71, 83] in the context of the glymphatic system, requires that all model parameters are defined precisely.

Then, the model yields a definite prediction which can be compared to clinical data to test physiological hypotheses as in, e.g., [30, 72, 179].

In inverse modeling, one seeks to determine *unknown* model parameters such that the prediction is in correspondence with the data. Within the context of brain solute transport modeling, this approach has been used substantially less than forward models, exceptions are two studies with imaging data from humans [47, 182] and optimal mass transport in rodents [22, 90, 147]. This might be because inverse models can be computationally more expensive or more effortful to implement than forward models.

To address aim (a), this thesis applies inverse mathematical modeling to quantify the relative importance of different solute transport mechanisms in the human brain from MRI (Paper I and Paper II). In detail, the aim is to determine unknown parameters in different physics–based models that may describe the dynamics of molecules on the macroscopic scale. By providing a way of testing physiological hypotheses, such quantitative parameter estimates may contribute to an increased understanding of solute transport in the brain from a modeling point of view.

The modeling performed in both papers relies on high–quality brain meshes. While tools for generating subject–specific meshes from MRI exist, in some cases, manual corrections or labelling are needed when creating advanced meshes (e.g., including the subarachnoid space and ventricular system). Even with knowledge of the processing software, this can be a time–consuming task. This issue motivates aim (b) which is addressed in Paper I and Paper III in this thesis.

Paper I explores the applicability of a new mesh-free method combining machine learning and PDE as an alternative to the traditional methods used in Paper II. Paper III takes a different angle at the problem and proposes a new approach to generate brain meshes. Finally, the technical aspects discussed in this thesis are not limited to the brain meshing issue. Working with CSF tracer enhanced MRI comes with many subtleties, and Paper IV aims to simplify the workflow from raw images to quantitative data that can be used for modeling.

The remainder of this introduction provides a compact overview of previous research on which this thesis builds upon, and is organized as follows. First, Sections 1.2 and 1.3 give a short description of the current understanding of the cerebrospinal fluid and the glymphatic system. Secondly, an overview of glymphatic system imaging studies, with a focus on MRI, is presented in Section 1.4. Mathematical models of various aspects of the glymphatic system are reviewed in Section 1.5, and the numerical methods used in this thesis are introduced in Section 1.6.

A summary of the papers collected in this thesis is given in Section 1.7 and Section 1.8 provides a comparison of some aspects of the papers. A conclusion of the results is given in Section 1.9. Some possible implications of the findings are discussed in Section 1.10. Finally, Section 1.11 outlines future perspectives and research possibilities.

1.2 The human brain and the cerebrospinal fluid

The brain of all vertebrates is surrounded by a colorless, water–like fluid called cerebrospinal fluid (CSF) [102]. CSF consists of 99 % water and has some ions dissolved in it [149]. It provides buoyancy to the brain [172] and protects it from traumatic injuries [34]. As proposed already in the nineteenth and twentieth century [28, 114, 131, 145] and recently by the glymphatic model, the flow of CSF in the brain plays a crucial, lymph–like, role in brain health. A historical review of the study of the CSF, dating back as early as 3000–2500 BC, can be found in [34, 68, 145].

A sagittal slice of the human head is illustrated in Fig. 1.1A. The skull, the CSF and the meninges protect the brain. The meninges are three membranes, called the dura mater, the arachnoid membrane, and the pia mater. They encase the brain and the spinal cord[1]. The space between the arachnoid membrane and the pia mater is filled with CSF and is called subarachnoid space and is shown in Fig. 1.1A.

CSF is produced at a rate of 0.4–1 l per day [145], mainly in the choroid plexus in the ventricular cavities [17] in the center of the brain. The total CSF volume amounts to 90–150 ml in the human central nervous system (the brain and the spine) [17]. This implies that the CSF is replaced several times a day [34] and one or several drainage pathways have to exist.

The classical view of the CSF movement is known as the "third circulation" and goes back to the 20th century to the famous neurosurgeon Harvey Cushing [29]. According to this view, the CSF circulates in a unidirectional manner from the choroid plexus to the top of the head. It leaves the ventricles through the foramen of Magendie and Luschka to the cisterns [144, 145] as shown in Fig. 1.1A). From there, it flows further through the subarachnoid space to be absorbed into the venous sinuses through structures called *arachnoid villi* or *arachnoid granulations* at the top of the head [17] as shown in Fig. 1.1.

This view has been challenged by various experimental observations and is addressed in a large body of literature, e.g., [17, 89, 114, 132, 172]. The dynamics of CSF are presumed to be much more complex than the traditional view [140, 144, 172]. For example, phase–contrast MRI has shown that there is also a pulsating movement of CSF due to heartbeat and breathing [49, 58, 173]. Furthermore, other routes for drainage of CSF such as through the cribriform plate into the nasal cavity, as illustrated in Fig. 1.1A, have been observed. Another suggested drainage pathway is via the recently discovered meningeal lymph nodes [6, 100] in the dura mater [144] illustrated in Figs. 1.1B. The relative importance of these pathways is yet to be determined, but today outflow via the arachnoid granulations, as proposed in the "third circulation", is presumed to be of minor importance due to lack of evidence [140, 145].

[1] It has recently been proposed that a fourth membrane exists [122], but not without controversy (see also the response letters to the article [122]).

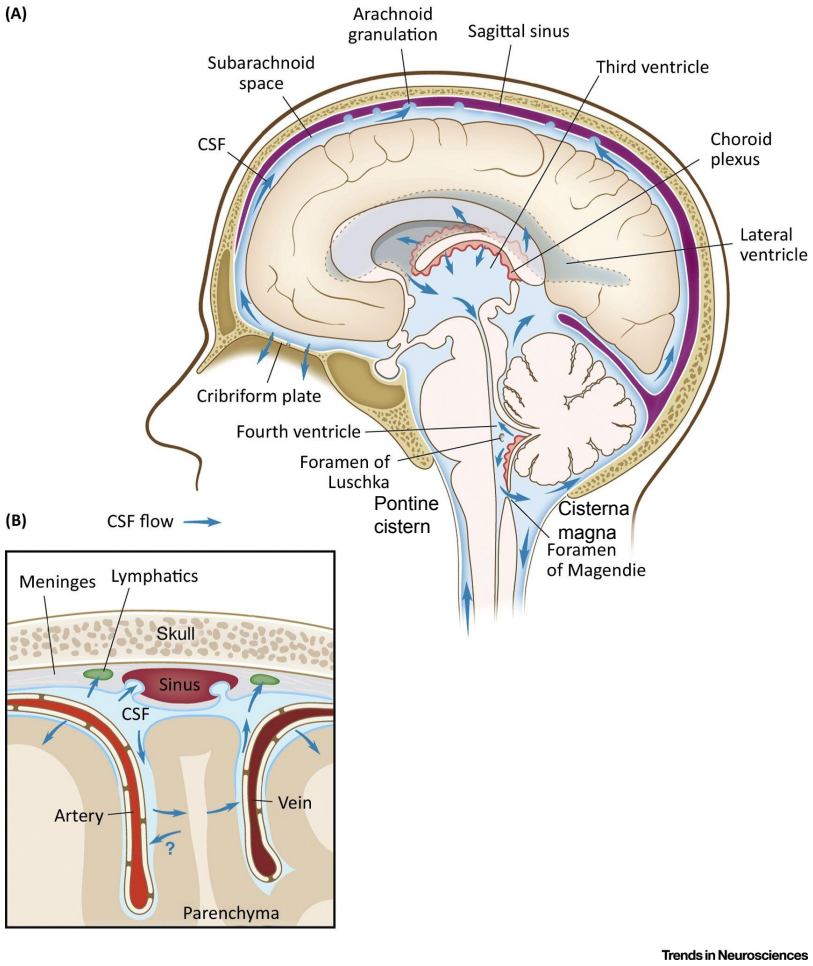

Figure 1.1: Fig A. Sagittal sketch of the human head. According to the classical hypothesis, CSF is produced in the choroid plexus, flows in a unidirectional manner to the top of the head and is absorbed into the sagittal sinus. The figure also indicates another outflow route for CSF via the cribriform plate into the nasal cavity. Fig. B illustrates two possible drainage pathways for CSF. Firstly, from the subarachnoid space to the sagittal sinus via arachnoid granulations and, secondly, to the meningeal lymphatics in the dura. Fig. B also illustrates an important aspect of the glymphatic concept. Namely, CSF enters and exits the brain parenchyma from perivascular spaces (CSF–filled spaces around penetrating arteries and veins). Reprinted from Trends in Neurosciences, Volume 39, Raper *et al.* "How Do Meningeal Lymphatic Vessels Drain the CNS?", Pages No. 581-586, Copyright (2016), with permission from Elsevier. Labels "Pontine Cistern" and "Cisterna Magna" added.

In summary, the knowledge of CSF dynamics and efflux pathways is still limited. Due to the critical role of CSF in brain health, a better understanding of CSF and the mechanisms by which it transports molecules is needed. The methods developed and used in this thesis represent a promising approach to contribute to this understanding, c.f. also the discussion in Section 1.11.

1.3 Molecular clearance in the brain

In the human body, byproducts of cell metabolism are cleared by the lymphatic system [149]. Fluid leaks through the blood vessel walls and slowly moves through the tissue, thereby collecting metabolic waste. It is then absorbed by lymphatic vessels present in the tissue, delivered to the venous circulation and finally cleared in the liver and kidneys [149].

In the brain, the blood–brain barrier (BBB) controls the exchange between molecules dissolved in brain fluids and the blood to protect the brain [145, 149]. Furthermore, there are no lymphatic vessels in the brain [149]. How then is the brain cleared from byproducts of the cell metabolism that accumulate in the brain extracellular space (ECS)? Given that the brain is responsible for around 20 % of the body's metabolism at rest [7], despite only making up 2 % of the body mass, there have to be other mechanisms to remove metabolic byproducts.

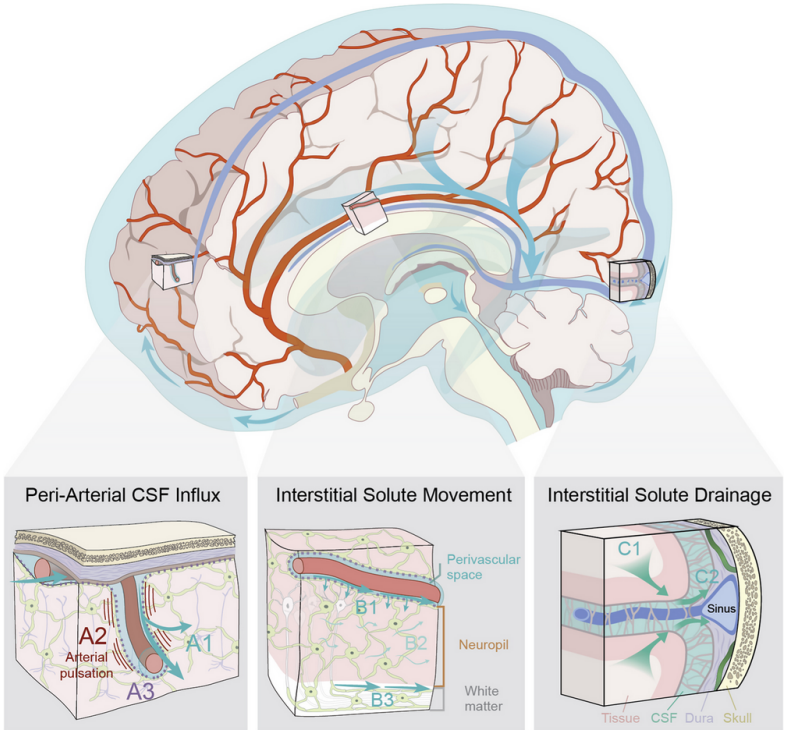

Figure 1.2: The illustration shows key components of the glymphatic system: CSF enters into the brain parenchyma along periarterial spaces. CSF mixes with the ISF, and clears out metabolic waste from the interstitium via perivenous spaces to the subarachnoid space. The image is taken from [86] and reprinted under the CC BY-NC-ND 4.0 license [25].

Given the importance of this question, it is not surprising that much research on this topic has been conducted. An in–depth literature review of fluid transport in the brain exceeds the scope of this introduction. This section will instead give a description of the "classical" concept of fluid transport in the brain and relates it to the recently popularized concept of the glymphatic system. The interested reader is referred to a selection of recent reviews [2, 12, 70, 80, 85, 86, 112, 113, 145, 149].

It was traditionally presumed that molecules in the ECS are removed by several means, including degradation due to intra– and extra–cellular mechanisms as well as transport across the BBB with the help of specialized transporters [149]. In addition, it has long been thought that the CSF acts as a sink for excess proteins [32, 149]. The transport of molecules in the ECS to the CSF has classically been thought to be a diffusive process [1, 32, 145]. The ECS is filled with interstitial fluid (ISF), a water–like fluid which fills the space between cells in the brain interstitium, which is chemically indistinguishable from CSF [85]. Hence, it was presumed that molecules diffuse in the ISF to enter the CSF outside the brain parenchyma. There, molecular transport was presumed to happen via fluid flow along various preferred routes in the brain (cf. [70] and refs. therein). These routes include perivascular spaces (PVS), white matter tracts and other spaces in the brain [70]. Perivascular spaces are angular, CSF–filled spaces between the brain vasculature and the end–feet of astrocytic glial cells [187]. They are illustrated in Fig. 1.2.

However, some results from tracer studies in animals conflict the theory and in contrast suggest that movement of the tracer in the brain is faster than what can be explained solely by diffusion, e.g., [26, 156]. Efflux of tracers was found to occur at a rate independent of the molecular size of the tracer. This is in conflict with the Sutherland–Einstein equation predicting an inverse relation between diffusion coefficient and molecule size [174]. Further, these experiments suggest that transport outside of the ECS seems to happen mainly along preferred routes that follow the vasculature [12, 119, 189].

In 2012, in a series of papers reporting new experiments with novel imaging data with rodents, Jeffrey J. Iliff and Maiken Nedergaard combined these past findings into a new concept for fluid flow in the brain, which they termed the "glymphatic system" [75, 76]. In its initial formulation [75, 127], this concept is summarized as follows:

1. There is inflow of CSF along PVS, in the same direction as blood flow, driven by arterial pulsation.

2. From the PVS, the CSF enters the ECS through astrocytic end–feet and mixes with the ISF.

3. Metabolic waste in the ECS is cleared by advection due to fluid flow from penetrating arteries to veins.

4. Waste is removed from the brain by movement of CSF along the paravenous spaces.

5. By the various CSF drainage pathways, the waste is then transported to the kidney and liver.

The influx of CSF to the brain was found to be strongly dependent on the expression of the water transporter aquaporin–4 in the end–feet of glial cells defining the PVS. The name hence indicates that this mechanism of circulation and exchange of CSF and ISF represents a glial–dependent (g) lymphatic–like clearance system for the brain.

Another key concept of this system is that it is particularly active during sleep in rodents [23, 193] and in humans [41, 45]. Given that sleep quality and hence glymphatic activity declines with aging, the glymphatic concept offers a fluid–mechanical explanation for the build–up of toxic protein aggregates seen in the brain in many age–related neurological diseases [13, 128].

Several aspects of the glymphatic system have been or still are controversial [70, 86, 113, 172]. For example, several experimental results [161, 169, 170] and modeling studies [86] question the existence of bulk flow in the interstitium or even the PVS [5]. There is also evidence for transport of molecules in the PVS in and against the direction of blood flow [70].

As of 2022, more than 1,000 papers, both experimental and modeling studies, have been published on the glymphatic system [86] and several of its aspects have been refined [86, 145]. Transport in PVS is still presumed to be advective in the glymphatic model. The idea of advective transport in the interstitium has been moderated; transport is thought to be both diffusive and advective, with diffusion likely making the greater contribution [86]. The relative importance of both mechanisms is not yet determined but is considered an important question in the field. For example, a review of fluid transport in the brain [85] published in 2023 summarizes open questions, and one of them reads:

> "What are the relative contributions of advection and diffusion in the ISF in the ECSs?"

Similarly, among the open questions discussed in [112], one reads:

> "Can ISF clearance routes be further elucidated using emerging brain-wide imaging technologies? Specifically, can noninvasive MRI of fluid movements serve as a platform for the assessment of glymphatic function in the clinic?"

1.4 Imaging brain clearance

The initial description of the glymphatic system was based on imaging studies in rats using *in vivo* two–photon microscopy as well as *ex vivo* fluorescence imaging [75]. In the subsequent years, *in vivo* imaging of rodents using MRI [14], PET[12] and other techniques [12, 86] have helped to refine the understanding of the glymphatic system. In humans, MRI is the major means of investigating glymphatic function. This will be covered in more detail in Subsections 1.4.1 and 1.4.2.

Most of the imaging of the glymphatic system in both animals and humans is based on injecting tracers, either into the CSF or the blood [12, 86]. In general, tracers are not a surrogate marker for CSF, but rather for transport of molecules via the CSF and their influx and efflux from the brain. However, when interpreting tracer-enhanced images, it should be kept in mind that the molecules of interest in the context of neurological diseases (Amyloid–β, tau, α–synuclein) can be much larger than tracers. Still, in absence of other techniques, tracer–enhanced MRI is an effective tool to study various aspects of the glymphatic system in humans. For example, it enables observing *in vivo* the drainage of tracers to lymph in the head [3, 44].

Tracer–enhanced *ex vivo* imaging techniques such as light sheet microscopy in pigs [11] or fluorescence microscopy in rats [194] have also been used. Due to artifacts induced by death and tissue processing, *in vivo* imaging techniques represent the main means of studying the glymphatic system [98]. An overview of the benefits and challenges of the imaging methods currently in use can be found in recent reviews [12, 98, 123].

This thesis is concerned with CSF tracer–enhanced MRI in humans [158, 159]. The MRI terminology relevant to this thesis is introduced in subsection 1.4.1. Tracer–enhanced MRI, with a focus on the human brain, is covered in Subsection 1.4.2. Finally, Subsection 1.4.3 gives an exposition of the disease that the patient analyzed in Paper I was diagnosed with: idiopathic normal pressure hydrocephalus, currently the only form of dementia that is partially reversible.

1.4.1 Magnetic resonance imaging

The technical development of magnetic resonance imaging goes back to the work of Paul Lauterbur and Peter Mansfield in the 1970s. In 2004, they were awarded the Nobel prize in medicine for their contributions [38]. Today, MRI is a clinically well–established, non–invasive tool which yields many different types of 3–D images ("modalities"). This thesis uses data from structural as well as diffusion–weighted MRI, but other modalities such as functional MRI (which images neuronal activity) have also been used in the study of the glymphatic system [54, 88].

Structural imaging makes use of the fact that different types of tissue are characterized by different values of the nuclear spin relaxation times T_1 and T_2 [137]. Two common types of structural types of images are the so–called T_1– and T_2–weighted images. Exemplary slices from T_1– and T_2–weighted images are shown in Fig. 1.3. The intensity in the image voxels is determined (a) by the type of tissue in the voxel and (b) by the MRI sequence used to acquire the image.

In T_1–weighted images, the sequence parameters are chosen such that the MR signal becomes approximately proportional to the inverse of T_1 [48]. White matter, for example, is characterized by shorter T_1 compared to gray matter due to its higher fat content and hence appears brighter in T_1–weighted images [48]. Therefore, these images display a good contrast between white and gray matter.

In T_2–weighted images, on the other hand, the signal becomes approximately inversely proportional to T_2. The T_2 value is comparable in white and gray matter but much higher in CSF, and hence, these images give a good contrast between tissue and fluid [48].

The work presented in this thesis also utilized data from two different MRI modalities, namely T_1–maps [177] and diffusion tensor images (DTI) [171]. These are distinguished from structural images such as T_1– and T_2–weighted images (voxel values correspond to dimensionless signal intensities) by the fact that the voxel values are quantitative measures of physical variables.

In T_1–maps, the voxel values are measures of the relaxation time T_1, typically of the order of a second in brain tissue [48]. This modality is very important in the context of CSF tracer imaging, since it directly allows to compute the CSF tracer concentration from the image, cf. also the more detailed description in Paper IV. An exemplary T_1–map is shown in Fig. 1.3. Despite the resolution being lower as compared to the T_1–weighted image, it can be seen that the T_1 values are lower in the white matter (which appears darker in this type of image) as compared to gray matter.

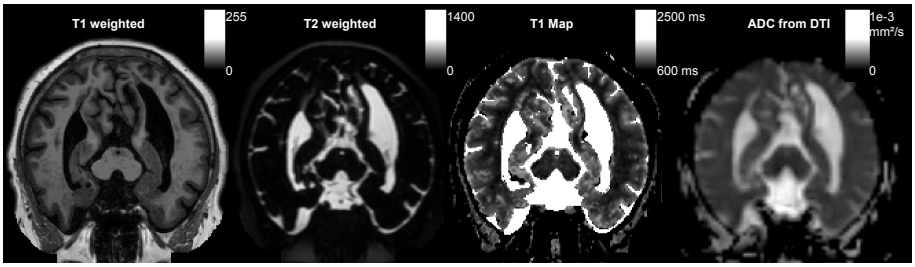

Figure 1.3: Coronal slices from MRI of a patient from [159] obtained with different MRI modalities.

The DTI technique measures the diffusivity of water as a 3×3 tensor for water in every voxel. This allows to compute other quantities such as the mean or apparent diffusion coefficient (ADC) [108] as shown in Fig. 1.3. It can be seen in the image that the ADC is highest in the CSF–filled ventricles, which is to be expected since molecules can diffuse unhindered in all directions there. The resolution is typically lower than in T_1–images, but still, DTI is valuable for the modeling presented in this thesis. From DTI, the diffusion tensor or mean diffusion coefficient for CSF tracers in the brain can be estimated [129, 182]. In Paper I, we compare our modeling results to this estimate in order to quantify the importance of diffusive and advective transport in the brain. Paper II takes an alternative approach and uses the DTI estimates to perform simulations in a subject–specific manner.

DTI has also been applied outside the context of PDE–based modeling to study the glymphatic system. For example, DTI has shown that fluid movement is enhanced along PVS and significantly affected by heartbeat [66]. The significance of sleep for glymphatic transport is supported by a study showing that apparent

diffusion coefficients increase in sleeping humans [35]. Decreased diffusivity along PVS was also observed using DTI in humans with neurological diseases as compared to controls [74, 175, 196], supporting the possible role of glymphatic malfunction in disease development.

The resolution of MRI increases with magnetic field strength, but this comes with drawbacks such as higher energy transfer to the tissue [91]. In the context of MRI studies of fluid transport in the brain, image resolutions of data reported in the literature are in the range $0.001\,\mathrm{mm}^3$–$0.027\,\mathrm{mm}^3$ in rodents and $0.5\,\mathrm{mm}^3$–$1\,\mathrm{mm}^3$ in humans [12]. This resolution is an important aspect to keep in mind when interpreting the modeling results presented in this thesis, because it implies that perivascular spaces can not be distinguished from the interstitium in the MRI that are being used in Paper I and Paper II.

This thesis makes extensive use of the freely available human brain MRI processing software FreeSurfer [52]. Among other things like image registration [157], FreeSurfer provides automated segmentation from T_1–weighted MRI into anatomical regions as well as 3–D brain surfaces. The software can also make use of the high contrast between tissue and fluid in T_2–weighted images to increase the quality of the generated brain surfaces. Figure 1.4 shows these surfaces and the automatic segmentation for an example subject. The use of FreeSurfer in this thesis is discussed in greater detail in Paper III and Paper IV.

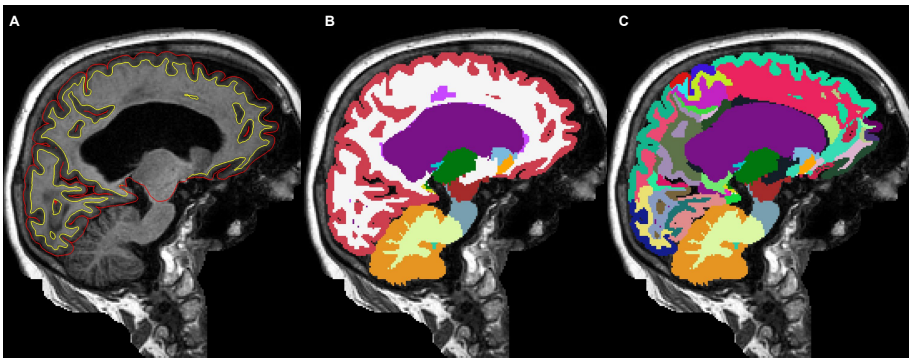

Figure 1.4: Sagittal slices (defaced) from MRI of a patient from [159] displaying the pial (red) and white matter (yellow) surfaces (A), brain segmentation (B) and white matter refined segmentation (C) obtained with FreeSurfer [52]. Coloring indicates different anatomically defined subregions.

1.4.2 Tracer–enhanced MRI

In humans, molecular transport in the brain has been studied using imaging modalities such as tracer–enhanced MRI [12, 123], positron emission tomography [95, 167] and computer tomography [151]. In MRI studies, the focus of this thesis, tracer has been injected both intravenously [124, 125] and intrathecally [45, 158, 188, 197]. This thesis is concerned with intrathecally injected tracer.

Intrathecal tracer injection is performed via a lumbar puncture, shown in Fig. 1.5. Such injections combined with subsequent MR imaging have been used clinically to diagnose CSF leaks [78, 154, 163]. Tracer enhancement in the human brain was quantified from MRI for the first time by Ringstad and Eide at the Oslo University Hospital in Oslo, Norway [39]. The CSF tracer gadobutrol used in this and subsequent studies [44, 158, 159] is not approved for intrathecal injection. While recent studies indicate that this procedure is safe [51, 65], such studies currently need to be approved by institutional review boards.

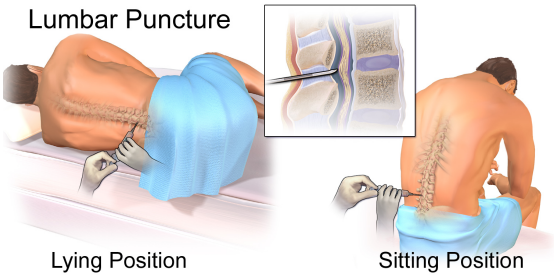

Figure 1.5: The image illustrates lumbar puncture as used in intrathecal CSF tracer injection. Image from [15].

A series of T_1–weighted MRI taken after intrathecal tracer admission in the patient considered in detail in Paper I is shown in Fig. 1.6. The tracer increases the image intensity, and one can see how the CSF tracer enters the head from the spinal canal. The lateral ventricle is enriched with tracer after four hours, and the tracer seems to have covered the full brain after 24 hours. After four weeks, the image is identical to that taken before injection, indicating that the tracer has been fully removed from the brain.

1.4.3 Idiopathic normal pressure hydrocephalus

The MRI analyzed in Paper I of this thesis are from the study [159]. Two of the patients considered therein, as well as some of the patients in Paper II, were diagnosed with a neurological disease named *Idiopathic normal pressure hydrocephalus* (iNPH). For this reason and the remarkable fact that the disease currently is the only reversible form of dementia [126], this section gives a brief description iNPH.

The name hydrocephalus refers to abnormal enlargement of the ventricles due to hindrance of CSF flow in the brain [4]. In normal pressure hydrocephalus, the CSF pressure is not significantly increased, and the term “idiopathic” indicates that the condition is not secondary to other conditions such as, e.g., subarachnoid hemorrhage [126].

The disease makes up about 10 % of dementia cases and affects an estimated 9–14 % of nursing home residents [153]. Symptoms of iNPH are impairment of gait, cognition, and urinary control. Surgical treatment can be performed by

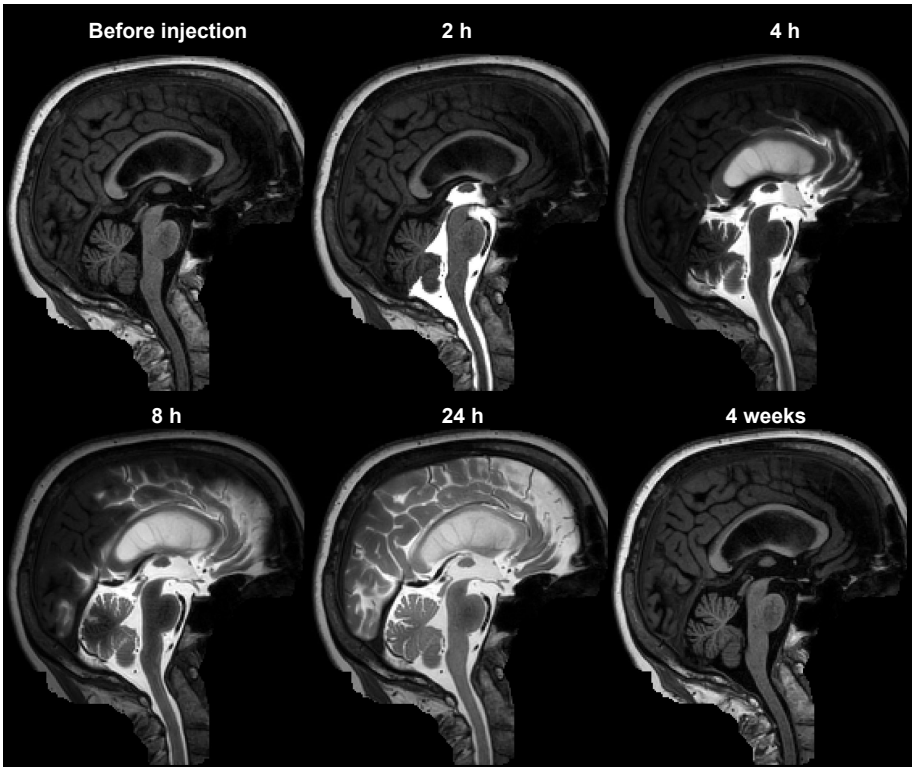

Figure 1.6: Sagittal slices (defaced) from CSF tracer–enhanced MRI of a patient from [159]. After 24 hours, the tracer has enriched the full brain and is cleared after four weeks.

placing a shunt in the brain to drain excess CSF from the ventricles. This can improve the symptoms with a success rate up to 80–90 % [40, 190].

Diagnosis of iNPH typically involves imaging with either CT or MRI [155] and is partially based on the presence of enlarged ventricles in the image [126], though not all patients with enlarged ventricles have iNPH [153]. Figure 1.7 shows the enlarged ventricles in a patient diagnosed with iNPH compared to a healthy subject.

The exact cause of the disease is still uncertain [18, 80]. It has recently been suggested that the disease might be linked to Alzheimer's disease via impaired glymphatic function [153]. For example, delayed clearance of CSF tracer in iNPH has been observed in MRI [42, 158], and DTI data indicates that water diffusivity is reduced along perivascular spaces in iNPH [8, 196]. The observation that shunting reduced incontinence to a higher degree than cognitive impairment [64] suggests that impaired glymphatic function might play an important role in iNPH [21], strengthening the hypothesis that an impaired glymphatic system links the two diseases [153].

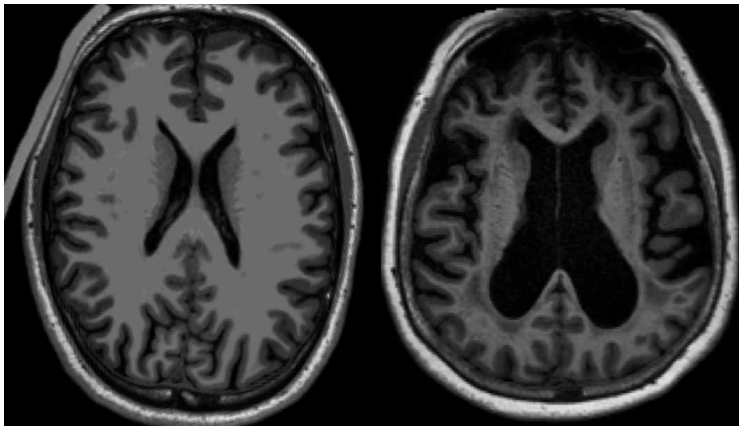

Figure 1.7: Axial slice from T_1–weighted MRI of a healthy control (left, MRI publicly available at [107]) and iNPH (right, subject from the study [159]) showing enlarged ventricles.

1.5 Mathematical modeling of brain clearance

In recent years, a plethora of modeling studies has been published that address various aspects of fluid transport in the brain. The attention of the modeling community was mostly directed at two aspects of the glymphatic concept, namely (a) transport mechanisms in perivascular spaces and (b) diffusive vs. advective transport in the brain interstitium [110]. The interested reader is referred to recent reviews of modeling brain fluid transport [85, 86, 110]. A review with focus on MRI and modeling can be found in [82].

This thesis is focused on aspect (b), the contribution of diffusion and advection (and possibly, other mechanisms) to solute transport in the human brain, from a macroscopic perspective. In the following, it will be outlined how different physiological concepts for molecular transport in the brain can be incorporated into macroscopic PDE models.

According to the "classical" hypothesis, molecules move by diffusion in the extracellular space in the brain. The extracellular space makes up about 20 % of the brain and can be considered a porous medium [130, 174]. This thesis is concerned with the CSF tracer gadobutrol, which is considered to be of small molecular size in this context [158]. For such molecules, diffusion is hindered by the tangled structure of the ECS [130]. Hence, on a macroscopic scale, diffusion will occur with an effective or apparent diffusion coefficient $D^*(\mathbf{x})$ (ADC) that varies between different locations $\mathbf{x}$ in the brain [174]. The ADC is lower than the diffusion coefficient D in a free medium. This geometric effect is described by the tortuosity $\lambda(\mathbf{x})$ defined in [130] as

$$\lambda^2(\mathbf{x}) = \frac{D}{D^*(\mathbf{x})}. \tag{1.1}$$

Here, the notation $D^*(\mathbf{x})$ is used to indicate that both the case where the diffusion parameter is spatially constant in white and gray matter, and the general case where it varies throughout the whole brain, are considered in this thesis. In general, D^*, and hence λ, are anisotropic parameters in brain tissue [174] and hence should be represented as tensors. Yet, the results reported in the supplementary materials accompanying Paper I and Paper II indicate that – on the macroscopic scale and a timescale of days – the anisotropy plays a negligible role for molecular transport.

In practice, (1.1) allows to estimate the tortuosity from DTI since the technique measures the hindered diffusion of water in the ECS [93]. A typical value for λ in brain tissue is 1.6 [174]. Some studies also report slightly higher values in the range 1.6–1.9 in humans [182] and slightly lower values in the range 1.5–1.7 in rodents [148]. With the assumption that gadobutrol can be considered to be a small molecule in the ECS, measurements of λ allow to estimate the spatially varying diffusion coefficient $D^*(\mathbf{x})$ for gadobutrol from DTI as described in Paper II.

The PDE that describes the concentration $c(\mathbf{x}, t)$ of molecules diffusing in some region Ω of the brain parenchyma is then

$$\frac{\partial}{\partial t} c(\mathbf{x}, t) = \nabla \cdot (D^*(\mathbf{x}) \nabla c(\mathbf{x}, t)) \tag{1.2}$$

where $\mathbf{x}$ denotes spatial position and t denotes time.

Throughout this thesis, equation (1.2) represents the "initial hypothesis" which other models are tested against. This testing is done by solving (1.2) numerically using appropriate boundary and initial conditions with the methods described in Section 1.6 and comparing the predictions to CSF tracer–enhanced MRI data.

As outlined in Section 1.3, it was classically presumed that the brain maintains homeostasis, at least partially, via intra– or extracellular degradation or removal by the bloodstream. On the macroscopic level, degradation can be incorporated into the model by adding a reaction–type term rc to the PDE:

$$\frac{\partial}{\partial t} c(\mathbf{x}, t) = \nabla \cdot (D^*(\mathbf{x}) \nabla c(\mathbf{x}, t)) - rc(\mathbf{x}, t). \tag{1.3}$$

Here, $r > 0$ represents the rate at which these processes occur. In this thesis, only the case that r is a (subject–specific) constant is considered, but in general, this parameter may be considered to be spatially varying and dependent on the circadian rhythm.

Transport of molecules in a fluid flowing along various preferred routes as in the classical understanding of brain fluid transport or, more specifically, along perivascular spaces as proposed by the glymphatic system, can also be included in the model. Advective transport via a spatially and temporally varying velocity field $\mathbf{v} = \mathbf{v}(\mathbf{x}, t)$ is represented mathematically with an additional term $\mathbf{v} \cdot \nabla c$. Further, possible effects such as secretion or absorption of fluid across the blood–brain barrier [70] can also be included via a source/sink term $\nabla \cdot \mathbf{v}$. The change in concentration c due to this source/sink is then given by $c\,(\nabla \cdot \mathbf{v})$. This term

can, by the product rule, be written together with the advection term as a single term $\nabla \cdot (c\mathbf{v})$ and the model becomes

$$\frac{\partial}{\partial t}c(\mathbf{x},t) = \nabla \cdot (D^*(\mathbf{x})\nabla c(\mathbf{x},t)) - rc(\mathbf{x},t) - \nabla \cdot (c(\mathbf{x},t)\mathbf{v}(\mathbf{x},t)). \tag{1.4}$$

It has also been suggested that transport along PVS is not driven by advection but rather by pulsatile mixing initiated by arterial pulsations (without net fluid flow) [86]. Mixing can be incorporated into the model with an diffusion–enhancement factor $\alpha \geq 1$:

$$\frac{\partial}{\partial t}c(\mathbf{x},t) = \nabla \cdot (\alpha D^*(\mathbf{x})\nabla c(\mathbf{x},t)) - rc(\mathbf{x},t) - \nabla \cdot (c(\mathbf{x},t)\mathbf{v}(\mathbf{x},t)). \tag{1.5}$$

Apart from the diffusion coefficient $D^*(\mathbf{x})$ which can be estimated from DTI as described above, all parameters $\alpha, r, \mathbf{v}$ in this model are unknown. Velocity fields for diffusion–advection based models, corresponding to $\alpha = 1$ and $r = 0$ in (1.5), can be obtained as in Paper II or using a regularized optimal mass transport technique from contrast–enhanced images. The latter has been applied to images from rodents [22, 90, 147] and also intravenous tracer enhanced MRI in humans [47]. To determine velocity fields as well as values for α and r from *intrathecal* CSF tracer–enhanced MRI in humans, PDE–constrained optimization as described in Section 1.6 is used in this thesis. Several important limitations of these approaches deserve to be discussed in greater detail in the following.

First, there is room for ambiguity when interpreting the estimated quantities. For example, the reaction–type term rc may be used to model very distinct physiological processes. On the one hand, it can represent degradation of biological molecules, which is less likely for gadobutrol. On the other hand, it can represent the averaged effect of processes happening on a time scale much faster than the time in between images, such as removal via the bloodstream in brain vasculature. However, gadobutrol is presumed not to cross the BBB [73]. It may also represent fast transport of tracer out of the brain to the subarachnoid space along various preferred pathways (classical concept) or solely along perivenous spaces (glymphatic concept).

Similar considerations hold true for advection velocity fields $\mathbf{v}$ estimated from data. The resolution of the MRI that are considered here is 1 mm^3. This is much larger than the scale on which the underlying physiological transport processes such as, e.g., advective transport in perivascular spaces ($\sim 40\,\mu$m [85]) occur. Hence, the velocity fields $\mathbf{v}$ inferred from this MRI data only represent the averaged effect of advective transport. It can not be distinguished if this is solely due to transport along arterial PVS (glymphatic hypothesis) or also along venous PVS and other preferred pathways (classical concept).

Also the diffusion enhancement parameter α can be interpreted in several ways. On the one hand, it may be used to represent the averaged effect of pulsatile mixing in PVS [86]. On the other hand, it has been argued that values of $\alpha \gg 1$ found from tracer–enhanced MRI in rodents are supportive of convective transport [150]. In humans, it was also found that a model with

$\alpha > 1$ could describe CSF tracer enhancement seen in MRI, but the effect was substantially smaller than observed in rodents [182]. This result was reproduced in this thesis with the method of physics–informed neural networks in Paper I.

Models can only be as realistic as their underlying assumptions. Except for the reaction–type term rc, the model (1.5) represents passive transport of molecules, either by diffusion or via fluid flow, in an inhomogeneous domain. This does not take into account that there are active transport mechanisms in the brain such as transport across membranes via co–transporters [103]. Such phenomena can be included in models using multicompartment modeling as in, e.g., [31, 139, 184]. Other limitations of the models are that they consider only the brain tissue and only take into account the interaction with the surrounding CSF via the boundary conditions. A more realistic model would include at least two domains with different underlying PDE, the brain tissue and the CSF, as a coupled system as in, e.g., [72]. Another interesting effect that is not included in this model is the deformation of the brain over time. Due to the rigidity of the skull, pulsations of CSF are induced by changes in blood volume during heart beat (the Monro–Kellie hypothesis, cf., e.g., [118]). This would, however, increase the computational effort since the mesh for the simulation domain $\Omega(t)$ needs to be deformed in every time step of the simulation.

Finally, it is worth putting the brain modeling presented in this section into a larger context. The human brain is, of course, a topic which has been studied for centuries by many researchers from different fields, including computational modeling. There are enormous research projects targeting computational modeling of the human brain, examples include the 40 million dollar Human Connectome Project [9, 46] and the Human Brain Project with a budget of a billion euros [109].

These projects address many aspects such as the functional connectivity of the brain, consciousness, and artificial intelligence, to name a few. This thesis is concerned with the fluid–mechanical aspects of the brain, a topic that many researchers presumed to be of minor relevance before the formulation of the glymphatic system [112]. The tremendous increase in interest in this topic, as illustrated by the over 1,000 publications on the glymphatic system since 2012 [86], can be attributed to the suggested link between brain fluid mechanics and neurological diseases [98, 112].

1.6 Numerical methods

From the mathematical point of view, this thesis considers PDE problems of the form

$$\frac{\partial}{\partial t}c(\mathbf{x},t) = \nabla\cdot(\alpha D^*(\mathbf{x})\nabla c(\mathbf{x},t)) - rc(\mathbf{x},t) - \nabla\cdot(c(\mathbf{x},t)\mathbf{v}(\mathbf{x})) \text{ in } \Omega_T \tag{1.6}$$

$$c(\mathbf{x},0) = c_0(\mathbf{x}) \text{ in } \Omega \tag{1.7}$$

$$c(\mathbf{x},t) = g(\mathbf{x},t) \text{ on } \partial\Omega\times[0,T] \tag{1.8}$$

with $\Omega_T = \Omega\times(0,T]$ for some fixed time $T>0$, $\Omega\subset\mathbb{R}^3$ open and bounded, and $c(\mathbf{x},t):\overline{\Omega}\times[0,T]\mapsto\mathbb{R}$ being the unknown state, modeling the concentration of tracer in the brain or MRI intensities in the context of this thesis. Depending on the model under consideration, different choices for the coefficients $\alpha\geq 1$, $r\in\mathbb{R}^+$, $D^*(\mathbf{x})\in C^0(\Omega)$ and $\mathbf{v}(\mathbf{x})\in C^1(\Omega)$ are taken. Note that, as a simplification to (1.5), the PDE problem (1.6)–(1.8) is considered only for stationary velocity fields in this thesis. The initial condition is given by $c_0\in L^2(\Omega)$. Throughout this thesis, only Dirichlet boundary conditions are used. In the case that c represents the concentration of CSF tracer in the brain, g is either estimated from MRI or learned as a control variable.

Depending on the modeling assumptions under consideration, different terms in the right–hand side of (1.6) are omitted in the papers presented in this thesis. In Paper I, only the diffusion term is considered. Paper II considers also diffusion–reaction and diffusion–advection problems, i.e. either the term rc or the term $\nabla\cdot(c\mathbf{v})$ is omitted. In Paper III, both diffusion and reaction as well as the fluid inflow component $c(\nabla\cdot\mathbf{v})$ are omitted, resulting in a hyperbolic advection equation.

Two different numerical approaches are used in this thesis to solve special cases of the problem (1.6)–(1.8) approximately. Firstly, all papers use standard continuous or discontinuous Galerkin finite element methods (FEM) for the spatial discretization and finite difference (Crank–Nicolson or Runge–Kutta) methods for the temporal discretization, see, e.g., [24, 36, 142]. Secondly, for comparison, Paper I applies a more recently[2] popularized approach, physics–informed neural networks (PINNs) [81, 143]. In the FEM approach, one searches for an approximation to the weak solution of the PDE in a finite–dimensional, linear function space defined by piecewise polynomial functions. The PINN approach approximates the strong solution of the PDE in the nonlinear space of neural networks with a finite number of neurons.

The specific choices of FEM and finite difference methods used to solve the variations of (1.6) considered in the papers presented in this thesis are described therein. These methods are discussed in detail in, e.g., [24, 36, 79, 142]. Since the PINN method differs substantially in various aspects from FEM, this section illustrates the difference between the two by considering the simplified problem

[2]The idea goes back to the 1990s [37, 92, 141], cf. also the recent review [27], but was popularized using modern machine learning tools in 2019 in [143].

of solving

$$-\Delta u(\mathbf{x}) = f(\mathbf{x}) \quad \text{in } \Omega \tag{1.9}$$

$$u(\mathbf{x}) = 0 \quad \text{on } \partial\Omega. \tag{1.10}$$

From the mathematical point of view, there exists a unique weak solution $u \in H_0^1(\Omega)$ for $f \in L^2(\Omega)$ and $\Omega \subset \mathbb{R}^d$ open and bounded [50]. Furthermore, for $\partial\Omega \in C^2$, u is also a strong solution, i.e., $u \in H^2(\Omega) \cap H_0^1(\Omega)$ [60]. In section 1.6.1, it is shown how the weak solution is approximated using FEM. Then, the PINN formulation to approximate the strong solution of (1.9)–(1.10) is introduced. This setting is also referred to as a forward problem, since the boundary conditions as well as the right–hand side f are known. Section 1.6.2 considers inverse problems, where some parameters like, for example, the right–hand side f in (1.9), are unknown and instead measurements of u are available. As an example, it is shown how the problem of determining an unknown f from measurements can be formulated with both methods. Both sections are concluded with a comparison of some aspects of the methods. The description in the following is based on [79] for FEM and [27] for PINN if not stated otherwise.

1.6.1 Forward problems

The FEM approach The FEM approach yields an approximation $u_h \in V_h$ to the weak solution $u \in H_0^1(\Omega)$ of the PDE problem (1.9)–(1.10) in a finite–dimensional, linear subspace $V_h \subset H_0^1(\Omega)$. This space is spanned by a finite set of basis functions ψ_i, which in FEM typically are piecewise polynomials with compact support. The latter means that all basis functions fulfill $\psi_i = 0$ outside some small subregion of Ω. These subregions are determined by the arrangement of the cells in the mesh needed in FEM to discretize the domain Ω, and the index h in V_h is a measure for the mesh size, e.g., the maximum cell diameter.

The approximate solution is then

$$u_h(\mathbf{x}) = \sum_{i=1}^{N} \mathrm{u}_i \psi_i(\mathbf{x}) \tag{1.11}$$

with unknown coefficients $\mathrm{u}_i \in \mathbb{R}$. These are determined by the requirement that the *weak* or *variational form* of (1.9) holds for u_h,

$$\int_\Omega \nabla u_h(\mathbf{x}) \cdot \nabla v_h(\mathbf{x}) \, \mathrm{d}x = \int_\Omega f(\mathbf{x}) v_h(\mathbf{x}) \, \mathrm{d}x \quad \forall v_h \in V_h. \tag{1.12}$$

This equation is obtained by multiplying (1.9) by a *test function* $v_h \in V_h$ and integrating by parts. Note that there is no boundary integral in (1.12) since the boundary condition (1.10) is incorporated in the chosen function space $V_h \subset H_0^1(\Omega)$ in which the solution is searched for. Inserting (1.11) into (1.12) yields a linear system

$$\mathcal{A}\mathbf{u} = \mathbf{f} \tag{1.13}$$

where $\mathbf{u} \in \mathbb{R}^N$ is a vector containing the unknown coefficients $\mathrm{u}_1, \ldots, \mathrm{u}_N$ and the stiffness matrix $\mathcal{A} \in \mathbb{R}^N \times \mathbb{R}^N$ is defined as

$$\mathcal{A}_{ij} = \int_\Omega \nabla\psi_i(\mathbf{x}) \cdot \nabla\psi_j(\mathbf{x})\,\mathrm{d}x \tag{1.14}$$

and the right–hand side vector $\mathbf{f} = (\mathrm{f}_1, \ldots, \mathrm{f}_N) \in \mathbb{R}^N$ is defined as

$$\mathrm{f}_i = \int_\Omega f(\mathbf{x})\psi_i(\mathbf{x})\,\mathrm{d}x. \tag{1.15}$$

Hence, solving the weak form of the PDE problem (1.9)–(1.10) approximately using FEM means solving a linear system of equations.

The PINN approach From the continuous perspective, in PINNs one considers the equivalent strong formulation of (1.9)–(1.10) [121]:

$$\min_{u \in H^2(\Omega)} E(u, f), \quad E(u, f) = w_p||-\Delta u - f||^2_{L^2(\Omega)} + ||u||^2_{L^2(\partial\Omega)} \tag{1.16}$$

with the requirements on $\partial\Omega$ and f as in (1.9)–(1.10) and $w_p > 0$ is a user–determined weighting factor. The strong solution u is approximated in terms of a neural network $u_{\boldsymbol{\theta}} \in C^\infty(\mathbb{R}^d)$ as defined in the following.

The most common network architecture is the feedforward fully–connected neural network (also known as multilayer perceptron). Following the notation in [27], such a network is parameterized by M parameters $\boldsymbol{\theta} \in \mathbb{R}^M$ and defined as a composition of functions $\sigma_i, i = 1, \ldots, L$ as

$$u_{\boldsymbol{\theta}}(\mathbf{x}) = \sigma_L \circ \cdots \circ \sigma_1(\mathbf{x}). \tag{1.17}$$

The functions $\sigma_i, i = 1, \ldots, L-1$ are defined as affine transformations followed by a nonlinear function σ:

$$\sigma_i : \mathbb{R}^{n_{i-1}} \times \mathbb{R}^{n_i \times n_{i-1}} \times \mathbb{R}^{n_i} \mapsto \mathbb{R}^{n_i}, \sigma_i(\mathbf{y}; W_i, \mathbf{b}_i) = \sigma\left(W_i\mathbf{y} + \mathbf{b}_i\right) \tag{1.18}$$

where the index i indicates that σ_i is defined by the *weight matrix* $W_i \in \mathbb{R}^{n_i \times n_{i-1}}$ and the *bias* $\mathbf{b}_i \in \mathbb{R}^{n_i}$. The last function σ_L is usually just an affine transformation $\sigma_L(\mathbf{y}; W_L, \mathbf{b}_L) = W_L\mathbf{y} + \mathbf{b}_L$ and called the *output layer*. The weights W_i and biases $\mathbf{b}_i$ define the parameter vector $\boldsymbol{\theta} = ((W_1, \mathbf{b}_1), \ldots, (W_L, \mathbf{b}_L))$. The action of the usually nonlinear *activation function* σ is understood to be component–wise. In the PINN literature, typical choices are the hyperbolic tangent or the sine function. The size of the weight matrices W_i and bias vectors $\mathbf{b}_i$, as well as the number L of concatenations, are design choices. The only constraint is given by the input and output dimensions, the dimension d of input $\mathbf{x}$ defines n_1, and $n_L = 1$ if the network is a function $u_{\boldsymbol{\theta}} : \mathbb{R}^d \mapsto \mathbb{R}$. The number L of concatenations is usually referred to as *number of layers* and the natural number n_i is usually referred to as the *number of neurons* in layer i.

The choice to use neural networks $u_{\boldsymbol{\theta}}$ as defined by (1.17) in PINNs is one import distinction to the FEM approach. The FEM approximation to the weak PDE solution u is linear *with respect to the unknown coefficients* u_i, and from that it follows that in FEM one has to solve a linear system to the determine the unknowns. The neural network functions $u_{\boldsymbol{\theta}}$ as defined by (1.17) are not linear with respect to the unknown parameters $\boldsymbol{\theta}$.

In practice, the integrals in E as defined by (1.16) are usually discretized. The discretized version of (1.16) is defined as

$$E_d(u, f) = w_p \mathcal{L}_p(u, f) + \mathcal{L}_{bc}(u). \tag{1.19}$$

The *PDE loss* $\mathcal{L}_p$ for the example problem (1.9) would be defined as

$$\mathcal{L}_p(u, f) = \frac{1}{N_P} \sum_{\mathbf{x} \in P} \left(-\Delta u(\mathbf{x}) - f(\mathbf{x})\right)^2 \tag{1.20}$$

where the finite set of N_P points $P \subset \Omega$ is referred to as *residual points* in the PINN literature. The *boundary loss* $\mathcal{L}_{bc}$ for (1.10) is

$$\mathcal{L}_{bc}(u) = \frac{1}{N_B} \sum_{\mathbf{x} \in B} \left(u(\mathbf{x})\right)^2 \tag{1.21}$$

where $B \subset \partial\Omega$ is a finite set of N_B points on the boundary of the domain.

In terms of neural networks $u_{\boldsymbol{\theta}}$, (1.19) becomes a finite dimensional minimization problem,

$$\min_{\boldsymbol{\theta} \in \mathbb{R}^M} E_d(u_{\boldsymbol{\theta}}, f), \quad E_d(u_{\boldsymbol{\theta}}, f) = w_p \mathcal{L}_p(u_{\boldsymbol{\theta}}, f) + \mathcal{L}_{bc}(u_{\boldsymbol{\theta}}). \tag{1.22}$$

This optimization problem is usually solved using gradient–based optimization algorithms such as ADAM [87] or limited–memory BFGS algorithms such as L–BFGS–B [53, 96].

Due to the fact that the optimization problem (1.22) is non–convex with respect to the parameters $\boldsymbol{\theta}$, one difficulty with the PINN method is the minimization of the loss function E_d, also referred to as *training* in machine learning. Many studies have been published on training PINNs and it is an active matter of research, cf. [27] for a recent review. In the scope of this thesis, two aspects that have been addressed in the PINN literature are worth mentioning. The first aspect is the choice of the weighting factor w_p in (1.22). Several works [104, 111, 185, 186] have put forward methodologies to choose loss weighting factors dynamically during training.

The second aspect is the choice of the residual points $P \subset \Omega$. Instead of randomly or quasi–randomly sampling points from Ω, [101] suggested to extend P with points in regions where the squared PDE residual $(-\Delta u_{\boldsymbol{\theta}}(\mathbf{x}) - f(\mathbf{x}))^2$ is high. This aspect of PINNs has received greater attention, with Paper I of this thesis and others [33, 55, 62, 105, 192, 195] proposing schemes to sample residual points. Recently, this aspect has been reviewed in [191].

With respect to the theoretical aspects, FEM has been analyzed for decades, and in many cases, convergence criteria are established and error estimates are available. For example, for the model problem (1.9)–(1.10) considered in this section and V_h defined by piecewise linear basis functions, the error between weak solution $u \in H^2(\Omega)$ and FEM approximation u_h behaves like

$$||u - u_h||_{L^2(\Omega)} \leq Ch^2 \tag{1.23}$$

for $f \in L^2(\Omega)$ and Ω being a convex domain with polygonal boundary, cf. [79], and C is a constant independent of h. So it is guaranteed that the FEM solution converges to the weak solution (in the L^2–norm) as the mesh is refined and $h \to 0$. Moreover, the rate of convergence is known. In numerical experiments, these rates can also be observed.

This is currently not the case for PINNs. The nonlinearity of the Ansatz space chosen in PINNs makes the numerical analysis difficult, and deriving error estimates in terms of the numbers of layers and neurons is ongoing research [27]. There are, however, some recent works that address the issue. In [165] it was shown that the PINN is consistent for a class of PDE in the sense that global minimizers of the PINN loss $\mathcal{L}$ converge to the true solution u of the PDE as the number of training points goes to infinity. Error bounds in terms of the PINN loss $\mathcal{L}$ or parts of it are given in [97, 121]. Other works have given asymptotic results, i.e., shown that networks $u_{\boldsymbol{\theta}}$ exist such that the error between $u_{\boldsymbol{\theta}}$ and u vanishes as the width and depth of the network goes to infinity, e.g. [115, 166]. In [77] non–asymptotic rates for the PINN error are given. However, convergence to the true solution can not be observed numerically with commonly used PINN training algorithms such as ADAM and L–BFGS–B [168] since PINNs can usually not be trained to relative errors lower than 10^{-4} [120].

Hence, there currently exists a considerable gap in terms of theoretical foundation between the PINN and FEM method. Current approaches that target closing the numerical aspects of this gap are, e.g., the optimization algorithms proposed in [120, 168]. These algorithms were used to train PINNs to relative errors of 10^{-8} or lower, substantially increasing the accuracy to which PINNs can be trained.

1.6.2 Inverse problems

The following description of the reduced functional approach is based on the textbooks [69, 181] if not stated otherwise. Consider now the inverse problem of recovering an unknown source function f from (possibly noisy) measurements $u_d(\mathbf{x})$ of the solution to (1.9)–(1.10). For ease of presentation, the boundary condition $u = 0$ on $\partial\Omega$ is still assumed to hold.

Using the L^2–norm to measure the mismatch to the observations, this problem can be formulated as follows: Find $f : \Omega \to \mathbb{R}$ such that the functional

$$\mathcal{J}(u, f) = \int_\Omega \left(u_d(\mathbf{x}) - u(\mathbf{x})\right)^2 \,\mathrm{d}x + \alpha \int_\Omega f(\mathbf{x})^2 \,\mathrm{d}x \tag{1.24}$$

is minimized with the constraint that u is the solution to (1.9)–(1.10). The term $\alpha \int_\Omega f^2 \, \mathrm{d}x$ with $\alpha > 0$ is referred to as Tikhonov regularization [178]. It is a method to address the fact that inverse problems are usually not well–posed in the sense of Hadamard [63]. This problem, however, is well–posed for $\alpha > 0$, cf. [69, 181].

Various approaches such as the one–shot–approach via the KKT optimality system (named after the mathematicians Karush, Kuhn and Tucker) to solve this problem exist. The FEM approach taken in this thesis is a gradient–based optimization approach. Here, one considers the *reduced* functional $\hat{\mathcal{J}}(u_h(f), f)$. Here, $u_h(f)$ denotes the FEM approximation to the weak solution of (1.9)–(1.10) with right–hand side f. Hence the reduced functional is a function of the unknown f only. Numerically, the gradient $\partial \hat{\mathcal{J}} / \partial f$ can be obtained efficiently by solving the adjoint equations as implemented in [116], also referred to as reverse mode automatic differentiation in machine learning [10].

With physics–informed neural networks, a penalty approach to determine the unknown f is taken [143]. Since the forward PDE solve in PINNs corresponds to an optimization problem, inverse problems can be solved in a very similar fashion as forward problems. The data mismatch in the PINN approach is defined as

$$\mathcal{L}_d(u_{\boldsymbol{\theta}}) = \frac{1}{N_O} \sum_{\mathbf{x} \in O} \left(u_{\boldsymbol{\theta}}(\mathbf{x}) - u_d(\mathbf{x}) \right)^2 \tag{1.25}$$

where the finite set O either denotes the N_O points where the data function $u_d(\mathbf{x})$ is sampled (if the data is available at every $\mathbf{x} \in \Omega$) or the set of points where data is available.

Next, the unknown f is represented as a neural network $f_{\boldsymbol{\delta}}$ with trainable parameters $\boldsymbol{\delta} \in \mathbb{R}^{M_\delta}$. The PDE loss (1.20) hence now involves two neural networks $u_{\boldsymbol{\theta}}, f_{\boldsymbol{\delta}}$ with unknown parameters $\boldsymbol{\theta}, \boldsymbol{\delta}$. Determining an approximation to f means optimizing the PINN functional (1.22) augmented with the data loss with weight $w_d > 0$:

$$\min_{(\boldsymbol{\theta}, \boldsymbol{\delta}) \in \mathbb{R}^{M + M_\delta}} w_p \mathcal{L}_p(u_{\boldsymbol{\theta}}, f_{\boldsymbol{\delta}}) + \mathcal{L}_{bc}(u_{\boldsymbol{\theta}}) + w_d \mathcal{L}_d(u_{\boldsymbol{\theta}}). \tag{1.26}$$

Several comments are appropriate. First, note that no regularization was added to the PINN formulation of the inverse problem. Regularization is not always needed in numerical experiments as demonstrated in, e.g. [19, 20, 143] and by our results in Paper I. In the PINN literature, the PDE loss term $\mathcal{L}_p$ is considered to regularize the problem to some extent, e.g., [67]. Secondly, if the boundary conditions are unknown, they may simply be omitted from the PINN approach by removing the term $\mathcal{L}_{bc}$ from (1.26). This represents a possible benefit of the PINN approach over the FEM approach, since there the boundary conditions are always required in the forward PDE solve.

Thirdly, the PINN formulation (1.26) has two important hyperparameters w_p, w_d which imply that (1.26) can be interpreted as a multi–objective optimization problem [160]. In this sense, the weights w_p, w_d can be regarded as not only numerical parameters, but reflect to some degree the modeling

assumption. High confidence in the PDE model is reflected by a high PDE weight w_p. This perspective distinguishes the PINN approach from the FEM approach where the (discretized) PDE is always fulfilled. In Paper I we observed this distinction numerically in the sense that adjusting the PINN hyperparameters such that the PDE loss becomes small after training yields results comparable to the FEM approach.

The two approaches for determining the unknown f from data and the PDE constraint can be summarized as follows. In the FEM based approach, every update of f involves one solve of the PDE system and one solve of the adjoint system to compute the gradient $\partial\hat{\mathcal{J}}/\partial f$. This approach can be slow if the PDE solve is computationally expensive, but the PDE is always fulfilled in a discretized sense. The PINN approach instead solves a single optimization problem by imposing the PDE as a soft constraint. Hence, the parameters of u and f are optimized simultaneously when minimizing the PINN functional (1.26). In other words, the PDE does not have to be solved in every gradient update, possibly making the optimization computationally more efficient. However, both the choice of weighting parameters as well as the non–convexity of the PINN loss make the optimization problem challenging, usually requiring hyperparameter tuning.

From this perspective, both methods have benefits and disadvantages, and the optimal choice of method may be problem–dependent. This, and the fact that FEM has been developed for many more years than PINN, make a meaningful comparison of the methods challenging. Paper I and [61] are two recent examples that address this question.

1.7 Summary of Papers

Paper I - Investigating molecular transport in the human brain from MRI with physics–informed neural networks

In recent years, there has been an extensive increase in efforts to combine traditional numerical methods with machine learning. One popular example are physics–informed neural networks. The methodology shows promise in overcoming some of the drawbacks faced by well–established mesh–based numerical methods, in particular FEM, in PDE–constrained optimization (e.g., high computational effort).

This paper applies physics–informed neural networks to estimate the apparent diffusion coefficient that governs the spread of CSF tracer into the brain as seen in MR images over a time span of two days. A graphical summary of the paper is given in Fig. 1.8. We find that the PINN approach yields good accuracy in synthetic test data without noise and with artificial noise. It is demonstrated that the results are stable with respect to important hyperparameters such as the weighting of the data and PDE loss terms.

On real data from CSF tracer–enhanced MR scans, however, we find that the PINN becomes more sensitive to hyperparameters and more sophisticated

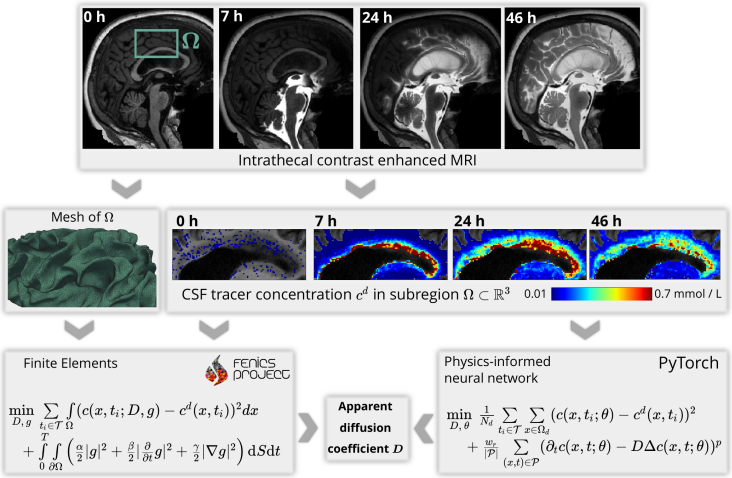

Figure 1.8: Graphical summary of Paper I. We compare PINNs to a FEM based approach for estimating the apparent diffusion coefficient describing the distribution of CSF tracer seen in MRI.

training strategies are needed. In particular, our results indicate that adaptive sampling of training points and a reformulation of the PINN loss function using the ℓ^1–norm are necessary to obtain numerically stable estimates of the diffusion coefficient.

In this context, we introduce a new adaptive strategy for sampling the PDE training points during optimization. This approach is a modification of "residual based adaptive refinement" (RAR) [101] where the computational cost increases during PINN training due to a growing set of training points. With our proposed sampling scheme, the computational cost does not increase since the amount of training points stays constant. This does not alter the results in the sense that the estimated diffusion coefficient does not change compared to the results using the RAR sampling.

Throughout the paper, we compare results from the PINN approach to a finite element based approach. We find that, with proper hyperparameter tuning, both methods yield comparable estimates of the apparent diffusion coefficient. Interpreted in light of the glymphatic model, the findings support the notion that diffusion alone is insufficient as the only mechanism to distribute molecules such as the CSF tracer in the brain.

Paper II - Human brain solute transport quantified by glymphatic MRI-informed biophysics during sleep and sleep deprivation

Understanding the dynamics of CSF and its interaction with the human brain is of critical importance, both due to the implications of CSF malfunctions in neurodegenerative diseases and for the CSF being a possible pathway to deliver drugs to the brain.

To address this problem, we use MRI from a clinical study [45]. Therein, 24 subjects were imaged over a time span of three days after intrathecal CSF tracer injection. We combine this data set with PDE–constrained optimization to assess the relative importance of different molecular transport mechanisms.

First, we *quantify* the subject-specific CSF tracer concentrations in the brain from a type of *qualitative* MRI known as T_1–weighted images. This requires mappings of the relaxation time T_1 in the brain, which are not available for all of the 24 subjects. In a systematic assessment we find that surrogate T_1 values can be used instead, allowing us to include all subjects in the analysis.

We find that up to 25 % of the injected CSF tracer have entered the brain after 24 hours, demonstrating the efficacy of the CSF as a possible drug delivery pathway. A total of seven subjects underwent voluntary sleep deprivation in the first night of the study. In those subjects, significantly more tracer is found in the brain 48 hours after injection, supporting the critical role of sleep for brain health.

Next, we compare this data to finite element simulations of diffusion of CSF tracer into the brain with subject-specific boundary conditions informed by the data. Diffusion simulations alone both underestimate the tracer enrichment and clearance from the brain, suggesting that other solute transport mechanisms play a significant role.

We therefore study two alternate mathematical models for brain solute transport, related to different possible transport mechanisms: First, motivated by the parenchymal bulk flow proposed by the glymphatic system [75], a model that includes diffusive and advective CSF tracer transport.

The second model includes enhanced diffusion (possibly due to dispersion [84, 180]) and a local clearance rate. The latter condenses different phenomena that may occur on a time scale faster than resolved by the available data into a single scalar parameter. It represents possible mechanisms such as clearance of the tracer to the blood stream or direct drainage to meningeal lymph nodes [6, 100] without mixing with CSF [70, 145]. These models contain unknown quantities (velocity fields in the first model and dispersion and local clearance factors in the second model), and we use PDE-constrained optimization to determine them in a subject-specific manner.

The data under consideration is sparse in time (typically, MRI are available at 2, 6, 24 and 48 hours after injection) and subject to substantial noise. Still, it is found that the parameters estimated by PDE–constrained optimization are stable over a reasonable range of numerical parameters such as regularization (advection model) and temporal discretization (local clearance model).

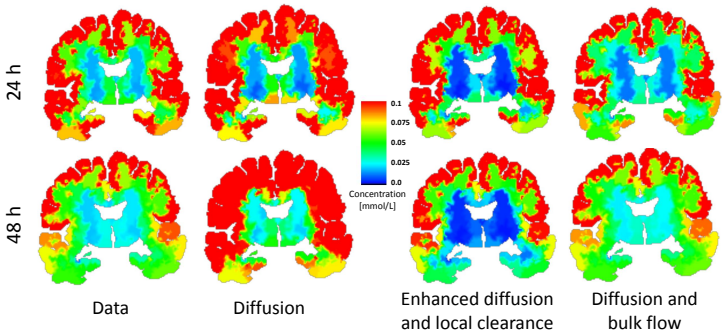

Figure 1.9: Group-averaged concentration of CSF tracer 24 and 48 hours after injection measured from MRI compared to different physics-based subject-specific clearance models investigated in Paper II.

With optimal subject-specific parameters, both models yield significantly better agreement to the data than a diffusion model, cf. Fig. 1.9. It is found that the average advection velocities are significantly reduced in the sleep deprived group in the time interval from 24–48 hours.

The optimal models with diffusion and local clearance suggest that transport happens 3-4 times faster than extracellular diffusion, and that half the tracer in the brain is cleared within 4-5 hours, which is in line with independent clinical measurements.

Paper III - Medical Image Registration using optimal control of a linear hyperbolic transport equation with a DG discretization

Generating subject-specific brain meshes from MRI can in some cases require extensive manual labor and expertise, e.g., when small substructures are poorly resolved in the image and hence not identified by automatic processing software. To address this issue, Paper III describes a new algorithm to create subject-specific brain meshes from a template mesh and image. The idea is to find a nonlinear registration that registers a template image to an input image, and then use the same transformation to deform a template mesh into a new mesh, cf. Fig. 1.10.

The paper introduces a nonlinear image registration algorithm based on deforming the image by solving an advection equation. Higher–order discontinuous Galerkin and Runge–Kutta methods are used to discretize the equation in space and time, respectively. To allow for differentiability with respect to the unknown advection velocity field, we introduce a smoothened upwind scheme. Theoretical analysis is performed to show that the numerical scheme is convergent under certain assumptions.

Numerical examples are given to demonstrate that the algorithm efficiently registers template to input image. Despite the fact that the approach is based

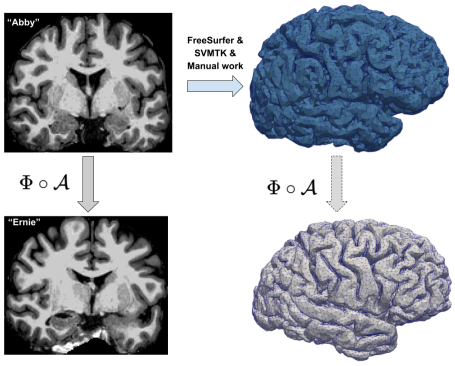

Figure 1.10: Paper III introduces a new numerical approach to nonlinear image registration. We apply it to register two MR images, and show that the registration can also be used to generate new subject-specific volume meshes.

on volumetric registration only, our numerical results show that the algorithm registers the images with similar accuracy as established volumetric and surface-based schemes. Finally, it is shown that the algorithm deforms a template mesh for the ventricular system without significantly degrading mesh quality to match the input image. Limitations are shown in an example where the current formulation of the algorithm does not achieve satisfyingly accurate registration of the cortical folds in a mesh of the left brain hemisphere.

Paper IV - Quantifying cerebrospinal fluid tracer concentration in the brain

Combining multi-modal clinical data with finite element simulations to study complex biophysical models of the human brain requires a substantial and diverse set of computational tools: the MR images need to be registered and normalized, subject–specific meshes need to be generated, and the data needs to be imported into numerical simulation software packages. The CSF tracer–enhanced MRI of human brains analyzed in this thesis is not established clinical practice but merely used in clinical studies. Hence, such images represent a new type of data for which the technical details of pre-processing have not been discussed in the literature so far. Given that CSF tracer–enhanced MRI give unprecedented insight into molecular transport in the brain *in vivo*, it can be expected that more researchers and clinicians around the world will use the technique.

The aim of this book chapter is to provide a detailed and practical discussion to facilitate the downstream analysis of such data sets and to simplify their usage in modeling. Starting from a time series of intrathecal CSF tracer–enhanced human brain MRI, the book chapter describes how to estimate the tracer concentration and incorporate them into subject-specific finite element simulations (cf. Fig. 1.11). All steps are illustrated by publicly available

code examples that allow the reader to reproduce the pipeline from data pres–processing to finite element simulations either on the publicly available data set that will accompany the book or on their own data. By making the technical overhead from raw data to modeling simpler, this book chapter will aid new modelers aiming to model brain solute transport from MRI.

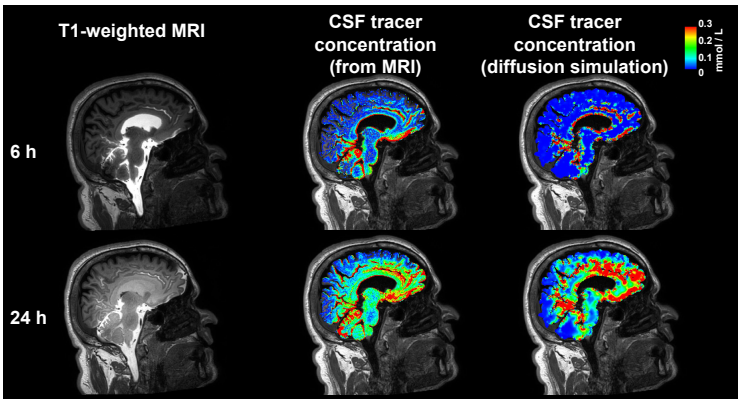

Figure 1.11: Using CSF tracer–enhanced human brain MRI (left) to estimate the CSF tracer concentration (middle) and incorporating this data into numerical simulations (right) requires a considerable set of computational tools. The book excerpt Paper IV and describes all the necessary steps for this modeling pipeline in great detail.

1.8 An integrated view of the papers

The techniques and assumptions applied in the individual papers share many similarities. In this section, the most important aspects of the papers are compared with each other, both with respect to modeling assumptions and technical details.

Paper I and Paper II are both concerned with a concrete physiological question. In both of the papers, we evaluate how well diffusion describes the penetration of CSF tracer into the human brain on the macroscopic scale over a time span of two days. In Paper I, we focus on a subregion of the subcortical white matter in one hemisphere in three subjects and in Paper II we consider the whole parenchyma in 24 subjects. In Paper I, we do not prescribe boundary conditions, since they are not needed when applying the inverse PINN. In the FEM approach, the boundary condition is a control variable that is learned from data. With both methods, we consider the diffusion equation and optimize for the apparent diffusion coefficient. The approach in Paper II is based on FEM only and prescribes the subject–specific boundary condition as a linear interpolation in time between available MRI. For the diffusion and local clearance model tested in Paper II, we optimize for both the apparent diffusion coefficient and the clearance rate.

Hence, in light of the different modeling assumptions (diffusion vs. diffusion plus local clearance), implementation details (learning vs. prescribing boundary conditions from data) and region of interest (subcortical white matter subregion vs. full brain parenchyma) some difference between the estimated parameters should be expected. The fact that we arrive at qualitatively similar results (in the sense that D^* is larger than the DTI value) should be considered as supportive to the physiological conclusions drawn from both studies.

Interestingly, for the only iNPH patient out of the 24 subjects considered in Paper II, we find an optimal diffusion coefficient 1.5× higher than DTI, which is comparable to the value found in Paper I for two other iNPH patients. However, it is important to note that there is large variation in the CSF tracer distribution seen in MRI between patients and diseases [43, 73]. Meanwhile, more data is needed, and this observation should motivate further investigation into the relation between different diseases and molecular transport parameters estimated with PDE–constrained optimization (see also Section 1.11).

Both papers are concerned with patients diagnosed with neurological diseases. In contrast, the data analyzed in Paper IV was obtained from a healthy volunteer. Paper IV focuses mostly on technical details of estimating and using CSF tracer concentration in simulations (as done in Paper I and Paper II), but also presents some simulation results. The results are in agreement with those from clinical data from *patients* in Paper I and Paper II: also in the *healthy* volunteer it is found that the tracer enters and leaves the brain faster as compared to diffusion simulations.

With respect to the technical aspects considered in this thesis, the methodology covered in Paper III is not limited to image registration. It is closely related to the inverse velocity identification in Paper II. While no diffusion term is desired for the application in Paper III as it would smoothen the mesh, the main difference is in the numerical solution of the underlying equation.

Another technical difference are the time and space discretization schemes. In Paper IIIone hundred time steps and a discontinuous representation of the data are used, while the approach put forward in Paper II uses a single time step and continuous representation of the data. These differences are motivated by the respective applications. The larger number of time steps used in Paper III is to satisfy a Courant–Friedrichs–Lewy (CFL) condition to obtain a diffeomorphism while at the same time allowing for more complex deformations than with one time step. Using the discontinuous Galerkin method also is a natural choice in Paper III since we work with voxelized data. While we focus on theoretical aspects and a proof of concept numerical example in Paper III, there are possible efficiency benefits by implementing the approach in parallel on a GPU. Given a faster implementation, the algorithm put forward in Paper III can in the future be used to efficiently estimate velocity fields from MRI directly (without generating and using a subject–specific brain mesh), significantly simplifying modeling workflows.

1.9 Conclusions

The overarching theme of this thesis is the combination of PDE–constrained optimization and magnetic resonance images to (a) address the specific physiological question of diffusive vs. advective molecular transport in the brain and (b) to develop methods and technology that simplify future modeling studies.

With respect to (a), Paper I and Paper II represent an original contribution to the field by providing transport parameter quantification from human MRI data. Both papers arrive at a similar conclusion: Diffusion alone is not sufficient as sole transport mechanism, and transport occurs faster than predicted by diffusion. In detail, in Paper I we find apparent diffusion coefficients $1.2 - 1.8\times$ larger than estimated from DTI. In Paper II, we find the subject–specific optimal apparent diffusion coefficients $3 - 4\times$ higher than DTI (on the group level). The qualitative conclusion hence is the same, meanwhile some of the quantitative difference in the estimated parameters may be attributed to the modeling assumptions used in both papers being different, cf. the discussion in Section 1.8.

Aspect (b) was addressed both by exploring the PINN method in Paper I and proposing a new mesh generation approach in Paper III. As shown in Paper I, the PINN needs to be tuned carefully when applied to temporally sparse and noisy MRI data. Also, our implementation of the PINN was roughly twice as fast as our FEM implementation. However, we averaged the PINN results after training several networks with randomly initialized weights. Hence, in this case, the PINN approach did not outperform the FEM approach in terms of the total computational cost.

The exemplary results presented in Paper III show that our advection–equation based image registration yields registration with accuracy comparable to a publicly available surface and volume based registration algorithm, FreeSurfer cvs–register [138]. This indicates that the surface registration steps may not always be necessary, and a simpler registration procedure can be used. It was also found that the approach works well for registering a template mesh of the ventricular system to a new patient. However, it was shown that the registration substantially degraded a mesh for the left hemisphere, rendering the mesh useless without post–processing.

Hence, two main conclusions with regards to aspect (b) can be drawn from the results presented. First, currently FEM–based approaches is more suited for (inverse) brain solute transport modeling using gMRI data. It should be noted, however, that both methods are being actively developed, cf. also Section 1.11, and this suggestion should continuously be re–evaluated. Second, an image–registration based approach can be used to generate, via a semi–automated image registration approach, volume meshes for subregions of the brain, making manual processing obsolete in some cases.

1.10 Implications of the findings

This section discusses some implications of the results presented in the papers collected in this thesis. With regards to the MRI data, we have performed a systematic evaluation of the influence of different data integration choices (T_1–maps) on the CSF tracer levels in the brain estimated from MRI in the Supplementary materials to Paper II. It was found that, on the brain–wide level, the choice of baseline T_1–map does not significantly alter the computed tracer levels. The findings suggests that, at least brain–wide, CSF tracer enrichment can be quantified from *qualitative* T_1–weighted MRI alone. This is an important conclusion since sometimes, such as in the data sets considered in Paper II or Paper IV, T_1–maps are not available for some subjects. Given that intrathecal CSF tracer injection is invasive and the following repeated MR imaging is stressful to the patients, this finding is particularly relevant. It implies that the imaging data from subjects without T_1–map can still be used in quantitative analyses. Hence, the scientific value of the imaging data, acquired at high financial cost and stress endured by the patient, is increased.

From the physiological point of view, the inverse identification of unknown model parameters presented in Paper I and Paper II allows one to quantify the contribution of *possible* transport mechanisms. For instance, the results reported in [182] and Paper I as well as Paper II all indicate that there has to be another molecular transport mechanism in the brain in addition to extracellular diffusion. The contribution of this additional mechanism, quantified via the apparent diffusion coefficient in Paper I and Paper II, appears to be much smaller than in mice [150]. While it is known that the CSF dynamics of mice and men differ, see, e.g., [134], this finding suggests that also the relative contribution of different molecular transport mechanisms *in the parenchyma* are substantially different between mice and men. This finding is particularly relevant given that most studies of the glymphatic system are based on imaging of rodents [86]. It implies that the conclusions drawn from imaging data of mice do not necessarily hold to the same degree in humans.

Furthermore, the subject–specific transport parameters obtained in Paper II show a substantial variation (a) between subjects (cf. Fig. 4c in Paper II), and (b) between different time points in the same subject (cf. Figs. 5d–f in Paper II). Since the subjects in Paper II are diagnosed with different neurological disorders, finding (a) may indicate that molecular brain transport mechanisms are altered or impaired in different ways in different diseases. Finding (b) indicates that these mechanisms may further depend significantly on the circadian rhythm and/or other physiological parameter such as posture. The latter effect was demonstrated experimentally in rats [94], and our findings indicate that this feature of the glymphatic concept translates to humans. This, in conclusion, supports the idea that glymphatic brain clearance in humans can – to some degree – be controlled and hence optimized by modifying external factors, such as the sleep rhythm, in everyday life.

1.11 Future work and outlook

The modeling presented in this thesis focused on molecular transport in the brain parenchyma. It is important to remember that there are various membranes in the brain across which there may be only selective transport of molecules (for example the blood–brain barrier). Hence, the movement of tracer seen in the images does not necessarily represent the dynamics of CSF. That being said, the techniques used and developed in this thesis can in the future also be applied to study the dynamics of CSF, e.g., in the ventricular system and the subarachnoid space, in greater detail. This is particularly interesting since the traditional view of the CSF moving from the choroid plexus through the ventricles to be absorbed into the bloodstream in the arachnoid villi (the "third circulation"[114]) has been questioned [17, 89]. Here, mathematical modeling combined with CSF tracer–enhanced MRI could provide novel insights into CSF pathways.

Such modeling would require different MRI data as analyzed in this thesis. This is because the MR protocols used to acquire these MRI make it difficult to quantify the concentration of tracer in the CSF itself. Luckily, the interest in using intrathecal CSF tracer–enhanced images to study the glymphatic system in humans has increased, and future studies may provide such data.

An example is an ongoing clinical study involving intrathecal CSF tracer injection and MR imaging in Parkinson patients as well as healthy control volunteers [59]. To the best of the author's knowledge, no such data has been reported in the literature as of March 2023. Hence, studies as [59] will provide novel data sets of MRI, including T_1–maps, from both healthy volunteers and patients. Such data can be expected to shed new light onto transport of fluid and molecules in the human brain. If this data becomes available to the modeling community, the techniques used and developed in this thesis can be used to address various interesting questions with possible clinical relevance.

For example, one could determine the subject-specific optimal transport parameters for the models presented in Paper II. The parameters can then be compared between patients and healthy volunteers, and it should be investigated if the estimated transport parameters are biomarkers for disease development in both patients and healthy subjects. In rats, inverse compartment modeling with MRI data has already shown differences in glymphatic transport parameters between healthy and diabetic animals [31]. Such investigations have the potential to shed new light on the relation between fluid transport in the brain and disease. If, for example, certain diseases are characterized by lower molecular transport parameters compared to healthy individuals, this would suggest to investigate therapeutic strategies that target the capacity of CSF to transport molecules in and out of the brain.

A limitation of the MRI data analyzed in this thesis is the spatial resolution of the images: therein, perivascular spaces are not distinguishable from the interstitium [149]. However, in T_2–weighted MRI with high field strength (7 T), perivascular spaces become visible. If future CSF tracer–enhanced MRI studies acquire such images as well, the method used in Paper II represent a meaningful way of testing the validity of the glymphatic hypothesis in humans: According

to the theory, transport should be dominated by advection in the PVS, and hence, the advective velocities obtained with our computational method should be highest around the PVS.

Regarding the technical aspects presented in this thesis, the current implementation of the MRI and mesh registration algorithm presented in Paper III is not optimized for speed. The results presented therein were computed on a cluster with 3 TB of RAM and required a computation time of roughly 16 days. This poses a drawback in application of the method, which can be mitigated by implementing the algorithm with GPU–acceleration. Given this implementation, there is potential to fine–tune the algorithm even further.

For example, we did not investigate the influence of smoothening the input images or test for time–dependent deformation velocity fields. It should in the future also be investigated to which extent the algorithm can be used to generate meshes for images that contain artifacts such as, e.g., images of patients with a brain tumor. Here, the algorithm might face challenges because the assumption of identical topology between input and target image might be invalid.

Finally, physics–informed neural networks as used in Paper I are a relatively new method as compared to, e.g., the finite element method. In the last years, many papers have been published that aim to overcome the main problem with PINNs, that is, to optimize the PINN loss function to obtain solutions with relative accuracy better than $\sim 10^{-4}$. The results presented in Paper I show that PINNs can in principle be used to solve challenging inverse problems using gMRI data, but careful hyperparameter tuning was needed to address overfitting. Future work should test new developments in the PINN community on such problems. Examples include greedy algorithms for PINN training [168], energy natural gradient based optimization of PINNs [120], temporal decomposition of PINNs [135], or advanced sampling strategies [191] as suggested by the results in Paper I. This will improve the applicability of PINNs for inverse modeling of brain data.

Once PINNs can be reliably trained without experience–based hyperparameter tuning, they may significantly simplify the pipeline from raw MRI data to physics-based modeling and thereby contribute to improved understanding of the glymphatic system.

A promising alternative to PINNs would be to consider other approaches combining PDE and neural networks such as Mesh Graph Nets [136] or hybrid NN–FEM models [117]. These approaches come with other challenges compared to PINNs, but might also prove useful and convenient in some inverse modeling problems related to brain clearance and MRI data.

Bibliography

[1] Abbott, N. J. “Evidence for bulk flow of brain interstitial fluid: significance for physiology and pathology”. In: *Neurochemistry international* vol. 45, no. 4 (2004), pp. 545–552.

[2] Abbott, N. J. et al. “The role of brain barriers in fluid movement in the CNS: is there a ‘glymphatic’system?” In: *Acta neuropathologica* vol. 135 (2018), pp. 387–407.

[3] Absinta, M. et al. “Human and nonhuman primate meninges harbor lymphatic vessels that can be visualized noninvasively by MRI”. In: *elife* vol. 6 (2017), e29738.

[4] Adams, R. et al. “Symptomatic occult hydrocephalus with normal cerebrospinal-fluid pressure: a treatable syndrome”. In: *New England Journal of Medicine* vol. 273, no. 3 (1965), pp. 117–126.

[5] Asgari, M., De Zélicourt, D., and Kurtcuoglu, V. “Glymphatic solute transport does not require bulk flow”. In: *Scientific reports* vol. 6, no. 1 (2016), p. 38635.

[6] Aspelund, A. et al. “A dural lymphatic vascular system that drains brain interstitial fluid and macromolecules”. In: *Journal of Experimental Medicine* vol. 212, no. 7 (2015), pp. 991–999.

[7] Attwell, D. and Laughlin, S. B. “An energy budget for signaling in the grey matter of the brain”. In: *Journal of Cerebral Blood Flow & Metabolism* vol. 21, no. 10 (2001), pp. 1133–1145.

[8] Bae, Y. J. et al. “Altered glymphatic system in idiopathic normal pressure hydrocephalus”. In: *Parkinsonism & Related Disorders* vol. 82 (2021), pp. 56–60.

[9] Bardin, J. “Making connections”. In: *Nature* vol. 483, no. 7390 (2012), p. 394.

[10] Baydin, A. G. et al. “Automatic differentiation in machine learning: a survey”. In: *Journal of Marchine Learning Research* vol. 18 (2018), pp. 1–43.

[11] Bèchet, N. B., Shanbhag, N. C., and Lundgaard, I. “Glymphatic pathways in the gyrencephalic brain”. In: *Journal of Cerebral Blood Flow & Metabolism* vol. 41, no. 9 (2021), pp. 2264–2279.

[12] Benveniste, H. et al. “Glymphatic cerebrospinal fluid and solute transport quantified by MRI and PET imaging”. In: *Neuroscience* vol. 474 (2021), pp. 63–79.

[13] Benveniste, H. et al. “The glymphatic system and waste clearance with brain aging: a review”. In: *Gerontology* vol. 65, no. 2 (2019), pp. 106–119.

[14] Bilston, L. E. et al. “Arterial pulsation-driven cerebrospinal fluid flow in the perivascular space: a computational model”. In: *Computer Methods in Biomechanics & Biomedical Engineering* vol. 6, no. 4 (2003), pp. 235–241.

[15] Blausen.com staff. “Medical gallery of Blausen Medical 2014”. In: *WikiJournal of Medicine* vol. 1, no. 2 (2014). DOI: DOI:10.15347/wjm/2014.010.

[16] Bojarskaite, L. et al. “Sleep cycle-dependent vascular dynamics in male mice and the predicted effects on perivascular cerebrospinal fluid flow and solute transport”. In: *Nature communications* vol. 14, no. 1 (2023), p. 953.

[17] Brinker, T. et al. “A new look at cerebrospinal fluid circulation”. In: *Fluids and Barriers of the CNS* vol. 11, no. 1 (2014), pp. 1–16.

[18] Bräutigam, K., Vakis, A., and Tsitsipanis, C. “Pathogenesis of idiopathic Normal Pressure Hydrocephalus: A review of knowledge”. In: *Journal of Clinical Neuroscience* vol. 61 (2019), pp. 10–13.

[19] Cai, S. et al. “Flow over an espresso cup: inferring 3-D velocity and pressure fields from tomographic background oriented Schlieren via physics-informed neural networks”. In: *Journal of Fluid Mechanics* vol. 915 (2021), A102.

[20] Cai, S. et al. “Physics-informed neural networks for heat transfer problems”. In: *Journal of Heat Transfer* vol. 143, no. 6 (2021).

[21] Carlstrom, L. P. et al. “A clinical primer for the glymphatic system”. In: *Brain* vol. 145, no. 3 (2022), pp. 843–857.

[22] Chen, X. et al. “Cerebral amyloid angiopathy is associated with glymphatic transport reduction and time-delayed solute drainage along the neck arteries”. In: *Nature aging* vol. 2, no. 3 (2022), pp. 214–223.

[23] Chong, P. L. et al. “Sleep, cerebrospinal fluid, and the glymphatic system: A systematic review”. In: *Sleep medicine reviews* vol. 61 (2022), p. 101572.

[24] Chung, T. J. et al. *Computational fluid dynamics*. Cambridge university press, 2002.

[25] Commons, C. *Attribution-NonCommercial-NoDerivatives 4.0 International (CC BY-NC-ND 4.0) License*. https://creativecommons.org/licenses/by-nc-nd/4.0/ [Accessed: 23.05.2023]. 2023.

[26] Cserr, H. F. and Ostrach, L. “Bulk flow of interstitial fluid after intracranial injection of blue dextran 2000”. In: *Experimental neurology* vol. 45, no. 1 (1974), pp. 50–60.

[27] Cuomo, S. et al. “Scientific machine learning through physics–informed neural networks: where we are and what’s next”. In: *Journal of Scientific Computing* vol. 92, no. 3 (2022), p. 88.

[28] Cushing, H. “Studies on the cerebro-spinal fluid: I. Introduction”. In: *The Journal of medical research* vol. 31, no. 1 (1914), p. 1.

[29] Cushing, H. et al. “The third circulation and its channels”. In: *Lancet* vol. 2, no. 851-857 (1925), p. 547.

[30] Daversin-Catty, C. et al. “The mechanisms behind perivascular fluid flow”. In: *Plos one* vol. 15, no. 12 (2020), e0244442.

[31] Davoodi-Bojd, E. et al. “Modeling glymphatic system of the brain using MRI”. In: *Neuroimage* vol. 188 (2019), pp. 616–627.

[32] Davson, H., Hollingsworth, G., and Segal, M. “The mechanism of drainage of the cerebrospinal fluid”. In: *Brain* vol. 93, no. 4 (1970), pp. 665–678.

[33] Daw, A. et al. “Rethinking the importance of sampling in physics-informed neural networks”. In: *arXiv preprint arXiv:2207.02338* (2022).

[34] Deisenhammer, F. et al. *Cerebrospinal fluid in clinical neurology*. Springer, 2015.

[35] Demiral, Ş. B. et al. “Apparent diffusion coefficient changes in human brain during sleep–does it inform on the existence of a glymphatic system?” In: *Neuroimage* vol. 185 (2019), pp. 263–273.

[36] Di Pietro, D. A. and Ern, A. *Mathematical aspects of discontinuous Galerkin methods*. Vol. 69. Springer Science & Business Media, 2011.

[37] Dissanayake, M. and Phan-Thien, N. “Neural-network-based approximations for solving partial differential equations”. In: *communications in Numerical Methods in Engineering* vol. 10, no. 3 (1994), pp. 195–201.

[38] Dreizen, P. “The Nobel prize for MRI: a wonderful discovery and a sad controversy”. In: *The Lancet* vol. 363, no. 9402 (2004), p. 78.

[39] Eide, P. K. and Ringstad, G. “MRI with intrathecal MRI gadolinium contrast medium administration: a possible method to assess glymphatic function in human brain”. In: *Acta radiologica open* vol. 4, no. 11 (2015), p. 2058460115609635.

[40] Eide, P. K. and Sorteberg, W. “Diagnostic intracranial pressure monitoring and surgical management in idiopathic normal pressure hydrocephalus: a 6-year review of 214 patients”. In: *Neurosurgery* vol. 66, no. 1 (2010), pp. 80–91.

[41] Eide, P. K. et al. “Altered glymphatic enhancement of cerebrospinal fluid tracer in individuals with chronic poor sleep quality”. In: *Journal of Cerebral Blood Flow & Metabolism* vol. 42, no. 9 (2022), pp. 1676–1692.

[42] Eide, P. K. et al. “Delayed clearance of cerebrospinal fluid tracer from choroid plexus in idiopathic normal pressure hydrocephalus”. In: *Journal of Cerebral Blood Flow & Metabolism* vol. 40, no. 9 (2020), pp. 1849–1858.

[43] Eide, P. K. et al. “Direction and magnitude of cerebrospinal fluid flow vary substantially across central nervous system diseases”. In: *Fluids and Barriers of the CNS* vol. 18, no. 1 (2021), pp. 1–18.

[44] Eide, P. K. et al. “Magnetic resonance imaging provides evidence of glymphatic drainage from human brain to cervical lymph nodes”. In: *Scientific reports* vol. 8, no. 1 (2018), pp. 1–10.

[45] Eide, P. K. et al. “Sleep deprivation impairs molecular clearance from the human brain”. In: *Brain* vol. 144, no. 3 (2021), pp. 863–874.

[46] Elam, J. S. et al. “The human connectome project: a retrospective”. In: *NeuroImage* vol. 244 (2021), p. 118543.

[47] Elkin, R. et al. “Optimal mass transport kinetic modeling for head and neck DCE-MRI: Initial analysis”. In: *Magnetic resonance in medicine* vol. 82, no. 6 (2019), pp. 2314–2325.

[48] Elmaoğlu, M. and Çelik, A. *MRI handbook: MR physics, patient positioning, and protocols*. Springer Science & Business Media, 2011.

[49] Enzmann, D. R. and Pelc, N. “Normal flow patterns of intracranial and spinal cerebrospinal fluid defined with phase-contrast cine MR imaging.” In: *Radiology* vol. 178, no. 2 (1991), pp. 467–474.

[50] Evans, L. C. *Partial differential equations*. Vol. 19. American Mathematical Society, 2022.

[51] Filippi, C. G. and Watts, R. “Imaging of Glymphatic Flow and Neurodegeneration”. In: *Hybrid PET/MR Neuroimaging: A Comprehensive Approach* (2022), pp. 849–860.

[52] Fischl, B. “FreeSurfer”. In: *Neuroimage* vol. 62, no. 2 (2012), pp. 774–781.

[53] Fletcher, R. *Practical methods of optimization*. John Wiley & Sons, 2013.

[54] Fultz, N. E. et al. “Coupled electrophysiological, hemodynamic, and cerebrospinal fluid oscillations in human sleep”. In: *Science* vol. 366, no. 6465 (2019), pp. 628–631.

[55] Gao, Z., Yan, L., and Zhou, T. “Failure-informed adaptive sampling for PINNs”. In: *arXiv preprint arXiv:2210.00279* (2022).

[56] Gauthier, S. et al. “World Alzheimer Report 2021: Journey through the diagnosis of dementia”. In: *Alzheimer’s Disease International* (2021), pp. 17–29.

[57] Glenner, G. G. and Wong, C. W. “Alzheimer’s disease: initial report of the purification and characterization of a novel cerebrovascular amyloid protein”. In: *Biochemical and biophysical research communications* vol. 120, no. 3 (1984), pp. 885–890.

[58] Greitz, D., Franck, A., and Nordell, B. “On the pulsatile nature of intracranial and spinal CSF-circulation demonstrated by MR imaging”. In: *Acta radiologica* vol. 34, no. 4 (1993), pp. 321–328.

[59] GRIP-study. *Det glymfatiske systems rolle i Parkinsons sykdom (GRIP-studien)*. URL: https://oslo-universitetssykehus.no/kliniske-studier/det-glymfatiske-systems-rolle-i-parkinsons-sykdom-grip-studien.

[60] Grisvard, P. *Elliptic problems in nonsmooth domains*. SIAM, 2011.

[61] Grossmann, T. G. et al. “Can Physics-Informed Neural Networks beat the Finite Element Method?” In: *arXiv preprint arXiv:2302.04107* (2023).

[62] Guo, J., Wang, H., and Hou, C. “A Novel Adaptive Causal Sampling Method for Physics-Informed Neural Networks”. In: *arXiv preprint arXiv:2210.12914* (2022).

[63] Hadamard, J. “Le problème de Cauchy et les équations aux dérivées partielles linéaires hyperboliques”. In: *Paris* vol. 11 (1932), pp. 243–264.

[64] Halperin, J. J. et al. “Practice guideline: Idiopathic normal pressure hydrocephalus: Response to shunting and predictors of response: Report of the Guideline Development, Dissemination, and Implementation Subcommittee of the American Academy of Neurology”. In: *Neurology* vol. 85, no. 23 (2015), pp. 2063–2071.

[65] Halvorsen, M. et al. “Off-label intrathecal use of gadobutrol: safety study and comparison of administration protocols”. In: *Neuroradiology* vol. 63 (2021), pp. 51–61.

[66] Harrison, I. F. et al. “Non-invasive imaging of CSF-mediated brain clearance pathways via assessment of perivascular fluid movement with diffusion tensor MRI”. In: *Elife* vol. 7 (2018), e34028.

[67] He, Q. et al. “Physics-informed neural networks for multiphysics data assimilation with application to subsurface transport”. In: *Advances in Water Resources* vol. 141 (2020), p. 103610.

[68] Herbowski, L. “The maze of the cerebrospinal fluid discovery”. In: *Anatomy Research International* vol. 2013 (2013).

[69] Hinze, M. et al. *Optimization with PDE constraints*. Vol. 23. Springer Science & Business Media, 2008.

[70] Hladky, S. B. and Barrand, M. A. “The glymphatic hypothesis: the theory and the evidence”. In: *Fluids and Barriers of the CNS* vol. 19, no. 1 (2022), pp. 1–33.

[71] Holter, K. E. et al. “Interstitial solute transport in 3D reconstructed neuropil occurs by diffusion rather than bulk flow”. In: *Proceedings of the National Academy of Sciences* vol. 114, no. 37 (2017), pp. 9894–9899.

[72] Hornkjol, M. et al. “CSF circulation and dispersion yield rapid clearance from intracranial compartments”. In: *bioRxiv* (2022), pp. 2022–05.

[73] Hovd, M. H. et al. “Population pharmacokinetic modeling of CSF to blood clearance: prospective tracer study of 161 patients under work-up for CSF disorders”. In: *Fluids and Barriers of the CNS* vol. 19, no. 1 (2022), pp. 1–14.

[74] Hsu, J.-L. et al. “Magnetic resonance images implicate that glymphatic alterations mediate cognitive dysfunction in Alzheimer disease”. In: *Annals of Neurology* vol. 93, no. 1 (2023), pp. 164–174.

[75] Iliff, J. J. et al. “A paravascular pathway facilitates CSF flow through the brain parenchyma and the clearance of interstitial solutes, including amyloid β”. In: *Science translational medicine* vol. 4, no. 147 (2012), 147ra111–147ra111.

[76] Iliff, J. J. et al. “Brain-wide pathway for waste clearance captured by contrast-enhanced MRI”. In: *The Journal of clinical investigation* vol. 123, no. 3 (2013), pp. 1299–1309.

[77] Jiao, Y. et al. “A rate of convergence of Physics Informed Neural Networks for the linear second order elliptic PDEs”. In: *arXiv preprint arXiv:2109.01780* (2021).

[78] Jinkins, J. R. et al. “Intrathecal gadolinium-enhanced MR cisternography in the evaluation of clinically suspected cerebrospinal fluid rhinorrhea in humans: early experience”. In: *Radiology* vol. 222, no. 2 (2002), pp. 555–559.

[79] Johnson, C. *Numerical solution of partial differential equations by the finite element method*. Courier Corporation, 2012.

[80] Johnston, M. and Papaiconomou, C. “Cerebrospinal fluid transport: a lymphatic perspective”. In: *Physiology* vol. 17, no. 6 (2002), pp. 227–230.

[81] Karniadakis, G. E. et al. “Physics-informed machine learning”. In: *Nature Reviews Physics* vol. 3, no. 6 (2021), pp. 422–440.

[82] Kaur, J. et al. “Magnetic resonance imaging and modeling of the glymphatic system”. In: *Diagnostics* vol. 10, no. 6 (2020), p. 344.

[83] Kedarasetti, R. T., Drew, P. J., and Costanzo, F. “Arterial vasodilation drives convective fluid flow in the brain: a poroelastic model”. In: *Fluids and Barriers of the CNS* vol. 19, no. 1 (2022), pp. 1–24.

[84] Keith Sharp, M., Carare, R. O., and Martin, B. A. “Dispersion in porous media in oscillatory flow between flat plates: applications to intrathecal, periarterial and paraarterial solute transport in the central nervous system”. In: *Fluids and Barriers of the CNS* vol. 16, no. 1 (2019), pp. 1–17.

[85] Kelley, D. H. and Thomas, J. H. “Cerebrospinal fluid flow”. In: *Annual Review of Fluid Mechanics* vol. 55 (2023).

[86] Kelley, D. H. et al. “The glymphatic system: Current understanding and modeling”. In: *Iscience* (2022), p. 104987.

[87] Kingma, D. P. and Ba, J. “Adam: A method for stochastic optimization”. In: *arXiv preprint arXiv:1412.6980* (2014).

[88] Kiviniemi, V. et al. “Ultra-fast magnetic resonance encephalography of physiological brain activity–glymphatic pulsation mechanisms?” In: *Journal of Cerebral Blood Flow & Metabolism* vol. 36, no. 6 (2016), pp. 1033–1045.

[89] Klarica, M., Radoš, M., and Orešković, D. "The movement of cerebrospinal fluid and its relationship with substances behavior in cerebrospinal and interstitial fluid". In: *Neuroscience* vol. 414 (2019), pp. 28–48.

[90] Koundal, S. et al. "Optimal mass transport with lagrangian workflow reveals advective and diffusion driven solute transport in the glymphatic system". In: *Scientific reports* vol. 10, no. 1 (2020), p. 1990.

[91] Ladd, M. E. et al. "Pros and cons of ultra-high-field MRI/MRS for human application". In: *Progress in nuclear magnetic resonance spectroscopy* vol. 109 (2018), pp. 1–50.

[92] Lagaris, I. E., Likas, A., and Fotiadis, D. I. "Artificial neural networks for solving ordinary and partial differential equations". In: *IEEE transactions on neural networks* vol. 9, no. 5 (1998), pp. 987–1000.

[93] Le Bihan, D. and Johansen-Berg, H. "Diffusion MRI at 25: exploring brain tissue structure and function". In: *Neuroimage* vol. 61, no. 2 (2012), pp. 324–341.

[94] Lee, H. et al. "The effect of body posture on brain glymphatic transport". In: *Journal of Neuroscience* vol. 35, no. 31 (2015), pp. 11034–11044.

[95] Leon, M. J. de et al. "Cerebrospinal fluid clearance in Alzheimer disease measured with dynamic PET". In: *Journal of Nuclear Medicine* vol. 58, no. 9 (2017), pp. 1471–1476.

[96] Liu, D. C. and Nocedal, J. "On the limited memory BFGS method for large scale optimization". In: *Mathematical programming* vol. 45, no. 1 (1989), pp. 503–528.

[97] Liu, S., Huang, X., and Protopapas, P. "Evaluating Error Bound for Physics-Informed Neural Networks on Linear Dynamical Systems". In: *arXiv preprint arXiv:2207.01114* (2022).

[98] Lohela, T. J., Lilius, T. O., and Nedergaard, M. "The glymphatic system: implications for drugs for central nervous system diseases". In: *Nature Reviews Drug Discovery* vol. 21, no. 10 (2022), pp. 763–779.

[99] Long, J. M. and Holtzman, D. M. "Alzheimer disease: an update on pathobiology and treatment strategies". In: *Cell* vol. 179, no. 2 (2019), pp. 312–339.

[100] Louveau, A. et al. "Structural and functional features of central nervous system lymphatic vessels". In: *Nature* vol. 523, no. 7560 (2015), pp. 337–341.

[101] Lu, L. et al. "DeepXDE: A deep learning library for solving differential equations". In: *SIAM review* vol. 63, no. 1 (2021), pp. 208–228.

[102] Lun, M. P., Monuki, E. S., and Lehtinen, M. K. "Development and functions of the choroid plexus–cerebrospinal fluid system". In: *Nature Reviews Neuroscience* vol. 16, no. 8 (2015), pp. 445–457.

[103] MacAulay, N., Hamann, S., and Zeuthen, T. “Water transport in the brain: role of cotransporters”. In: *Neuroscience* vol. 129, no. 4 (2004), pp. 1029–1042.

[104] Maddu, S. et al. “Inverse Dirichlet weighting enables reliable training of physics informed neural networks”. en. In: *Machine Learning: Science and Technology* vol. 3, no. 1 (Feb. 2022). Publisher: IOP Publishing, p. 015026. DOI: 10.1088/2632-2153/ac3712.

[105] Mao, Z. and Meng, X. “Physics-informed neural networks with residual/gradient-based adaptive sampling methods for solving PDEs with sharp solutions”. In: *arXiv preprint arXiv:2302.08035* (2023).

[106] Marasco, R. A. “Current and evolving treatment strategies for the Alzheimer disease continuum.” In: *The American Journal of Managed Care* vol. 26, no. 8 Suppl (2020), S167–S176.

[107] Mardal, K.-A. et al. *Software for Mathematical modeling of the human brain - from magnetic resonance images to finite element simulation*. Version v2.0. June 2021. DOI: 10.5281/zenodo.4899490.

[108] Mardal, K.-A. et al. *Mathematical Modeling of the Human Brain: From Magnetic Resonance Images to Finite Element Simulation*. 2022.

[109] Markram, H. “The human brain project”. In: *Scientific American* vol. 306, no. 6 (2012), pp. 50–55.

[110] Martinac, A. D. and Bilston, L. E. “Computational modelling of fluid and solute transport in the brain”. In: *Biomechanics and modeling in mechanobiology* vol. 19 (2020), pp. 781–800.

[111] Meer, R. van der, Oosterlee, C., and Borovykh, A. “Optimally weighted loss functions for solving PDEs with Neural Networks”. In: *arXiv:2002.06269 [cs, math]* (Mar. 2021). arXiv: 2002.06269.

[112] Mestre, H., Mori, Y., and Nedergaard, M. “The brain’s glymphatic system: current controversies”. In: *Trends in neurosciences* vol. 43, no. 7 (2020), pp. 458–466.

[113] Mestre, H. et al. “Flow of cerebrospinal fluid is driven by arterial pulsations and is reduced in hypertension”. In: *Nature communications* vol. 9, no. 1 (2018), p. 4878.

[114] Milhorat, T. H. “The third circulation revisited”. In: *Journal of neurosurgery* vol. 42, no. 6 (1975), pp. 628–645.

[115] Mishra, S. and Molinaro, R. “Estimates on the generalization error of physics-informed neural networks for approximating a class of inverse problems for PDEs”. In: *IMA Journal of Numerical Analysis* vol. 42, no. 2 (2022), pp. 981–1022.

[116] Mitusch, S. K., Funke, S. W., and Dokken, J. S. “dolfin-adjoint 2018.1: automated adjoints for FEniCS and Firedrake”. In: *Journal of Open Source Software* vol. 4, no. 38 (2019), p. 1292.

[117] Mitusch, S. K., Funke, S. W., and Kuchta, M. “Hybrid FEM-NN models: Combining artificial neural networks with the finite element method”. In: *Journal of Computational Physics* vol. 446 (2021), p. 110651.

[118] Mokri, B. “The Monro–Kellie hypothesis: applications in CSF volume depletion”. In: *Neurology* vol. 56, no. 12 (2001), pp. 1746–1748.

[119] Mott, F. “The Oliver-Sharpey lectures on the cerebrospinal fluid”. In: *Lancet* vol. 2, no. 1 (1910), p. 79.

[120] Müller, J. and Zeinhofer, M. “Achieving High Accuracy with PINNs via Energy Natural Gradients”. In: *arXiv preprint arXiv:2302.13163* (2023).

[121] Müller, J. and Zeinhofer, M. “Notes on exact boundary values in residual minimisation”. In: *Mathematical and Scientific Machine Learning*. PMLR. 2022, pp. 231–240.

[122] Møllgård, K. et al. “A mesothelium divides the subarachnoid space into functional compartments”. In: *Science* vol. 379, no. 6627 (2023), pp. 84–88.

[123] Naganawa, S. and Taoka, T. “The glymphatic system: a review of the challenges in visualizing its structure and function with MR imaging”. In: *Magnetic Resonance in Medical Sciences* vol. 21, no. 1 (2022), pp. 182–194.

[124] Naganawa, S. et al. “Gd-based contrast enhancement of the perivascular spaces in the basal ganglia”. In: *Magnetic Resonance in Medical Sciences* vol. 16, no. 1 (2017), p. 61.

[125] Naganawa, S. et al. “Serial scans in healthy volunteers following intravenous administration of gadoteridol: time course of contrast enhancement in various cranial fluid spaces”. In: *Magnetic Resonance in Medical Sciences* vol. 13, no. 1 (2014), pp. 7–13.

[126] Nassar, B. R. and Lippa, C. F. “Idiopathic normal pressure hydrocephalus: a review for general practitioners”. In: *Gerontology and geriatric medicine* vol. 2 (2016), p. 2333721416643702.

[127] Nedergaard, M. “Garbage truck of the brain”. In: *Science* vol. 340, no. 6140 (2013), pp. 1529–1530.

[128] Nedergaard, M. and Goldman, S. A. “Glymphatic failure as a final common pathway to dementia”. In: *Science* vol. 370, no. 6512 (2020), pp. 50–56.

[129] Nicholson, C. “Diffusion and related transport mechanisms in brain tissue”. In: *Reports on progress in Physics* vol. 64, no. 7 (2001), p. 815.

[130] Nicholson, C. and Hrabětová, S. “Brain extracellular space: the final frontier of neuroscience”. In: *Biophysical journal* vol. 113, no. 10 (2017), pp. 2133–2142.

[131] Obersteiner, H. *The anatomy of the central nervous organs in health and disease*. Griffin, 1900.

[132] Orešković, D. and Klarica, M. "A new look at cerebrospinal fluid movement". In: *Fluids and Barriers of the CNS* vol. 11 (2014), pp. 1–3.

[133] Panza, F. et al. "A critical appraisal of amyloid-β-targeting therapies for Alzheimer disease". In: *Nature Reviews Neurology* vol. 15, no. 2 (2019), pp. 73–88.

[134] Pardridge, W. M. "CSF, blood-brain barrier, and brain drug delivery". In: *Expert opinion on drug delivery* vol. 13, no. 7 (2016), pp. 963–975.

[135] Penwarden, M. et al. "A unified scalable framework for causal sweeping strategies for Physics-Informed Neural Networks (PINNs) and their temporal decompositions". In: *arXiv preprint arXiv:2302.14227* (2023).

[136] Pfaff, T. et al. "Learning mesh-based simulation with graph networks". In: *arXiv preprint arXiv:2010.03409* (2020).

[137] Pooley, R. A. "Fundamental physics of MR imaging". In: *Radiographics* vol. 25, no. 4 (2005), pp. 1087–1099.

[138] Postelnicu, G., Zollei, L., and Fischl, B. "Combined volumetric and surface registration". In: *IEEE transactions on medical imaging* vol. 28, no. 4 (2008), pp. 508–522.

[139] Poulain, A., Riseth, J., and Vinje, V. "Multi-compartmental model of glymphatic clearance of solutes in brain tissue". In: *Plos one* vol. 18, no. 3 (2023), e0280501.

[140] Proulx, S. T. "Cerebrospinal fluid outflow: a review of the historical and contemporary evidence for arachnoid villi, perineural routes, and dural lymphatics". In: *Cellular and Molecular Life Sciences* vol. 78, no. 6 (2021), pp. 2429–2457.

[141] Psichogios, D. C. and Ungar, L. H. "A hybrid neural network-first principles approach to process modeling". In: *AIChE Journal* vol. 38, no. 10 (1992), pp. 1499–1511.

[142] Quarteroni, A. and Valli, A. *Numerical approximation of partial differential equations*. Vol. 23. Springer Science & Business Media, 2008.

[143] Raissi, M., Perdikaris, P., and Karniadakis, G. E. "Physics-informed neural networks: A deep learning framework for solving forward and inverse problems involving nonlinear partial differential equations". In: *Journal of Computational physics* vol. 378 (2019), pp. 686–707.

[144] Raper, D., Louveau, A., and Kipnis, J. "How do meningeal lymphatic vessels drain the CNS?" In: *Trends in neurosciences* vol. 39, no. 9 (2016), pp. 581–586.

[145] Rasmussen, M. K., Mestre, H., and Nedergaard, M. "Fluid transport in the brain". In: *Physiological Reviews* vol. 102, no. 2 (2022), pp. 1025–1151.

[146] Rasmussen, M. K., Mestre, H., and Nedergaard, M. "The glymphatic pathway in neurological disorders". In: *The Lancet Neurology* vol. 17, no. 11 (2018), pp. 1016–1024.

[147] Ratner, V. et al. “Cerebrospinal and interstitial fluid transport via the glymphatic pathway modeled by optimal mass transport”. In: *Neuroimage* vol. 152 (2017), pp. 530–537.

[148] Ray, L., Iliff, J. J., and Heys, J. J. “Analysis of convective and diffusive transport in the brain interstitium”. In: *Fluids and Barriers of the CNS* vol. 16, no. 1 (2019), pp. 1–18.

[149] Ray, L. A. and Heys, J. J. “Fluid flow and mass transport in brain tissue”. In: *Fluids* vol. 4, no. 4 (2019), p. 196.

[150] Ray, L. A. et al. “Quantitative analysis of macroscopic solute transport in the murine brain”. In: *Fluids and Barriers of the CNS* vol. 18, no. 1 (2021), pp. 1–19.

[151] Raz, E. et al. “Possible empirical evidence of glymphatic system on computed tomography after endovascular perforations”. In: *World Neurosurgery* vol. 134 (2020), e400–e404.

[152] Reardon, S. “FDA approves Alzheimer’s drug lecanemab amid safety concerns”. In: *Nature* vol. 613, no. 7943 (2023), pp. 227–228.

[153] Reeves, B. C. et al. “Glymphatic system impairment in Alzheimer’s disease and idiopathic normal pressure hydrocephalus”. In: *Trends in Molecular Medicine* vol. 26, no. 3 (2020), pp. 285–295.

[154] Reiche, W. et al. “MR cisternography after intrathecal Gd-DTPA application”. In: *European radiology* vol. 12 (2002), pp. 2943–2949.

[155] Relkin, N. et al. “Diagnosing idiopathic normal-pressure hydrocephalus”. In: *Neurosurgery* vol. 57, no. suppl_3 (2005), S2–4.

[156] Rennels, M. L. et al. “Evidence for a ‘paravascular’fluid circulation in the mammalian central nervous system, provided by the rapid distribution of tracer protein throughout the brain from the subarachnoid space”. In: *Brain research* vol. 326, no. 1 (1985), pp. 47–63.

[157] Reuter, M., Rosas, H. D., and Fischl, B. “Highly accurate inverse consistent registration: a robust approach”. In: *Neuroimage* vol. 53, no. 4 (2010), pp. 1181–1196.

[158] Ringstad, G., Vatnehol, S. A. S., and Eide, P. K. “Glymphatic MRI in idiopathic normal pressure hydrocephalus”. In: *Brain* vol. 140, no. 10 (2017), pp. 2691–2705.

[159] Ringstad, G. et al. “Brain-wide glymphatic enhancement and clearance in humans assessed with MRI”. In: *JCI insight* vol. 3, no. 13 (2018).

[160] Rohrhofer, F. M., Posch, S., and Geiger, B. C. “On the pareto front of physics-informed neural networks”. In: *arXiv preprint arXiv:2105.00862* (2021).

[161] Rosenberg, G., Kyner, W. T., and Estrada, E. “Bulk flow of brain interstitial fluid under normal and hyperosmolar conditions”. In: *American Journal of Physiology-Renal Physiology* vol. 238, no. 1 (1980), F42–F49.

[162] Sadigh-Eteghad, S. et al. “Amyloid-beta: a crucial factor in Alzheimer’s disease”. In: *Medical principles and practice* vol. 24, no. 1 (2015), pp. 1–10.

[163] Selcuk, H. et al. “Intrathecal gadolinium-enhanced MR cisternography in the evaluation of CSF leakage”. In: *American journal of neuroradiology* vol. 31, no. 1 (2010), pp. 71–75.

[164] Selkoe, D. J. and Hardy, J. “The amyloid hypothesis of Alzheimer’s disease at 25 years”. In: *EMBO molecular medicine* vol. 8, no. 6 (2016), pp. 595–608.

[165] Shin, Y., Darbon, J., and Karniadakis, G. E. “On the convergence of physics informed neural networks for linear second-order elliptic and parabolic type PDEs”. In: *arXiv preprint arXiv:2004.01806* (2020).

[166] Shin, Y., Zhang, Z., and Karniadakis, G. E. “Error estimates of residual minimization using neural networks for linear PDEs”. In: *arXiv preprint arXiv:2010.08019* (2020).

[167] Shokri-Kojori, E. et al. “β-Amyloid accumulation in the human brain after one night of sleep deprivation”. In: *Proceedings of the National Academy of Sciences* vol. 115, no. 17 (2018), pp. 4483–4488.

[168] Siegel, J. W. et al. “Greedy Training Algorithms for Neural Networks and Applications to PDEs”. In: *arXiv preprint arXiv:2107.04466* (2021).

[169] Smith, A. J. and Verkman, A. S. “Going against the flow: Interstitial solute transport in brain is diffusive and aquaporin-4 independent”. In: *The Journal of physiology* vol. 597, no. 17 (2019), p. 4421.

[170] Smith, A. J. et al. “Test of the’glymphatic’hypothesis demonstrates diffusive and aquaporin-4-independent solute transport in rodent brain parenchyma”. In: *elife* vol. 6 (2017), e27679.

[171] Soares, J. M. et al. “A hitchhiker’s guide to diffusion tensor imaging”. In: *Frontiers in neuroscience* vol. 7 (2013), p. 31.

[172] Spector, R., Snodgrass, S. R., and Johanson, C. E. “A balanced view of the cerebrospinal fluid composition and functions: Focus on adult humans”. In: *Experimental neurology* vol. 273 (2015), pp. 57–68.

[173] Spijkerman, J. M. et al. “Phase contrast MRI measurements of net cerebrospinal fluid flow through the cerebral aqueduct are confounded by respiration”. In: *Journal of Magnetic Resonance Imaging* vol. 49, no. 2 (2019), pp. 433–444.

[174] Syková, E. and Nicholson, C. “Diffusion in brain extracellular space”. In: *Physiological reviews* vol. 88, no. 4 (2008), pp. 1277–1340.

[175] Taoka, T. et al. “Evaluation of glymphatic system activity with the diffusion MR technique: diffusion tensor image analysis along the perivascular space (DTI-ALPS) in Alzheimer’s disease cases”. In: *Japanese journal of radiology* vol. 35 (2017), pp. 172–178.

[176] Tarasoff-Conway, J. M. et al. “Clearance systems in the brain—implications for Alzheimer disease”. In: *Nature reviews neurology* vol. 11, no. 8 (2015), pp. 457–470.

[177] Taylor, A. J. et al. “T1 mapping: basic techniques and clinical applications”. In: *JACC: Cardiovascular Imaging* vol. 9, no. 1 (2016), pp. 67–81.

[178] Tikhonov, A. N. et al. *Numerical methods for the solution of ill-posed problems*. Vol. 328. Springer Science & Business Media, 1995.

[179] Tithof, J. et al. “A network model of glymphatic flow under different experimentally-motivated parametric scenarios”. In: *Iscience* vol. 25, no. 5 (2022), p. 104258.

[180] Troyetsky, D. E. et al. “Dispersion as a waste-clearance mechanism in flow through penetrating perivascular spaces in the brain”. In: *Scientific reports* vol. 11, no. 1 (2021), p. 4595.

[181] Tröltzsch, F. *Optimal control of partial differential equations: theory, methods, and applications*. Vol. 112. American Mathematical Soc., 2010.

[182] Valnes, L. M. et al. “Apparent diffusion coefficient estimates based on 24 hours tracer movement support glymphatic transport in human cerebral cortex”. In: *Scientific reports* vol. 10, no. 1 (2020), pp. 1–12.

[183] Van Dyck, C. H. et al. “Lecanemab in early Alzheimer’s disease”. In: *New England Journal of Medicine* vol. 388, no. 1 (2023), pp. 9–21.

[184] Vardakis, J. C. et al. “Exploring neurodegenerative disorders using a novel integrated model of cerebral transport: Initial results”. In: *Proceedings of the Institution of Mechanical Engineers, Part H: Journal of Engineering in Medicine* vol. 234, no. 11 (2020), pp. 1223–1234.

[185] Wang, S., Wang, H., and Perdikaris, P. “On the eigenvector bias of Fourier feature networks: From regression to solving multi-scale PDEs with physics-informed neural networks”. en. In: *arXiv:2012.10047 [cs, stat]* (Dec. 2020). arXiv: 2012.10047.

[186] Wang, S., Yu, X., and Perdikaris, P. “When and why PINNs fail to train: A neural tangent kernel perspective”. en. In: *Journal of Computational Physics* vol. 449 (Jan. 2022), p. 110768. DOI: 10.1016/j.jcp.2021.110768.

[187] Wardlaw, J. M. et al. “Perivascular spaces in the brain: anatomy, physiology and pathology”. In: *Nature Reviews Neurology* vol. 16, no. 3 (2020), pp. 137–153.

[188] Watts, R. et al. “Measuring glymphatic flow in man using quantitative contrast-enhanced MRI”. In: *American Journal of Neuroradiology* vol. 40, no. 4 (2019), pp. 648–651.

[189] Weed, L. H. “The cerebrospinal fluid”. In: *Physiological reviews* vol. 2, no. 2 (1922), pp. 171–203.

[190] Williams, M. A. and Malm, J. “Diagnosis and treatment of idiopathic normal pressure hydrocephalus”. In: *Continuum: Lifelong Learning in Neurology* vol. 22, no. 2 Dementia (2016), p. 579.

[191] Wu, C. et al. “A comprehensive study of non-adaptive and residual-based adaptive sampling for physics-informed neural networks”. In: *Computer Methods in Applied Mechanics and Engineering* vol. 403 (2023), p. 115671.

[192] Wu, W. et al. “Effective Data Sampling Strategies and Boundary Condition Constraints of Physics-Informed Neural Networks for Identifying Material Properties in Solid Mechanics”. In: *arXiv preprint arXiv:2211.15423* (2022).

[193] Xie, L. et al. “Sleep drives metabolite clearance from the adult brain”. In: *science* vol. 342, no. 6156 (2013), pp. 373–377.

[194] Yang, L. et al. “Evaluating glymphatic pathway function utilizing clinically relevant intrathecal infusion of CSF tracer”. In: *Journal of translational medicine* vol. 11, no. 1 (2013), pp. 1–9.

[195] Yang, Z., Qiu, Z., and Fu, D. “DMIS: Dynamic Mesh-based Importance Sampling for Training Physics-Informed Neural Networks”. In: *arXiv preprint arXiv:2211.13944* (2022).

[196] Yokota, H. et al. “Diagnostic performance of glymphatic system evaluation using diffusion tensor imaging in idiopathic normal pressure hydrocephalus and mimickers”. In: *Current Gerontology and Geriatrics Research* vol. 2019 (2019), pp. 1–10.

[197] Zhou, Y. et al. “Impairment of the glymphatic pathway and putative meningeal lymphatic vessels in the aging human”. In: *Annals of neurology* vol. 87, no. 3 (2020), pp. 357–369.

Papers

Paper I

Investigating molecular transport in the human brain from MRI with physics-informed neural networks

Bastian Zapf, Johannes Haubner, Miroslav Kuchta, Geir Ringstad, Per Kristian Eide, Kent-Andre Mardal

Published in *Scientific Reports*, September 2022, volume 12, issue 1, pp. p.15475-15475. DOI: 10.1038/s41598-022-19157-w.

scientific reports

Check for updates

OPEN

Investigating molecular transport in the human brain from MRI with physics-informed neural networks

Bastian Zapf[1], Johannes Haubner[2], Miroslav Kuchta[2], Geir Ringstad[3,4], Per Kristian Eide[5,6] & Kent-Andre Mardal[1,2]✉

In recent years, a plethora of methods combining neural networks and partial differential equations have been developed. A widely known example are physics-informed neural networks, which solve problems involving partial differential equations by training a neural network. We apply physics-informed neural networks and the finite element method to estimate the diffusion coefficient governing the long term spread of molecules in the human brain from magnetic resonance images. Synthetic testcases are created to demonstrate that the standard formulation of the physics-informed neural network faces challenges with noisy measurements in our application. Our numerical results demonstrate that the residual of the partial differential equation after training needs to be small for accurate parameter recovery. To achieve this, we tune the weights and the norms used in the loss function and use residual based adaptive refinement of training points. We find that the diffusion coefficient estimated from magnetic resonance images with physics-informed neural networks becomes consistent with results from a finite element based approach when the residuum after training becomes small. The observations presented here are an important first step towards solving inverse problems on cohorts of patients in a semi-automated fashion with physics-informed neural networks.

In the recent years there has been tremendous activity and developments in combining machine learning with physics-based models in the form of partial differential equations (PDE). This activity has lead to the emergence of the discipline "physics-informed machine learning"[1]. Therein, nowadays, arguably one of the most popular approaches are physics-informed neural networks (PINNs)[2–4]. They combine PDE and boundary/initial condition into a non-convex optimization problem which can be implemented and solved using mature machine learning frameworks while easily leveraging modern hardware (e.g. GPU-accelerators). One of the benefits of the PINN compared to traditional numerical methods for PDE is that no computational mesh is required. Further, inverse PDE problems are solved in the same fashion as forward problems in PINNs. The only modifications to the code are to add the unknown PDE parameters one seeks to recover to the set of optimization parameters and an additional data-discrepancy term to the objective function. The PINN training process, however, is challenging and can require significant computing resources. Several works have put forward approaches to address this issue, among them extreme learning machines[5], importance sampling[6] and adaptive activation functions[7]. Another challenge in training PINNs is balancing boundary, initial and PDE loss terms. This challenge has been addressed by adaptive weighting strategies[8–11], as well as theory of functional connections[12,13]. Despite these challenges, the effectiveness of the method has been demonstrated in a wide range of works, examples include turbulent flows[14], heat transfer[15], epidemiological compartmental models[16] or stiff chemical systems[17].

Among other approaches[18–20], PINNs can be used to discover unknown physics from data. In the context of computational fluid dynamics, PINNs have been successfully applied in inverse problems using simulated data, see, e.g.,[14,21–24] and real data[25,26]. A comprehensive review on PINNs for fluid dynamics can be found in[27].

[1]Faculty of Mathematics and Natural Sciences, University of Oslo, 0851 Oslo, Norway. [2]Department of Numerical Analysis and Scientific Computing, Simula Research Laboratory, 0164 Oslo, Norway. [3]Department of Radiology, Oslo University Hospital, 0372 Oslo, Norway. [4]Department of Geriatrics and Internal medicine, Sorlandet Hospital, 4838 Arendal, Norway. [5]Department of Neurosurgery, Oslo University Hospital, 0372 Oslo, Norway. [6]Institute of Clinical Medicine, University of Oslo, 0372 Oslo, Norway. ✉email: kent-and@simula.no

In this work, we solve an inverse biomedical flow problem in 4D with unprocessed, noisy and temporally sparse MRI data on a complex domain. Classical approaches require careful meshing of the brain geometry and making assumptions on the boundary conditions[28]. In patient-specific brain modeling the meshing is particularly challenging and requires careful evaluation of the generated meshes[29]. Physics-informed neural networks have been applied for the discovery of unknown physics from data without meshing and without regularization[3]. This makes the PINN method an appealing and promising approach that avoids major challenges in our application and is therefore well worth investigation. However, PINNs introduce other challenges such as the choice of the network architecture, the optimization algorithm and hyperparameter tuning, e.g., weight factors in the loss function. Nevertheless, it is worth to examine how PINNs perform compared to classical algorithms in our application.

We aim to perform a computational investigation of the glymphatic theory based on and similar to[28,30] with PINNs. We apply them to model the fluid mechanics involved in brain clearance. Various kinds of dementia have recently been linked to a malfunctioning waste-clearance system - the so-called glymphatic system[31]. In this system, peri-vascular flow of cerebrospinal fluid (CSF) plays a crucial role either through bulk flow, dispersion or even as a mediator of pressure gradients through the interstitium[32]. While imaging of molecular transport in either rodents[33] or humans[34] points towards accelerated clearance through the glymphatic system, the detailed mechanisms involved in the system are currently debated[35–40].

Our approach builds on previous work where the estimated apparent diffusion coefficient (ADC) for the distribution of gadobutrol tracer molecules over 2 days, as seen in T1-weighted magnetic resonance images (MRI) at certain time points, is compared with the ADC estimated from diffusion tensor images (DTI)[28]. The ADC of gadobutrol was estimated from the T1-weighted images based on simulations using the finite element method (FEM) for optimal control of the diffusion equation. The findings were then compared to estimates of the apparent diffusion coefficient based on DTI. The latter is a magnetic resonance imaging technique that measures the diffusion tensor of water on short time scales, which in turn can then be used to estimate the diffusion tensor for other molecules, such as gadobutrol[28]. The limited amount of available data prevents from quantifying the uncertainty in the recovered parameters, and makes it a challenging test case for comparing PINNs and finite element based approaches.

Among other works involving physics-informed neural networks and MRI data[41,42] several works have previously demonstrated the effectiveness of PINNs in inverse problems related to our application. PINNs have been applied to estimate physiological parameters from clinical data using ordinary differential equation models[43], but we here consider a PDE model. Parameter identification problems involving MRI data and PDE have been solved using PINNs[26,44], but the geometries are reduced to 1-D and hence, taking into account the time dependence of the solution, an effectively two-dimensional problem is solved. Both approaches further involve a data smoothening preprocessing step.

To the best of our knowledge, this work is the first to estimate physiological parameters from temporally sparse, unsmoothened MRI data in a complex domain using a 4-D PDE model with PINNs. We start to verify the PINNs approach on carefully manufactured synthetic data, before working on real data. The synthetic testcases reveal challenges that occur for the PINNs due to noise in the data and the sensitivity of the neural network training procedure to different choices of hyperparameters. For all of the chosen hyperparameter settings, we evaluate the accuracy of the recovered diffusion coefficient based on the value of the PDE and data loss. For the synthetic test case, as well as for the real test case, it is required to ensure vanishing PDE loss in order to be consistent with the finite element approach. The question on how this is achieved is addressed by heuristics. We investigate using the ℓ^1-norm instead of ℓ^2-norm for the PDE loss as an alternative to avoid the overfitting. We further discuss how to solve additional challenges that arise when applying the PINNs to real MRI data. Throughout the paper, we solve the problem with both PINNs and FEM.

Problem statement

Given a set of concentration measurements $c^d(x_j, t_i)$ at four discrete time points $t_i \in \{0, 7, 24, 46\}$ h and voxel center coordinates $x_j \in \Omega$, where $\Omega \subset \mathbb{R}^3$ represents a subregion of the brain, we seek to find the apparent diffusion coefficient $D > 0$ such that a measure $J(c, c^d)$ for the discrepancy to the measurement is minimized under the constraint that $c(x, t)$ fulfills

$$\frac{\partial}{\partial t} c = D\Delta c \quad \text{in } \Omega \times (0, T). \tag{1}$$

The apparent diffusion coefficient takes into account the tortuosity λ of the extracellular space of the brain and relates to the free diffusion coefficient $D_f = \lambda^2 D$[46]. Similar to Valnes et al.[28] we here make the simplifying assumption of a spatially constant scalar diffusion coefficient. Diffusion of molecules in the brain matter is known to be anisotropic[46,47]. In Supplementary Section S2 online we assess the anisotropy in the white matter for the patient under consideration in this work. The fractional anisotropy is 0.27 ± 0.15 in Ω, indicating that molecular diffusion is rather isotropic. Moreover, we show there that simulations based on anisotropic, inhomogeneous DTI are, up to relative error of 9 %, comparable to simulations based on the patient-specific isotropic, homogeneous mean diffusion coefficient. This serves as justification for the simplifying assumption of a constant diffusion coefficient used in this work. The initial and boundary conditions required for the PDE (1) to have a unique solution are only partially known, and the differing ways in which we choose to incorporate them into the the PINN and FEM approaches are described in sections "The PINN approach" and "The finite element approach".

Our workflow to solve this problem on MRI data is illustrated in Fig. 1. Figure 2a illustrates the white matter subregion $\Omega \subset \mathbb{R}^3$ we consider in this work. Figure 2b shows a slice view of the concentration after 24 h for the

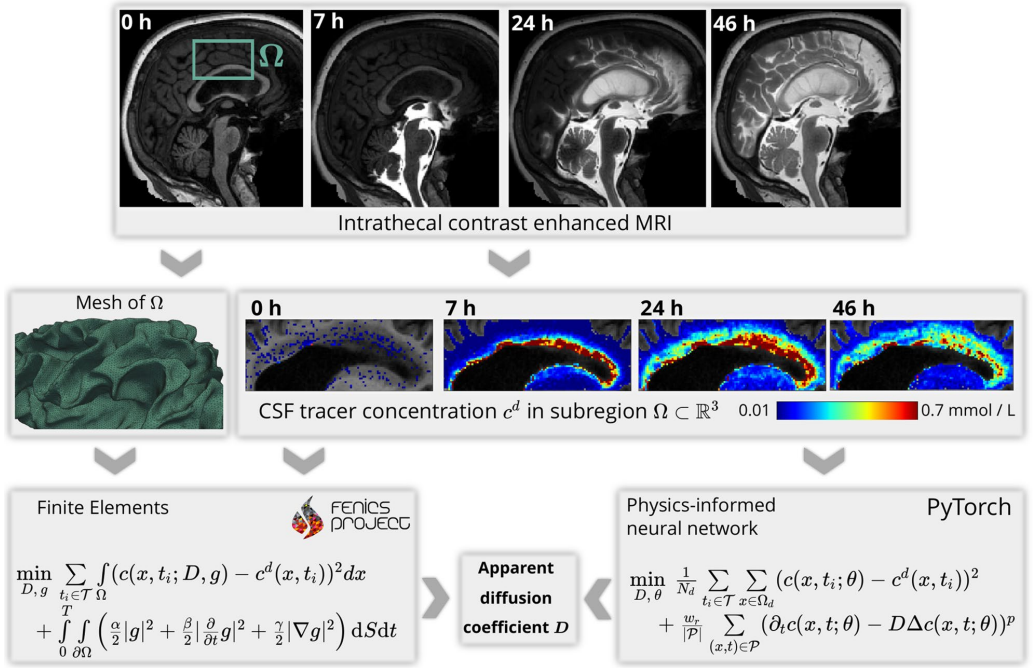

Figure 1. Flowchart illustrating our workflow from clinical images to estimated tracer diffusivity in the human brain. From the FreeSurfer[45] segmentation of a baseline MRI at $t = 0$, we define and mesh a subregion Ω of the white matter. Intrathecal contrast enhanced MRI at later times $t = 7,\ 24,\ 46$ h are used to estimate the concentration of the tracer in the subregion. We then use both a finite element based approach and physics-informed neural networks to determine the scalar diffusion coefficient that describes best the concentration dynamics in Ω.

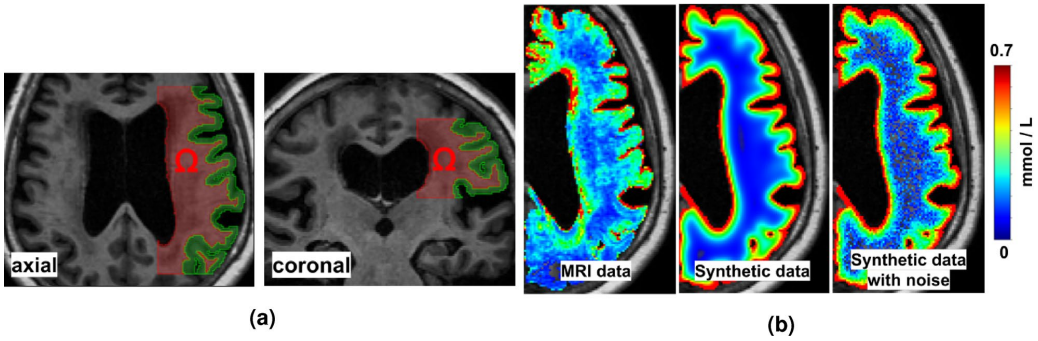

Figure 2. Geometries and data considered in this work. (**a**) Axial and coronal slices through the subregion Ω of the white matter we consider in this work. The green region depicts the gray matter and is drawn to illustrate the geometrical complexity of the grey matter. (**b**) Axial view of the tracer concentration after 24 h in the right hemisphere for the three data sets under consideration. Note how the tracer enters the brain from CSF spaces (black).

three datasets considered in this work, i.e., MRI data, synthetic data with and without noise. In all cases, we use data at $\mathcal{T} = \{0, 7, 24, 46\}$ h (after tracer injection at $t = 0$).

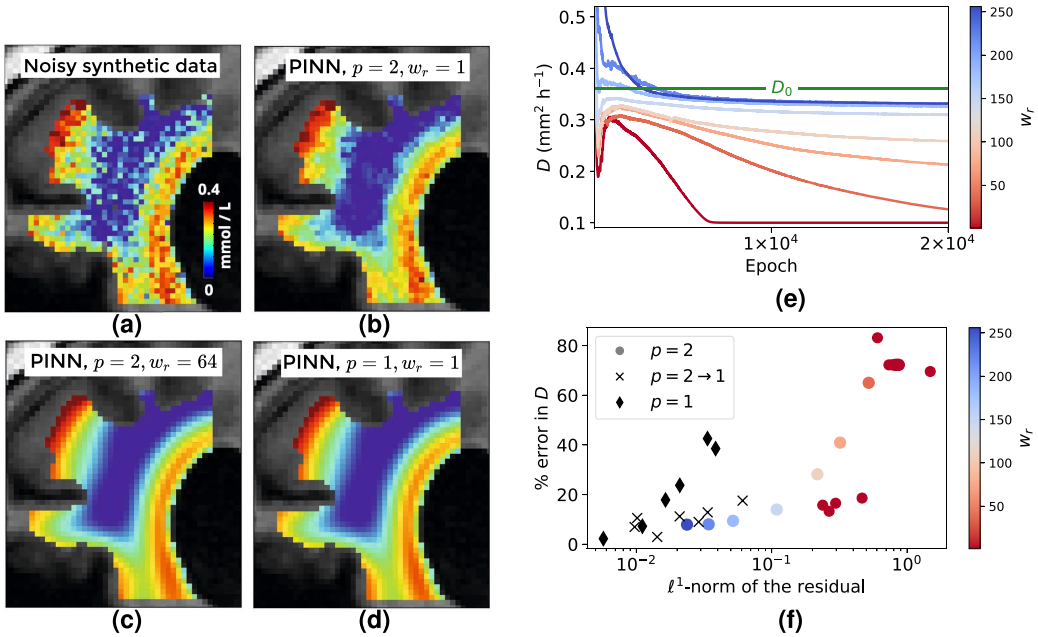

Figure 3. Influence of PINN hyperparameters on the diffusion coefficient estimated from noisy synthetic data. (**a**) Coronal slice of synthetic data with noise after 46h, compared to predictions $c(x, t = 46\,\text{h}, \theta_{\text{opt}})$ of trained PINN models with different hyperparameters in the loss function (4). The overfitting seen in the PINN with $p = 2, w_r = 1$ (**b**) can be prevented by using either increased PDE weight w_r (**c**) or the ℓ^1-norm for the PDE loss (**d**). (**e**) The diffusion coefficient recovered by the PINN trained on noisy synthetic data converges to D_{min} for PDE weight $w_r \leq 2$ in the loss function (4). (**f**) Relative error in recovered D from noisy synthetic data as a function of the residual after training for the results presented in (**e**) and Table 1. Color encodes the PDE weight $1 \leq w_r \leq 256$ for the results with $p = 2$ (dotted). Black markers indicate results with either switching $p = 2 \to 1$ during training or $p = 1$. Different hyperparameter settings in the PINN loss (4) yield models which fulfill the PDE to different accuracy, and low values for the residual coincide with more accurate recovery of the diffusion coefficient.

Results

Synthetic data. We first validate the implementation of both approaches by recovering the known diffusion coefficient D_0 from synthetic data without noise. We find that both approaches can be tuned to recover the diffusion coefficient to within a few percent accuracy from three images. Further details can be found in Supplementary Section S4 online.

Synthetic data with noise. We next discuss how to address challenges that arise for our PINN approach when trained on noisy data as specified by Supplementary Equation (S2). We find (see Supplementary Table S2 online for the details) that smaller batch sizes of $\sim 10^4$ points per loss term result in more accurate recovery of the diffusion coefficient (for fixed number of epochs). We hence divide data and PDE points into 20 batches with 1.5×10^4 and 5×10^4 samples per batch, respectively, for the following results. In all the results with synthetic data reported in this work, we trained the PINN for 20,000 epochs.

In Fig. 3a,b we compare the data to output of the PINN after training with the ADAM optimizer[48] and exponential learning rate decay from 10^{-3} to 10^{-4} for 2×10^4 epochs. In detail, after training we use the PINN as a forward surrogate model with the optimized weights and biases θ_{opt} to compute the output $c(x, t; \theta_{\text{opt}})$ at time t and voxel coordinates x.

The figures indicate that the network is overfitting the noise that was added to the synthetic data. This in turn leads to the diffusion coefficient converging to the lower bound $D_{\text{min}} = 0.1\,\text{mm}^2\,\text{h}^{-1}$ during optimization as shown in Fig. 3e. Here we discuss two remedies: (i) increasing the regularizing effect of the PDE loss via increasing the PDE weight w_r and (ii) varying the norm in the PDE loss. We observe from Fig. 3e that for $w_r \gtrsim 64$ the recovered D converges towards the true value to within $\approx 10\,\%$ error. It can also be seen that increasing the weight further does not significantly increase the accuracy. Figure 3b,c show the predicted solution after 46 h of the trained PINN. It can be seen that the overfitting occurring for $w_r = 1$ is prevented by choosing a $w_r \geq 64$. These results are in line with the frequent observation that the weights of the different loss terms in PINNs are

Parameterization	p	lr			
		10^{-3}	$10^{-3} \rightarrow 10^{-4}$	10^{-4}	$10^{-4} \rightarrow 10^{-5}$
$D = \delta$	1	×	×	18 (1.6e−02)	43 (3.4e−02)
	$2 \rightarrow 1$	×	7 (9.7e−03)	3 (1.4e−02)	13 (3.4e−02)
	2	70 (1.5e+00)	83 (6.1e−01)	16 (2.4e−01)	17 (3.0e−01)
$D = D(\delta)$	1	7 (1.1e−02)	2 (5.7e−03)	24 (2.1e−02)	39 (3.9e−02)
	$2 \rightarrow 1$	11 (2.1e−02)	11 (1.0e−02)	9 (2.9e−02)	18 (6.1e−02)
	2	72 (7.3e−01)	72 (7.7e−01)	13 (2.7e−01)	19 (4.7e−01)

Table 1. Rel. error $|D - D_0|/D_0$ in % in the diffusion coefficient and PDE residual norm after training (in brackets) for different optimization strategies averaged over 4 trainings on synthetic data with noise. It can be seen that the accuracy correlates with the PDE residual after training, i.e. the lower the PDE residual, the more accurate the recovered diffusion coefficient. This relation is further illustrated in Fig. 3f. Failure of the algorithm is indicated by the symbol "×".

critical hyperparameters. Since we assume that the data is governed by a diffusion equation (with unknown diffusion coefficient), we want the PDE residual to become small. As demonstrated above, this can be achieved by increasing the PDE weight. The correlation between a large weight, a low PDE residual and a more accurate recovery of the diffusion coefficient is visualized in Fig. 3f.

Figure 3f also demonstrates the effectiveness the strategy (ii) to successfully lower the PDE residual, which is based on using the ℓ^1-norm for the PDE loss. Using this norm makes the cost function less sensitive to outliers in the data where the observed tracer distribution c^d deviates from the diffusion model (1).

Exemplarily, we demonstrate the effectiveness of this approach in Fig. 3d. There, we plot the PINN prediction after training with $p = 1$. It can be seen that the prediction is visually identical to the prediction obtained with $p = 2$ and $w_r = 64$ (The relative difference between the predictions in Fig. 3c,d is about 2 %).

The results in Fig. 3f are obtained in a systematic study with fixed $w_r = 1$. In detail, we test the combinations of the following hyperparameters:

- Parameterizations $D(\delta)$ (10) vs. $D = \delta$ (11) of the diffusion coefficient in terms of a trainable parameter δ, c.f. section "Parameterization of the diffusion coefficient"
- $p = 1$, switching $p = 2 \rightarrow 1$ after half the epochs, $p = 2$
- fixed learning rate 10^{-3}, exponential learning rate decay $10^{-3} \rightarrow 10^{-4}$, fixed learning rate 10^{-4} and exponential learning rate decay $10^{-4} \rightarrow 10^{-5}$.

Table 1 reports the relative error in the recovered diffusion coefficient after 2×10^4 epochs of training with ADAM and the minibatch sampling described in Supplementary Algorithm 1 online. From the table it can be observed that for $D = \delta$ and $p = 1$ instabilities occur with the default learning rate 10^{-3} and, due to exploding gradients, the algorithm fails. This problem does not occur when using the parameterization $D = D(\delta)$ (10). It can further be observed that both parameterizations can be fine tuned to achieve errors $\lesssim 10\%$ in the recovered D. However, the table shows that it is *a priori* not possible to assess which hyperparameter performs best since, for example, settings that fail for the parameterization $D = \delta$ (11) work well with $D(\delta)$ (10).

We hence investigate the effect of the different hyperparameters on the trained PINN and compute the ℓ^1 -norm of the residual after training defined as

$$\frac{1}{|\mathcal{P}_\tau|} \sum_{(x,t)\in\mathcal{P}_\tau} |\partial_t c(x,t;\theta) - D\Delta c(x,t;\theta)|. \tag{2}$$

Here, $\mathcal{P}_\tau = \tau \times \Omega_p$, where $\tau = \{0, \ldots, T\}$ are 200 linearly spaced time points between first and final image at $T = 46$h and Ω_r denotes the set of center coordinates of all the voxels inside the PDE domain. Note that we evaluate (2) with the recovered diffusion coefficient, not with the true D_0. Table 1 also reports this norm for the different hyperparameter settings. It can be seen that different hyperparameters lead to different norms of the PDE residual. Table 1 reveals that low values of the residual correspond to more accurate recovery of the diffusion coefficient. These results are plotted together with the results from Fig. 3e in Fig. 3f where it can be seen that low PDE residual after training correlates with more accurate recovery of the diffusion coefficient. This underlines our observation that it is important in our setting to train the PINN such that the norm of the PDE residual is small.

Finally, for the FEM approach, Supplementary Table S4 online tabulates the relative error in the recovered diffusion coefficient for solving (7) with regularization parameters spanning several orders of magnitude. Similar to the PINN results, the parameterization $D = D(\delta)$ (10) can avoid numerical instabilities. As with the PINN approach, the FEM approach yield estimates of the diffusion coefficient accurate to $\lesssim 10\%$ for proper choice of regularization parameters. The results are in line with the well-established observation that a sophisticated decrease of the noise level and regularization parameters ensures convergence towards a solution[49].

MRI data. We proceed to estimate the apparent diffusion coefficient governing the spread of tracer as seen in MRI images. It is worth emphasizing here that our modeling assumption of tracer transport via diffusion with

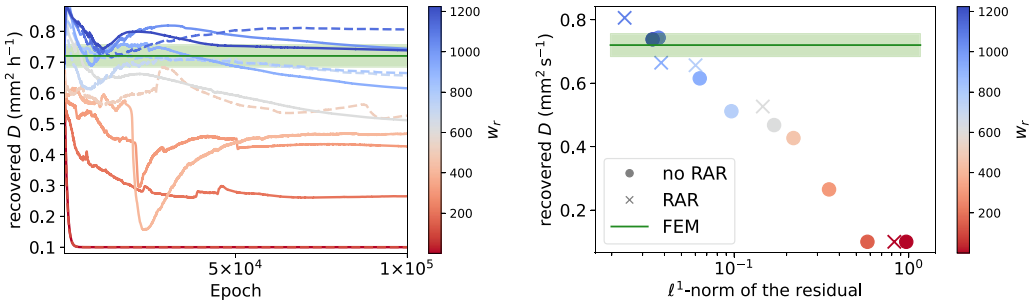

Figure 4. Influence of PINN hyperparameters on the diffusion coefficient estimated from clinical data. (**a**) Diffusion coefficient during training for different PDE weights w_r and exponentially decaying learning rate from 10^{-4} to 10^{-5}. Dashed lines indicate result with residual based adaptive refinement (RAR). (**b**) Estimated diffusion coefficient with $p = 2$ for different PDE weights w_r as a function of the ℓ^1-norm of the residual after training. The values for FEM and the green horizontal bars indicating an error estimate are taken from Valnes et al.[28].

a constant diffusion coefficient $D \in \mathbb{R}$ is a simplification, and that we can not expect perfect agreement between model predictions and the MRI data. Furthermore, closer inspection of the tracer distribution on the boundary in Fig. 2b reveals that, unlike in the synthetic data, the concentration varies along the boundary in the MRI measurements. Based on these two considerations it is to be expected that challenges with the PINN approach arise that were not present in the previous, synthetic testcases. However, our previous observation that smaller PDE residual correlates with more accurate recovery of the diffusion coefficient serves as a guiding principle on how to formulate and minimize the PINN loss function such that the PDE residual becomes small.

Based on the observation that the parameterization $D = D(\delta)$ avoids instabilities during the optimization, we only use this setting in this subsection. The white matter domain Ω is the same as in the previous section, and we again divide both data and PDE loss into 20 minibatches. We train for 10^5 epochs using the ADAM optimizer with exponentially decaying learning rate 10^{-4} to 10^{-5}. The reason we have to train the PINN for more epochs on MRI data compared to the synthetic test case (where we used 20,000 epochs) is the need for using lower learning rate together with learning rate decay to avoid convergence into a bad local minimum (where typically $c(x, t; \theta) = \text{const}$ and $D \to 0$).

We first test for $p = 2$ with PDE weight $w_r \in \{1, 32, 64, 128, 256, 512, 1024\}$ and display the results in Fig. 4a. It can be seen that, similar to the noisy synthetic data, the diffusion coefficient converges to the lower bound for low PDE weights. For these settings, we plot the residual norm (2) of the trained networks in Fig. 4b. It can be seen that increased PDE weight leads to lower residual after training, and in turn to an estimate for D which becomes closer to FEM.

Further, in Fig. 5a we also plot the ℓ^1-norm of the residual after training as a function of time $t \in [0, T]$, defined as

$$r(t) = \frac{1}{|\Omega_r|} \sum_{x \in \Omega_r} |\partial_t c(x, t; \theta) - D \Delta c(x, t; \theta)|. \tag{3}$$

The continuous blue lines in Fig. 5a exemplarily show $r(t)$ for some PDE weights. It can be seen that higher PDE weights lead to lower residuals. However, for $w_r = 256$ the PDE residual is significantly higher at the times where data is available than in between. We did not observe this behavior in the synthetic testcase. Since we want the modeling assumption (1) to be fulfilled equally in $\Omega \times [0, T]$, we use residual based adaptive refinement (RAR)[50]. Using the RAR procedure, we add 10^5 space-time points to the set $\mathcal{P}$ of PDE points after 1×10^4, $2 \times 10^4, \ldots, 9 \times 10^4$ epochs. Details on our implementation of RAR and an exemplary loss plot during PINN training are given in Supplementary Section S5.2 online. The effectiveness of RAR to reduce this overfitting is indicated by the dashed blue lines in Fig. 5a.

Next, we test for $p = 1$ with an exponentially decaying learning rate from 10^{-3} to 10^{-4} as well as 10^{-4} to 10^{-5}. With this setting, the PINNs approach yields an estimate $D = 0.75\,\text{mm}^2\,\text{h}^{-1}$ which is close to the FEM solution[28] $D = 0.72\,\text{mm}^2\,\text{h}^{-1}$. However, a closer inspecting of the PINN prediction at 22 and 24 (where data is available) shown in Fig. 6a reveals that the PINN is overfitting the data. This is further illustrated by the continuous red line in Fig. 5 where it can be seen that the PDE residual is one order of magnitude higher at the times where data is available. The dashed red line in Fig. 5 and slices of the predicted $c(x, t; \theta_{\text{opt}})$ shown in Fig. 6a show that this behavior can be prevented by using RAR. The FEM approach also shown in Fig. 6a resolves the boundary data in more detail than the PINN solution obtained with RAR. This can be explained by the fact that the boundary condition g explicitly enters the FEM approach as a control variable.

Since the RAR procedure increases the number of PDE points, the computing time increases (by about 25 % in our setting). We hence test a modification of the RAR procedure. Instead of only adding points, we also remove the points from $\mathcal{P}$ where the PDE residual is already low. We here call this procedure residual based

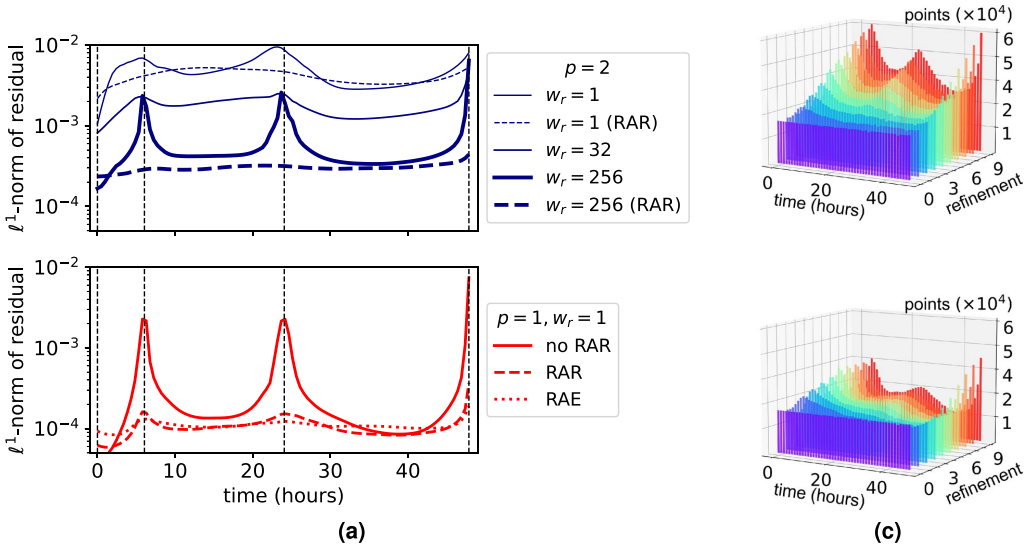

Figure 5. Adaptive training point refinement is needed to fulfill the PDE in all timepoints. (**a**) Average PDE residual in Ω_P over time for different optimization schemes. Vertical lines (dashed) indicate the times where data is available. In all cases, the learning rate decays exponentially from 10^{-3} to 10^{-4}. (**b**,**c**) Distribution of PDE points during training with RAR (**b**) and RAE (**c**). Starting from a uniform distribution of points (in time), more points are added at 7, 24 and 46 h where data is available.

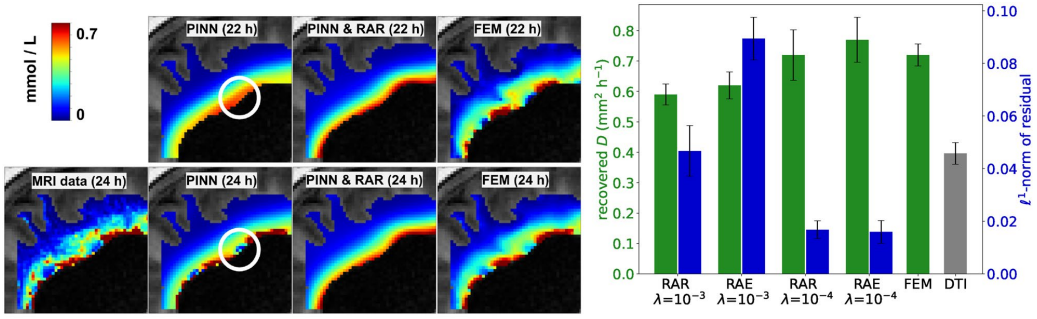

Figure 6. Adaptive refinement yields PINN solutions that are consistent with a diffusion model. (**a**) Upper row: Output $c(x, t = 22\,\text{h}, \theta_{\text{opt}})$ of PINNs models trained with $p = 1$ and $p = 1$ & RAR and FEM solution for $(\alpha, \beta, \gamma) = (10^{-6}, 0.1, 0.01)$. Lower row: Zoom into a sagittal slice of data at 24h compared PINN and FEM solutions. The PINN prediction after training without RAR overfits the data. Compare also to Fig. 5. (**b**) Green: PINN estimates for the diffusion coefficient with RAR or RAE and different initial learning rates ($p = 1$ in all cases). Blue: ℓ^1-norm of the residual after training. It can be seen that lower learning rate leads to a lower residual norm and an estimate for the diffusion coefficient closer to the FEM approach.

adaptive exchange (RAE) and give the details in Supplementary Section S5.2 online. We note that similar refinement techniques have recently also been proposed and studied extensively in[51] and[52].

The dotted red line in Fig. 5 demonstrates that in our setting both methods yield similarly low residuals $r(t)$ without overfitting the data. Since in RAE the number of PDE points stays the same during training, the computing time is the same as without RAR. In Fig. 5b it can be seen how both RAR and RAE add more PDE points around the timepoints where data is available.

We estimate the apparent diffusion coefficient D by averaging over 5 trainings with either RAR or RAE and learning rate decay from 10^{-3} to 10^{-4} or 10^{-4} to 10^{-5}. The results are displayed in Fig. 6b together with the ℓ^1 -norm (2) after training. It can be seen that for the same learning rate, both RAR and RAE yield similar results.

A lower learning rate, however, leads to lower PDE residual and an estimated diffusion coefficient which is closer to the value 0.72 $mm^2\,h^{-1}$ from Valnes et al.[28].

Testing different patients. In Valnes et al.[28], the same methodology was applied to two more patients, named 'REF' and 'NPH2'. We here test how well the optimal hyperparameter settings found in section "MRI data" generalize to these patients. A similar subregion of the white matter is used but the voxels on the boundary of the domain were removed.

A PINN is trained with the following hyperparameters from section "MRI data" that yielded the lowest PDE residual after training: The number of minibatches is set to 20, training for 10^5 epochs with ADAM and exponential learning rate decay from 10^{-4} to 10^{-5}, and $p = 1$ with RAR at 1×10^4, $2 \times 10^4, \ldots, 9 \times 10^4$ epochs. The network architecture remains the same. For patient 'NPH2' we find $D = 0.48\ mm^2\,h^{-1}$ while the FEM approach[28] yields $D = 0.50\ mm^2\,h^{-1}$. We find $D = 0.41\ mm^2\,h^{-1}$ for patient 'REF' while the FEM approach[28] yields $D = 0.50\ mm^2\,h^{-1}$.

Discussion

We have tested both PINNs and FEM for assessing the apparent diffusion coefficient in a geometrically complex domain, a subregion of the white matter of the human brain, based on a few snapshots of T1-weighted contrast enhanced MR images over the course of 2 days. Both methodologies yield similar estimates when properly set up, that is; we find that the ADC is in the range (0.6–0.7) $mm^2\,h^{-1}$, depending on the method, whereas the DTI estimate is 0.4 $mm^2\,h^{-1}$. As such the conclusion is similar to that of Valnes et al.[28]. With a proper hyperparameter set-up, PINNs are as accurate as FEM and, given our implementation with GPU acceleration, roughly twice as fast as our current FEM implementation on MRI data as shown in Supplementary Section S4.1 online.

However, choosing such a set-up, i.e., hyperparameter setting, loss function formulation and training procedure, is still a priory not known and challenging. An automated way to find a suitable setting is needed. To this end automated approaches such as AutoML[53] or Meta learning[54], could be applied in the future. Moreover, theoretical guarantees are required, especially in sensitive human-health related applications.

Our results are in line with the frequent observation that the PDE loss weight is an important hyperparameter. Several works have put forth methodologies to choose the weights adaptively during training[8–11], but in practice they have also been chosen via trial-and-error[43,55,56]. However, in settings with noisy data, it can not be expected that both data loss and PDE loss become zero. The ratio between PDE loss weight and data loss weight reflects to some degree the amount of trust one has in the data and the physical modeling assumptions, i.e., the PDE. In this work, we have made the modeling assumption that the data is governed by a diffusion equation, and hence require the PDE to be fulfilled. This provides a criterion for choosing a Pareto-optimal solution if the PINN loss is considered from a multi-objective perspective[57].

From the mathematical point of view, we have sought the solution of a challenging nonlinear ill-posed inverse problem with limited and noisy data in both space and time. There can thus be more than one local minimum and the estimated solutions depend on the regularization and/or hyperparameters. Here, our main observation is that the diffusion coefficient recovered by PINNs approaches the FEM result when the hyperparameters are chosen to ensure that the PDE residual after training is sufficiently small.

In general, we think that the current problem serves as a challenging test case and is well suited for comparing PINNs and FEM based methods. Further, since the finite element approach is well-established and theoretically founded it can serve to benchmark PINNs. Our numerical results indicate that the norm of the PDE residual of the trained PINN correlates with the quality of the recovered parameter. This relates back to the finite element approach where the PDE residual is small since the PDE is explicitly solved. In our example, we have found that in particular two methodological choices help to significantly lower the PDE-residual in the PINNs approach: ℓ^1-penalization of the PDE and adaptive refinement of residual points.

From the physiological point of view, there are several ways to improve upon our modeling assumption of a diffusion equation with spatially constant, scalar diffusion coefficient. The microscopic bulk flow proposed by the glymphatic theory may, on the macroscopic scale, be mathematically modelled in the form of convection[40], dispersion[58], clearance[59].

For instance, an estimate of the local CSF velocity can be obtained by the optimal mass transport technique[60]. From an implementational point of view, such methods fit well within our current framework since the PINN formulation is comparably easy to implement and the PDE does not have to be solved explicitly.

Methods

Approvals and MRI acquisition. The approval for MRI observations was retrieved by the Regional Committee for Medical and Health Research Ethics (REK) of Health Region South-East, Norway (2015/96) and the Institutional Review Board of Oslo University Hospital (2015/1868) and the National Medicines Agency (15/04932-7). The study participants were included after written and oral informed consent. All methods were performed in accordance with the relevant guidelines and regulations. Details on MRI data acquisition and generation of synthetic data can be found in the Supplementary Section S1 online.

The PINN approach. In PINNs, our parameter identification problem can be formulated as an unconstrained non-convex optimization problem over the network parameters θ and the diffusion coefficient D as

$$\min_{\theta,D} \mathcal{J} + w_r \mathcal{L}_r, \tag{4}$$

where $w_r > 0$ is a weighting factor. We model the concentration measurements by a fully connected neural network $c(x, t; \theta)$ where $x \in \mathbb{R}^3$ are spatial inputs and $t \in \mathbb{R}$ is the time input. The data loss $\mathcal{J}$ is defined as

$$\mathcal{J} = \frac{1}{N_d} \sum_{t_i \in \mathcal{T}} \sum_{x \in \Omega_d} (c(x, t_i; \theta) - c^d(x, t_i))^2, \tag{5}$$

where Ω_d is a discrete finite subset of Ω, $\mathcal{T} = \{0, 7, 24, 46\}$ h, and N_d denotes the number of space-time points in $\mathcal{T} \times \Omega$ where we have observations. The PDE loss term $\mathcal{L}_r$ is defined as

$$\mathcal{L}_r = \frac{1}{|\mathcal{P}|} \sum_{(x,t) \in \mathcal{P}} |\partial_t c(x, t; \theta) - D\Delta c(x, t; \theta)|^p, \tag{6}$$

where $p \in [1, \infty)$, the set $\mathcal{P}$ consists of N_r points in $\tau \times \Omega_r, \tau \subset [0, T]$, and $\Omega_r \subset \Omega$ is a set of $N_p = |\mathcal{P}|$ coordinates $x \in \mathbb{R}^3$ that lie in the *interior* of the domain Ω. The sampling strategy to generate $\mathcal{P}$ is explained in detail in Supplementary Section S3 online. In this work we test training with both $p = 2$ and $p = 1$. It is worth noting that boundary conditions are not included (in fact, they are often not required for inverse problems[3]) in the PINN loss function (4), allowing us to sidestep making additional assumptions on the unknown boundary condition. The initial condition is taken to be the first image at $t = 0$ and simply enters via the data loss term (5). A detailed description of the network architecture and other hyperparameter settings can be found in Supplementary Section S3 online.

The finite element approach. Our parameter identification problem describes a nonlinear ill-posed inverse problem[61–63]. As a comparison baseline for the PINN approach, we build on the numerical realization of Valnes et al.[28] and define the PDE constrained optimization problem[64] as

$$\min_{D,g} \sum_{t_i \in \mathcal{T}} \int_\Omega (c(x, t_i; D, g) - c^d(x, t_i))^2 \, \mathrm{d}x + \frac{1}{2} \int_0^T \int_{\partial\Omega} \left(\alpha |g|^2 + \beta |\frac{\partial}{\partial t} g|^2 + \gamma |\nabla g|^2 \right) \mathrm{d}S\mathrm{d}t, \tag{7}$$

where, similar to[28], the second term is Tikhonov regularization with regularization parameters $\alpha, \beta, \gamma > 0$ and $c = c(x, t, D, g)$ solves (1) with boundary and initial conditions

$$c(x, t) = g(x, t) \quad \text{on } \partial\Omega \times (0, T), \tag{8}$$

$$c(x, 0) = 0 \quad \text{in } \Omega. \tag{9}$$

To determine c for given (D, g), the partial differential equation is considered in a weak variational form and discretized in time, by using a finite difference method, and in space, by using finite elements. This leads to a sequence of linear systems of equations, which needs to be solved to obtain the state c. Hence, in the finite element approach, the state, that is used to evaluate the objective function, fulfills the weak form of the partial differential equation in a discretized sense. In order to compute the derivative of the functional (7) with respect to the controls (D, g), automated differentiation techniques are applied in a similar fashion as backpropagation is applied for neural networks. A detailed description of the mathematical and implementation details can be found in Supplementary Section S3 online.

Parameterization of the diffusion coefficient. Previous findings[35,40,59,60] indicate that diffusion contributes at least to some degree to the distribution of tracers in the brain. It can thus be assumed that a vanishing diffusion coefficient is unphysical. This assumption can be incorporated into the model by parameterizing D in terms of a trainable parameter δ as

$$D(\delta) = D_{\min} + \sigma(\delta) D_{\max}, \tag{10}$$

where $\sigma(x) = (1 + \exp(-x))^{-1}$ denotes the logistic sigmoid function. In all results reported here, we initialize with $\delta = 0$ and set $D_{\min} = 0.1\ \mathrm{mm^2\ h^{-1}}$ and $D_{\max} = 1.2\ \mathrm{mm^2\ h^{-1}}$. This parameterization with a sigmoid function effectively leads to vanishing gradients $|\frac{\partial D}{\partial \delta}|$ for $|\delta| \gg 1$. In section "Synthetic data with noise" we demonstrate that this choice of parameterization can help to avoid instabilities that occur during PINN training without parameterization, i.e.

$$D = \delta. \tag{11}$$

The reason to introduce a $D_{\min} > 0$ is to avoid convergence into a bad local minimum. For the finite element approach, we did not observe convergence into a local minimum where $D = 0$, and hence used the parameterization (11).

Data availability

The datasets analyzed in the current study are available from the corresponding author upon request.

Received: 6 July 2022; Accepted: 24 August 2022
Published online: 14 September 2022

References

1. Karniadakis, G. E. *et al.* Physics-informed machine learning. *Nat. Rev. Phys.*https://doi.org/10.1038/s42254-021-00314-5 *(2021).*
2. Lagaris, I., Likas, A. & Fotiadis, D. Artificial neural networks for solving ordinary and partial differential equations. *IEEE Trans. Neural Netw.* **9**, 987–1000. https://doi.org/10.1109/72.712178 (1998).
3. Raissi, M., Perdikaris, P. & Karniadakis, G. Physics-informed neural networks: A deep learning framework for solving forward and inverse problems involving nonlinear partial differential equations. *J. Comput. Phys.* **378**, 686–707. https://doi.org/10.1016/j.jcp.2018.10.045 (2019).
4. Cuomo, S. *et al.* Scientific machine learning through physics-informed neural networks: where we are and what's next. arXiv preprint arXiv:2201.05624 (2022).
5. Dwivedi, V. & Srinivasan, B. Physics informed extreme learning machine (PIELM)—A rapid method for the numerical solution of partial differential equations. *Neurocomputing* **391**, 96–118 (2020).
6. Nabian, M. A., Gladstone, R. J. & Meidani, H. Efficient training of physics-informed neural networks via importance sampling. *Comput. Aided Civ. Infrastruct. Eng.* **36**, 962–977 (2021).
7. Jagtap, A. D., Kawaguchi, K. & Em Karniadakis, G. Locally adaptive activation functions with slope recovery for deep and physics-informed neural networks. *Proc. R. Soc. A Math. Phys. Eng. Sci.* **476**, 20200334. https://doi.org/10.1098/rspa.2020.0334 (2020).
8. Wang, S., Yu, X. & Perdikaris, P. When and why PINNs fail to train: A neural tangent kernel perspective. *J. Comput. Phys.* **449**, 110768. https://doi.org/10.1016/j.jcp.2021.110768 (2022).
9. Wang, S., Wang, H. & Perdikaris, P. On the eigenvector bias of Fourier feature networks: From regression to solving multi-scale PDEs with physics-informed neural networks. arXiv:2012.10047 [cs, stat] (2020).
10. van der Meer, R., Oosterlee, C. & Borovykh, A. Optimally weighted loss functions for solving PDEs with neural networks. arXiv:2002.06269 [cs, math] (2021).
11. Maddu, S., Sturm, D., Müller, C. L. & Sbalzarini, I. F. Inverse Dirichlet weighting enables reliable training of physics informed neural networks. *Mach. Learn. Sci. Technol.* **3**, 015026. https://doi.org/10.1088/2632-2153/ac3712 (2022) (**Publisher: IOP Publishing**).
12. Leake, C. & Mortari, D. Deep theory of functional connections: A new method for estimating the solutions of partial differential equations. *Mach. Learn. Knowl. Extract.* **2**, 37–55 (2020).
13. Schiassi, E. *et al.* Extreme theory of functional connections: A fast physics-informed neural network method for solving ordinary and partial differential equations. *Neurocomputing* **457**, 334–356 (2021).
14. Jin, X., Cai, S., Li, H. & Karniadakis, G. E. NSFnets (Navier–Stokes flow nets): Physics-informed neural networks for the incompressible Navier–Stokes equations. *J. Comput. Phys.* **426**, 109951. https://doi.org/10.1016/j.jcp.2020.109951 (2021).
15. Cai, S., Wang, Z., Wang, S., Perdikaris, P. & Karniadakis, G. E. Physics-informed neural networks for heat transfer problems. *J. Heat Transf.* **143**, 060801. https://doi.org/10.1115/1.4050542 (2021).
16. Schiassi, E., De Florio, M., D'ambrosio, A., Mortari, D. & Furfaro, R. Physics-informed neural networks and functional interpolation for data-driven parameters discovery of epidemiological compartmental models. *Mathematics* **9**, 2069 (2021).
17. De Florio, M., Schiassi, E. & Furfaro, R. Physics-informed neural networks and functional interpolation for stiff chemical kinetics. *Chaos* **32**, 063107 (2022).
18. Psichogios, D. C. & Ungar, L. H. A hybrid neural network-first principles approach to process modeling. *AIChE J.* **38**, 1499–1511 (1992).
19. Rudy, S. H., Brunton, S. L., Proctor, J. L. & Kutz, J. N. Data-driven discovery of partial differential equations. *Sci. Adv.* **3**, e1602614. https://doi.org/10.1126/sciadv.1602614 (2017).
20. Peng, G. C. Y. *et al.* Multiscale modeling meets machine learning: What can we learn?. *Arch. Comput. Methods Eng.* **28**, 1017–1037. https://doi.org/10.1007/s11831-020-09405-5 (2021).
21. Cai, S., Wang, Z., Chryssostomidis, C. & Karniadakis, G. E. Heat transfer prediction with unknown thermal boundary conditions using physics-informed neural networks. In *Computational Fluid Dynamics; Micro and Nano Fluid Dynamics*, vol. 3, V003T05A054. https://doi.org/10.1115/FEDSM2020-20159 (American Society of Mechanical Engineers, Virtual, Online, 2020).
22. Jagtap, A. D., Mao, Z., Adams, N. & Karniadakis, G. E. Physics-informed neural networks for inverse problems in supersonic flows. arXiv:2202.11821 [cs, math] (2022).
23. Reyes, B., Howard, A. A., Perdikaris, P. & Tartakovsky, A. M. Learning unknown physics of non-Newtonian fluids. arXiv:2009.01658 [physics] (2020).
24. Arzani, A., Wang, J.-X. & D'Souza, R. M. Uncovering near-wall blood flow from sparse data with physics-informed neural networks. *Phys. Fluids* **33**, 071905. https://doi.org/10.1063/5.0055600 (2021) (**Publisher: American Institute of Physics**).
25. Cai, S. *et al.* Flow over an espresso cup: Inferring 3-D velocity and pressure fields from tomographic background oriented Schlieren via physics-informed neural networks. *J. Fluid Mech.* **915**, A102. https://doi.org/10.1017/jfm.2021.135 (2021).
26. Kissas, G. *et al.* Machine learning in cardiovascular flows modeling: Predicting arterial blood pressure from non-invasive 4D flow MRI data using physics-informed neural networks. *Comput. Methods Appl. Mech. Eng.* **358**, 112623. https://doi.org/10.1016/j.cma.2019.112623 (2020).
27. Cai, S., Mao, Z., Wang, Z., Yin, M. & Karniadakis, G. E. Physics-informed neural networks (PINNs) for fluid mechanics: A review. arXiv:2105.09506 [physics] (2021).
28. Valnes, L. M. *et al.* Apparent diffusion coefficient estimates based on 24 hours tracer movement support glymphatic transport in human cerebral cortex. *Sci. Rep.* **10**, 9176. https://doi.org/10.1038/s41598-020-66042-5 (2020) (**Number: 1 Publisher: Nature Publishing Group**).
29. Mardal, K.-A., Rognes, M. E., Thompson, T. B. & Valnes, L. M. Mathematical modeling of the human brain: From magnetic resonance images to finite element simulation (2022).
30. Ray, L. A., Pike, M., Simon, M., Iliff, J. J. & Heys, J. J. Quantitative analysis of macroscopic solute transport in the murine brain. *Fluids Barriers CNS* **18**, 55. https://doi.org/10.1186/s12987-021-00290-z (2021).
31. Iliff, J. J. *et al.* A paravascular pathway facilitates CSF flow through the brain parenchyma and the clearance of interstitial solutes, including amyloid beta. *Sci. Transl. Med.* **4**, 147ra111-147ra111. https://doi.org/10.1126/scitranslmed.3003748 (2012) (**Publisher: American Association for the Advancement of Science Section: Research Article**).
32. Nedergaard, M. & Goldman, S. A. Glymphatic failure as a final common pathway to dementia. *Science (New York, N.Y.)* **370**, 50–56. https://doi.org/10.1126/science.abb8739 (2020).
33. Mestre, H. *et al.* Flow of cerebrospinal fluid is driven by arterial pulsations and is reduced in hypertension. *Nat. Commun.* **9**, 4878. https://doi.org/10.1038/s41467-018-07318-3 (2018).
34. Ringstad, G. *et al.* Brain-wide glymphatic enhancement and clearance in humans assessed with MRI. *JCI Insight* **3**, e121537. https://doi.org/10.1172/jci.insight.121537 (2018).
35. Holter, K. E. *et al.* Interstitial solute transport in 3D reconstructed neuropil occurs by diffusion rather than bulk flow. *Proc. Natl. Acad. Sci.* **114**, 9894–9899. https://doi.org/10.1073/pnas.1706942114 (2017) (**Publisher: National Academy of Sciences Section: Biological Sciences**).
36. Hladky, S. B. & Barrand, M. A. The glymphatic hypothesis: The theory and the evidence. *Fluids Barriers CNS* **19**, 9. https://doi.org/10.1186/s12987-021-00282-z (2022).
37. Kedarasetti, R. T., Drew, P. J. & Costanzo, F. Arterial pulsations drive oscillatory flow of CSF but not directional pumping. *Sci. Rep.* **10**, 10102. https://doi.org/10.1038/s41598-020-66887-w (2020) (**Number: 1 Publisher: Nature Publishing Group**).

38. Ladrón-de Guevara, A., Shang, J. K., Nedergaard, M. & Kelley, D. H. Perivascular pumping in the mouse brain: Improved boundary conditions reconcile theory, simulation, and experiment. *J. Theor. Biol.* **542**, 111103 (2022).
39. Smith, A. J. & Verkman, A. S. Going against the flow: Interstitial solute transport in brain is diffusive and aquaporin-4 independent. *J. Physiol.* **597**, 4421–4424. https://doi.org/10.1113/JP277636 (2019).
40. Ray, L., Iliff, J. J. & Heys, J. J. Analysis of convective and diffusive transport in the brain interstitium. *Fluids Barriers CNS* **16**, 6. https://doi.org/10.1186/s12987-019-0126-9 (2019).
41. Fathi, M. F. *et al.* Super-resolution and denoising of 4d-flow MRI using physics-informed deep neural nets. *Comput. Methods Programs Biomed.* **197**, 105729 (2020).
42. Borges, P. *et al.* Physics-informed brain MRI segmentation. In *International Workshop on Simulation and Synthesis in Medical Imaging*, 100–109 (Springer, 2019).
43. van Herten, R. L., Chiribiri, A., Breeuwer, M., Veta, M. & Scannell, C. M. Physics-informed neural networks for myocardial perfusion MRI quantification. *Med. Image Anal.* **78**, 102399 (2022).
44. Sarabian, M., Babaee, H. & Laksari, K. Physics-informed neural networks for brain hemodynamic predictions using medical imaging. *IEEE Trans. Med. Imaging* (2022).
45. Fischl, B. FreeSurfer. *NeuroImage* **62**, 774–781. https://doi.org/10.1016/j.neuroimage.2012.01.021 (2012).
46. Syková, E. & Nicholson, C. Diffusion in brain extracellular space. *Physiol. Rev.* **88**, 1277–1340. https://doi.org/10.1152/physrev.00027.2007 (2008).
47. Alexander, A. L., Lee, J. E., Lazar, M. & Field, A. S. Diffusion tensor imaging of the brain. *Neurotherapeutics* **4**, 316–329. https://doi.org/10.1016/j.nurt.2007.05.011 (2007).
48. Kingma, D. P. & Ba, J. Adam: A method for stochastic optimization. arXiv preprint arXiv:1412.6980 (2014).
49. Kaltenbacher, B., Neubauer, A. & Scherzer, O. *Iterative Regularization Methods for Nonlinear Ill-Posed Problems* (De Gruyter, 2008).
50. Lu, L., Meng, X., Mao, Z. & Karniadakis, G. E. DeepXDE: A deep learning library for solving differential equations. *SIAM Rev.* **63**, 208–228. https://doi.org/10.1137/19M1274067 (2021) (**Publisher: Society for Industrial and Applied Mathematics**).
51. Daw, A., Bu, J., Wang, S., Perdikaris, P. & Karpatne, A. Rethinking the importance of sampling in physics-informed neural networks. arXiv preprint arXiv:2207.02338 (2022).
52. Wu, C., Zhu, M., Tan, Q., Kartha, Y. & Lu, L. A comprehensive study of non-adaptive and residual-based adaptive sampling for physics-informed neural networks. arXiv preprint arXiv:2207.10289 (2022).
53. He, X., Zhao, K. & Chu, X. Automl: A survey of the state-of-the-art. *Knowl. Based Syst.* **212**, 106622 (2021).
54. Psaros, A. F., Kawaguchi, K. & Karniadakis, G. E. Meta-learning PINN loss functions. *J. Comput. Phys.* **458**, 111121 (2022).
55. Yin, M., Zheng, X., Humphrey, J. D. & Karniadakis, G. E. Non-invasive inference of thrombus material properties with physics-informed neural networks. *Comput. Methods Appl. Mech. Eng.* **375**, 113603. https://doi.org/10.1016/j.cma.2020.113603 (2021).
56. Yazdani, A., Lu, L., Raissi, M. & Karniadakis, G. E. Systems biology informed deep learning for inferring parameters and hidden dynamics. *PLoS Comput. Biol.* **16**, e1007575. https://doi.org/10.1371/journal.pcbi.1007575 (2020).
57. Rohrhofer, F. M., Posch, S. & Geiger, B. C. On the pareto front of physics-informed neural networks. arXiv preprint arXiv:2105.00862 (2021).
58. Asgari, M., de Zélicourt, D. & Kurtcuoglu, V. Glymphatic solute transport does not require bulk flow. *Sci. Rep.* **6**, 38635. https://doi.org/10.1038/srep38635 (2016).
59. Croci, M., Vinje, V. & Rognes, M. E. Uncertainty quantification of parenchymal tracer distribution using random diffusion and convective velocity fields. *Fluids Barriers CNS* **16**, 32. https://doi.org/10.1186/s12987-019-0152-7 (2019).
60. Koundal, S. *et al.* Optimal mass transport with lagrangian workflow reveals advective and diffusion driven solute transport in the glymphatic system. *Sci. Rep.* **10**, 1990. https://doi.org/10.1038/s41598-020-59045-9 (2020).
61. Ito, K. & Kunisch, K. On the choice of the regularization parameter in nonlinear inverse problems. *SIAM J. Optim.* **2**, 376–404. https://doi.org/10.1137/0802019 (1992).
62. Holler, G., Kunisch, K. & Barnard, R. C. A bilevel approach for parameter learning in inverse problems. *Inverse Probl.* **34**, 115012. https://doi.org/10.1088/1361-6420/aade77 (2018).
63. Kaltenbacher, B., Kirchner, A. & Vexler, B. Adaptive discretizations for the choice of a Tikhonov regularization parameter in nonlinear inverse problems. *Inverse Probl.* **27**, 125008. https://doi.org/10.1088/0266-5611/27/12/125008 (2011).
64. Hinze, M., Pinnau, R., Ulbrich, M. & Ulbrich, S. *Optimization with PDE Constraints* Vol. 23 (Springer Science & Business Media, 2008).

Acknowledgements

We would like to thank Lars Magnus Valnes for insightful discussions and providing scripts for preprocessing the MRI data and meshing. We would like to thank George Karniadakis, Xuhui Meng, Khemraj Shukla and Shengze Cai from Brown University for helpful discussions about PINNs in the early stages of this work. We note and thankfully acknowledge G. Karniadakis' suggestion to switch to ℓ^1 loss during the optimization. The finite element computations were performed on resources provided by Sigma2 - the National Infrastructure for High Performance Computing and Data Storage in Norway. The PINN results presented in this paper have been computed on the Experimental Infrastructure for Exploration of Exascale Computing (eX3), which is financially supported by the Research Council of Norway under contract 270053.

Author contributions

B.Z., J.H., M.K, K.A.M. conceived the experiments. P.K.E. and G.R. acquired the data. B.Z. implemented the simulators. B.Z. conducted the experiments and made the figures. All authors discussed and analyzed the results. B.Z., J.H., M.K., K.A.M. wrote the draft. All authors revised the manuscript and approved the final manuscript.

Funding

This study was funded by Norges Forskningsråd (Research Council of Norway) (Nos. 300305, 303362).

Competing interests

The authors declare no competing interests.

Additional information

Supplementary Information The online version contains supplementary material available at https://doi.org/10.1038/s41598-022-19157-w.

Correspondence and requests for materials should be addressed to K.-A.M.

Supplementary information for 'Investigating molecular transport in the human brain from MRI with physics-informed neural networks'

Bastian Zapf[1], **Johannes Haubner**[2], **Miroslav Kuchta**[2], **Geir Ringstad**[3,4], **Per Kristian Eide**[5,6], **and Kent-Andre Mardal**[1,2,*]

[1]University of Oslo, Faculty of Mathematics and Natural Sciences, Oslo, 0851, Norway
[2]Simula Research Laboratory, Department of Numerical Analysis and Scientific Computing, Oslo, 0164, Norway
[3]Oslo University Hospital, Department of Radiology, Oslo, 0372, Norway
[4]Sorlandet Hospital, Department of Geriatrics and Internal medicine, Arendal, 4838, Norway
[5]Oslo University Hospital, Department of Neurosurgery, Oslo, 0372, Norway
[6]University of Oslo, Institute of Clinical Medicine, Oslo, 0372, Norway
[*]kent-and@simula.no

S1 Data Generation

S1.1 MRI Data

The data under consideration in this study is based on MRI scans taken of a patient who was imaged at Oslo University Hospital in Oslo, Norway. The patient was diagnosed with normal pressure hydrocephalus and is referred to as "NPH1" in[1].

The imaging protocol starts with the acquisition of a baseline MRI before 0.5 mL of a contrast agent (1 mmol/mL gadobutrol) is injected into the CSF at the spinal canal (intrathecal injection). The pulsating movement of CSF transports the tracer towards the head where it enters the brain. The contrast agent alters the magnetic properties of tissue and fluid, and in subsequently taken MRI, enriched brain regions display changes in MR signal relative to the baseline MRI. From the change in signal we estimate the concentration of tracer per voxel at timepoints 0, 7, 24 and 46 hours after injection. Further details on the MRI acquisition and tracer concentration estimation can be found in[1].

We next use FreeSurfer[2] to segment the baseline image into anatomical regions and obtain binary masks for white and gray matter. The human brain has many folds and represents a highly complex geometry. To limit the intrinsically high computing requirements of inverse problems, we focus on a subregion of the white matter shown in main Fig. 2a.

In the following, we describe how this data is processed further to obtain patient-specific finite element meshes to generate synthetic test data by simulation.

S1.2 Synthetic data

We use the surface meshes created during the brain segmentation with FreeSurfer[2] to create finite element meshes of the full brain. In detail, the first step in the mesh generation pipeline is to load Freesurfer brain surfaces into SVMTK[3], a Python library based on CGAL[4], for semi-automated removal of defects and creation of high quality finite element meshes. Details on SVMTK and the mesh generation procedure can be found in[3].

Using FEM we then solve the PDE (1) with boundary and initial conditions (8), (9) with a diffusion coefficient $D_0 = 0.36\,\mathrm{mm}^2\,\mathrm{h}^{-1}$ for the domain Ω being the whole brain. This value for the diffusion coefficient of gadubutrol was estimated in[1] from diffusion tensor imaging (DTI). In detail, we discretize (1) using the Crank-Nicolson scheme and use integration by parts to transform (1) into a variational problem that is solved in FEniCS[5] with continuous linear Lagrange elements. We use a high resolution mesh with 3×10^5 vertices (10^6 cells) and small time step of 16 min. In combination with the Crank-Nicolson scheme, this minimizes effects of numerical diffusion. For the initial condition (9) we assume no tracer inside the brain at $t = 0$, i.e. $c_0 = 0$. The boundary condition (8) is assumed to be spatially homogeneous while we let it vary in time as

$$g(t) = \begin{cases} 2t/T & \text{for } 0 \le t \le T/2 \\ 2 - 2t/T & \text{for } T/2 \le t \le T. \end{cases} \tag{S1}$$

This choice leads to enrichment of tissue similar to what is observed experimentally over the timespan of $T = 46$ hours. Finally, we interpolate the finite element solution $c(x,t)$ between mesh vertices and evaluate it at the center coordinates x_{ijk} of the voxels ijk inside the region of interest Ω and store the resulting concentration arrays c_{ijk} at 0, 7, 24 and 46 hours. With this downsampling procedure, we are then able to test the methods within the same temporal and spatial resolution as available from MRI. Finally, we remove all the voxels that are not within our white matter subdomain of interest Ω.

S1.3 Synthetic data with artifical noise

We test the susceptibility of the methods with respect to noise by adding to the data perturbations drawn randomly from the normal distribution $\mathcal{N}(0,\sigma^2)$. We refer to the standard deviation σ as noise level hereafter. Since negative values for the concentration c are nonphysical, we threshold negative values to 0, i.e. the noise-corrupted voxel values are computed as

$$c_{ijk} = \max\{0, c_{ijk} + \eta\} \quad \text{where} \quad \eta \sim \mathcal{N}(0,\sigma^2). \tag{S2}$$

In all the results presented in this work, we choose $\sigma = 0.05$. This corresponds to 5 % of the maximum value of $c = 1$ in the simulated measurements c_{ijk} and allows to reproduce some of the characteristic difficulties occurring when applying the PINN to the clinical data considered here.

S2 Assessing the validity of assuming a constant diffusion coefficient

We here provide arguments to motivate our modeling assumption of a scalar diffusion coefficient that is spatially constant in the region of interest Ω.

S2.1 Using tensor valued spatially varying diffusivity has little influence on forward simulations of tracer

In this section we assess the sensitivity of simulated tracer concentration with respect to two different modeling choice for the diffusivity D.

To this end, we use the diffusion tensor image (DTI) available for the patient under consideration in this work and use it to estimate the spatially varying diffusion tensor $\mathsf{D}(x) \in \mathbb{R}^{3\times 3}$ for the gadobutrol tracer as described in[1]. An illustration of the mean apparent diffusion coefficient $\frac{1}{3}\mathrm{tr}\mathsf{D}(x)$ can be found in Fig. S1d.

We now use this diffusion tensor to perform forward simulations of tracer spreading into the patient's brain using FEM as described in Section S1.2. In detail, instead of solving the scalar diffusion equation (1) we solve

$$\partial_t c(x,t) = \nabla \cdot (\mathsf{D}(x)\nabla c(x,t)) \quad \text{for} \quad (x,t) \in \Omega \times (0,T) \tag{S3}$$
$$c(x,0) = 0 \quad \text{for} \quad x \in \Omega \tag{S4}$$
$$c(x,t) = g(x,t) \quad \text{for} \quad (x,t) \in \partial\Omega \times (0,T) \tag{S5}$$

for the two distinct choices of $\mathsf{D}(x)$ stated below. Here, the domain Ω is set to be the whole brain. The initial condition is zero as in Section S1.3, but here we use a linear interpolation of data as boundary condition g. In detail, we define the boundary condition as

$$g^d(x,t) = c_i^d(x) + (c_{i+1}^d(x) - c_i^d(x))\frac{t-t_i}{t_{i+1}-t_i} \quad \text{for} \quad t_i \le t \le t_{i+1} \tag{S6}$$

where $t_i = \{0,6,24,46\}\,\mathrm{h}$ are the observation times and c_i^d is the tracer estimate from MRI at time t_i.

Model 1: Tensor valued diffusivity. Here, we directly use the spatially varying diffusion tensor

$$\mathsf{D}(x) \in \mathbb{R}^{3\times 3} \tag{S7}$$

for gadobutrol as obtained from DTI to solve PDE (1).

Model 2: Constant scalar diffusivity in white and gray matter. For this model, we compute regional mean apparent diffusion coefficients

$$\overline{D} = \frac{1}{3}\frac{1}{|\Omega|}\int_\Omega \mathrm{tr}\mathsf{D}(x)\,\mathrm{d}x. \tag{S8}$$

We consider two regions, white and gray matter, and obtain

$$\overline{D}_w = 0.42 \pm 0.19\,\mathrm{mm^2 h^{-1}} \quad \overline{D}_g = 0.46 \pm 0.21\,\mathrm{mm^2 h^{-1}}. \tag{S9}$$

The PDE (S5) is then solved with

$$\mathsf{D}(x) = D(x)\mathbb{1}; \quad D(x) = \begin{cases} \overline{D}_g & \text{for } x \in \text{ gray matter} \\ \overline{D}_w & \text{for } x \in \text{ white matter} \end{cases} \tag{S10}$$

where $\mathbb{1}$ denotes the identity matrix.

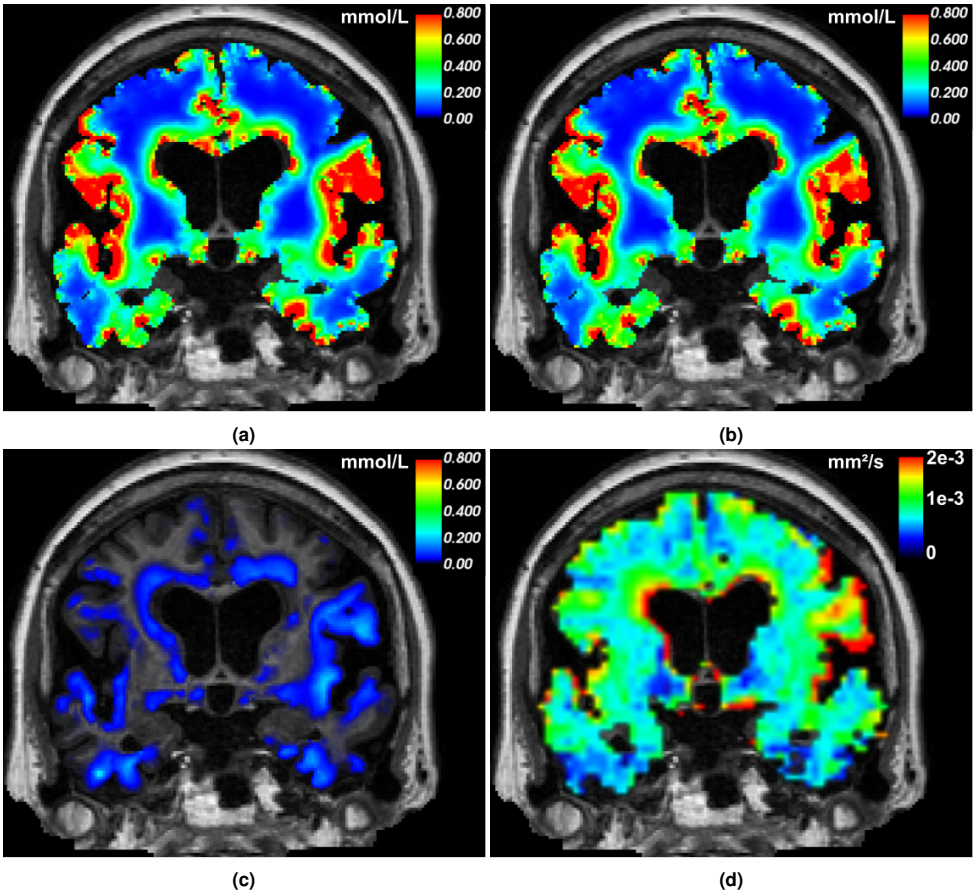

Figure S1. (a) Simulated tracer after 24 h obtained with DTI based Model 1 (S7). (b) Simulated tracer after 24 h obtained with scalar diffusion Model 2 (S10). The difference between (a) and (b) is barely visible to the eye, and the absolute difference is shown in (c) using the same scale. (d) the mean diffusivity $\frac{1}{3}\mathrm{trD}$.

In Fig. S1a and S1b we exemplarily display visualizations of the simulated tracer after 24 h (where the amount of tracer reaches its maximum in clinical observations) for both models. The difference is barely visible to the eye, and the relative ℓ^1-error between the tracer at 24 h simulated with the two models is only 8.8 %. Hence, it can not be expected that in an inverse setting with three snapshots of real data one can reliably differentiate by which of these two diffusion models the tracer distribution observed with MRI is governed.

S2.2 DTI characteristics suggest nearly isotropic diffusion

We next present some details on the diffusion tensor image available for the patient under consideration in this work. Figure S2a illustrates the fractional anisotropy

$$FA = \frac{3}{2}\frac{(\lambda_1 - MD)^2 + (\lambda_2 - MD)^2 + (\lambda_3 - MD)^2}{\lambda_1^2 + \lambda_2^2 + \lambda_3^2} \in [0,1] \tag{S11}$$

where

$$MD = \frac{1}{3}\mathrm{trD} \tag{S12}$$

is the mean diffusivity and λ_i, $i = 1,2,3$ are the eigenvalues of the diffusion tensor. It can be seen that the FA is rather small in most of the brain, in fact the mean $FA \approx 0.25$. The minimum value $FA = 0$ corresponds to isotropic diffusion, while $FA = 1$ corresponds to diffusion restricted to only one direction. Hence the value $FA \approx 0.25$ is in line with our assumption of a scalar, constant diffusion coefficient. Figure S2b further illustrates the distribution of eigenvalues in our region of interest. It can be seen that the ratio between largest and smallest eigenvalue is roughly 1.8, further justifying our modeling assumption of isotropic diffusion.

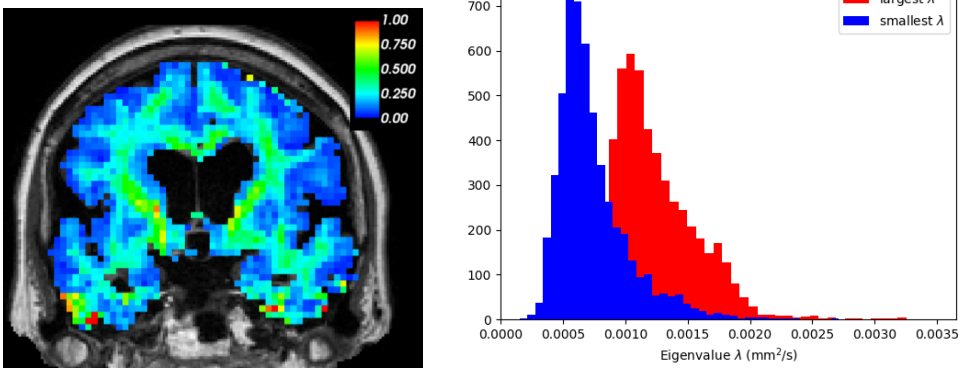

(a) **(b)**

Figure S2. (a) Fractional anisotropy and (b) distribution of smallest and largest eigenvalues in our domain of interest Ω for the diffusion tensor image.

S3 Hyperparameter settings

In our PINN approach, we model $c : (x,t) \to \mathbb{R}, x \in \mathbb{R}^3$, $t \in [0,T]$ by a feedforward neural network with 9 hidden layers and 64 neurons in each layer and hyperbolic tangent as activation function together with Glorot initialization[6] for all results presented here. We have also experimented with larger networks, different and adaptive activation functions but have not observed significant differences for a range of choices in terms of convergence rates or accuracy. We note that since the raw data is already a 3-D array representing grid structured data, using (physics-informed) convolutional neural networks instead of fully connected networks might yield benefits such as training speed up. In this work, however, we decide to focus on tuning the loss function formulation and find that using a fully connected network in combination with a properly tuned loss function yields results that are consistent with the FEM approach.

The network furthermore has an input normalization layer with fixed parameters to normalize the inputs to the range $[-1,1]$. To set these weights, we first compute the smallest bounding box containing all points $x = (x_1,x_2,x_3) \in \Omega$ to obtain lower and upper bounds l_i, u_i, $i = 1,2,3$ such that $l_i \leq x_i \leq u_i$ for all $x \in \Omega$. The first layer normalizes the inputs as

$$t \hookleftarrow 2\frac{t}{T} - 1,\ x_i \hookleftarrow 2\frac{x_i - l_i}{u_i - l_i} - 1 \tag{S13}$$

for $i = 1,2,3$ and with $T = 46\,\text{h}$ (last MRI acquisition timepoint).

If not stated otherwise, we use $N_p = 10^6$ space-time points (x_1,x_2,x_3,t) for the evaluation of the PDE loss (4). We found that this number was either sufficiently high to reach accurate recovery of the diffusion coefficient, or more sophisticated refinement techniques like residual-based adaptive refinement (RAR)[7] were needed instead of simply using more PDE points. The samples for the spatial coordinates x_1,x_2,x_3 are generated by first drawing a random voxel i inside Ω. The voxel center coordinates (x_1^i,x_2^i,x_3^i) are then perturbed to obtain $x_1 = x_1^i + dx$ where x_1^i is the x_1-coordinate of the center of a randomly drawn voxel i, and similarly for x_2 and x_3. The perturbation dx is drawn from the uniform distribution $\mathcal{U}([-0.5\,\text{mm}, 0.5\,\text{mm}])$ and ensures that (x_1,x_2,x_3) lies within the voxel i (the voxels correspond to a volume of $1\,\text{mm}^3$). The values for t are chosen from a latin hypercube sampling strategy over the interval $[0,T]$. We furthermore normalize the input data c^d by the maximum value such that $0 \leq c^d \leq 1$. In both the simulation dataset and the MRI data considered here, we use four images and the same domain Ω. The binary masks describing Ω consist of roughly 0.75×10^4 voxels, i.e., the four images (at 0, 7, 24 and 46 hours) yield a total of $N_d = 3 \times 10^5$ data points. Due to the large number of data and PDE points, we use minibatch sampling of the PINN loss function (4) and minimize it using the ADAM optimizer[8]. The learning rate η as well as potential learning rate decay schemes are an important hyperparameter, and we specify the used values in each section. The training set is divided into 20 batches, corresponding to 10^4 and 5×10^4 samples per minibatch in the data and PDE loss term, respectively.

Details on the implementation of the minibatch sampling strategy are presented in Section S5. It is worth noting here that our main reason to use minibatch sampling are not memory limitations. The graphics processing units (NVIDIA A100-SXM4) that we use to train the PINN have 80 GB of memory. This is enough to minimize the PINN loss function (4) with $N_d = 3 \times 10^5$ and $N_p = 10^6$ data and PDE loss points in a single batch. Our reason to use minibatch sampling is that the stochasticity of minibatch gradient descent helps to avoid local minima, see, e.g., Chapter 8 in[9]. In Section S4 below we perform a systematic study using different minibatch sizes and find that smaller batch sizes are preferable in our setting since they yield more accurate recovery of the diffusion coefficient (for a fixed number of epochs).

As for the finite element approach, we discretize (1) in time using the Crank-Nicolson scheme and 48 time steps. We then formulate the PDE problem as variational problem and solve it in FEniCS[5] using the finite element method. To limit the compute times required, we use a time step size of 1 h and continuous linear Lagrange elements. We further use linear interpolation of the data as a starting guess for the boundary control g,

$$g(x,t) = c^d(x,t_i) + \frac{c^d(x,t_{i+1}) - c^d(x,t_i)}{t_{i+1} - t_i}(t - t_i) \tag{S14}$$

for $t_i \in \mathcal{T} = \{0,7,24,46\}\,\text{h}$ and $t_i \leq t \leq t_{i+1}$. We then use dolfin-adjoint[10] to compute gradients of the functional (7) with respect to D and g and optimize using the L-BFGS method.

In terms of degrees of freedom (optimization parameters), these settings result in 33665 weights in the neural network. For the finite element approach, the degrees of freedom depend on the number of vertices on the boundary of the mesh since the control is the boundary condition g. Our mesh for Ω has 33398 cells on the boundary. For 48 time steps, this yields $48 \times 33398 = 1.6 \times 10^6$ degrees of freedom.

S4 Validation on synthetic data

We verify the implementation of the two approaches by considering synthetic data without noise, cf. Fig. 2b, in the white matter subregion Ω depicted in Fig. 2a.

Table S1. Iterations needed for convergence with both approaches on the different data sets tested in this study. Numbers in brackets indicate typical values for the compute times.

	synthetic with noise	MRI data
FEM	1,000 (45-50 h)	1,000 (45-50 h)
PINN	20,000 (3 h)	100,000 (20 h for RAR, 15 h for RAE)

For the PINN approach we test different minibatch sizes for three different optimization schemes using the ADAM optimizer: (i) fixed learning rate 10^{-3} and $p = 2$, (ii) fixed learning rate 10^{-3} while we switch from $p = 2$ to $p = 1$ after half the epochs and (iii) using initial learning rate 10^{-3} that decays exponentially during training to 10^{-4} and $p = 2$. Table S2 tabulates the relative error between the learned diffusion coefficient and the ground truth D_0 for a wide range of parameters. We find that (a) in general smaller batch sizes result in more accurate results and (b) the results are both most stable and accurate when using exponentially decaying learning rate. Notably, the PINN recovers the ground truth diffusion coefficient D_0 to up to 1 % accuracy when using the learning rate decay optimization scheme. These result are in line with[11] where increased accuracy in parameter recovery was observed for smaller batch sizes. However, there are also settings where full batch optimization with L-BFGS improves PINN performance in parameter identification problems[12].

For the finite element approach, Table S3 presents the accuracy of the recovered diffusion coefficient. According to the theoretical results, decreasing regularization parameters leads to higher accuracy but less well conditioned optimization problems. This is in line with the results presented in Table S3. The finite element approach with appropriate regularization parameters and the PINN approach yield comparably accurate results.

S4.1 Computational effort

We here list the computing times to estimate the diffusion coefficient with our implementation of the FEM and PINN approaches presented in the main text. It should be noted that neither of these implementations have been optimized to reduce the compute times, and that the times required for convergence vary between datasets.

Our implementation of the FEM approach using dolfin-adjoint[10] with a mesh containing 91849 cells and 23307 vertices (whereof 33398 and 16693 are on the boundary, respectively) requires around 45-48 hours computing time on noisy synthetic data for the 1,000 iterations until convergence as shown in Supplementary Fig. S3a using a single Intel Xeon Gold CPU. As for the PINN approach, on noisy synthetic data, convergence was achieved when terminating the optimization after 20,000epochs of ADAM with data and PDE batch sizes of 1.5×10^4 and 5×10^4, respectively. With our implementation in PyTorch[13] this takes about 3 hours on a NVIDIA A100-SXM4.

As for training on real MRI data, the FEM approach was usually converged after 1,000 iterations as well, while the PINN approach required lower learning rate and thus more epochs. The PINN results presented in the text were obtained after 100,000 epochs which usually was sufficient to converge. The compute time varies between sampling strategies (for PINNs) and workload on the cluster node for the particular simulation (for both approaches). For PINNs, the compute time was around 20 h for RAR and 15 h for RAE. The results are sumarized in S1.

We have also performed additional numerical experiments where we use residual based adaptive exchange and train with both ADAM and L-BFGS optimizer after every refinement. This strategy is similar to[14]. It emerges that a combination of low learning rates for ADAM, adaptive residual based refinement and ℓ^1 norm for the PDE loss allows us to successfully train with a combination of Adam + L-BFGS. The results after training with ADAM + L-BFGS are consistent with the ADAM results reported in the manuscript, while roughly half the optimization time is required.

S4.2 PINN solution of the synthetic testcase

Table S2. Average rel. error $|D_{\text{pinn}} - D_0|/D_0$ in % after 2×10^4 epochs training on synthetic data without noise, with Algorithm 1. We average over 5 runs, numbers in brackets are standard deviation.

Optimization scheme	n_r \ n_d	10^4	5×10^4	10^5
ADAM lr = 1e-3 $p = 2$	10000	2 (0)	2 (1)	3 (1)
	33334	4 (0)	12 (6)	9 (1)
	50000	7 (1)	5 (0)	2 (0)
	100000	7 (1)	55 (18)	59 (18)
	166667	8 (1)	24 (17)	50 (23)
	333334	8 (1)	38 (4)	50 (16)
ADAM lr = 1e-3 p=2 $\rightarrow$ p=1	10000	2 (0)	1 (0)	2 (0)
	33334	2 (0)	2 (0)	2 (0)
	50000	2 (1)	2 (0)	2 (1)
	100000	2 (1)	58 (27)	50 (25)
	166667	2 (1)	3 (2)	68 (4)
	333334	2 (0)	0 (0)	62 (6)
ADAM exp lr decay 1e-3 $\rightarrow$ 1e-4 $p = 2$	10000	1 (0)	1 (0)	1 (0)
	33334	1 (0)	1 (1)	1 (0)
	50000	1 (1)	1 (0)	1 (0)
	100000	1 (0)	10 (6)	72 (0)
	166667	1 (1)	4 (2)	23 (26)
	333334	1 (0)	4 (4)	59 (23)

S4.3 Finite element solution of the synthetic testcases

Table S3. Rel. error $|D - D_0|/D_0$ for the FEM approach (7), different regularization parameters, 3 measurement points, clean data, 1,000 iterations. Convergence of the optimization is demonstrated in Fig. S3a.

α	β \ γ	0.0	0.01	1.0
10^{-6}	0.001	9	8	261
	0.01	1	5	261
	0.1	11	10	261

Table S4. Rel. error $|D - D_0|/D_0$ in % for the finite element approach (7), different regularization parameters and parameterizations $D(\delta)$. Failure of the algorithm is indicated by the symbol "x". Convergence plots for the optimization are given in Fig. S3b.

Parameterization		$D = \delta$ (11)		$D = D(\delta)$ (10)	
α	β \ γ	0.0	0.01	0.0	0.01
10^{-6}	0.0	43	10	35	2
	0.01	8	x	16	8
	0.1	4	x	3	11
10^{-4}	0.0	44	x	6	20
	0.01	5	13	2	14
	0.1	6	12	5	12

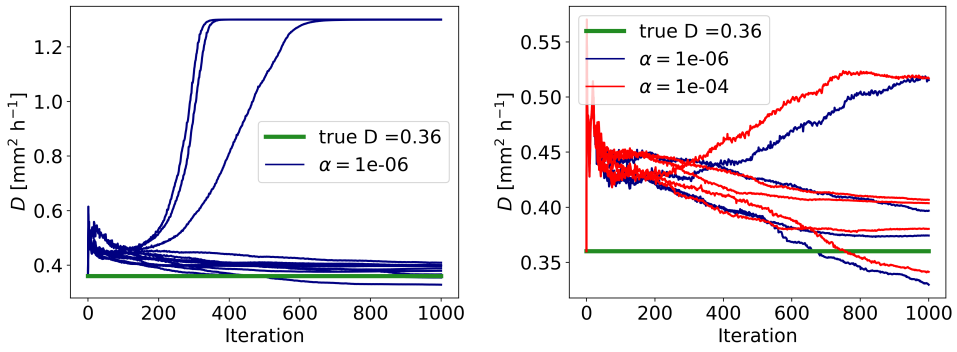

Figure S3. Convergence plots for the FEM regularization parameters presented in Tables S3 (synthetic data) and S4 (synthetic data with noise). Different lines correspond to different combinations of regularization parameters $(\beta,\gamma)=\{0.001,0.01,0.1\}\times\{0,0.01,1\}$ and $\{0,0.01,0.1\}\times\{0,0.01\}$ tested for synthetic and noisy synthetic data, respectively.

S5 Details on the PINN training procedures

S5.1 Minibatch sampling strategy

Algorithm 1 Minibatch training

Input: neural network c with parameters θ, data minibatch size n_d, PDE minibatch size n_r, RAR checkpoints $\{i_1,\dots,i_n\}$, epochs, learning rate η, initial guess D for the diffusion coefficient, input-data pairs $\{(\mathbf{x}_k^d,c_k^d)\in\mathbb{R}^4\times\mathbb{R}\}_{1\le k\le N_d}$, PDE space-time points $\mathcal{P}=\{\mathbf{x}_k\in\mathbb{R}^4\}_{1\le k\le N_r}$

compute number of data batches b_d =ceil(N_d/n_d)
compute number of PDE batches $b_r=$ ceil(N_r/n_r)
Set b =max(b_d,b_r)
for i in range(epochs) **do**
  if i $\in$ RAR checkpoints **then**
    add points to $\mathcal{P}$ with either procedure 2 or 3
  end if
  randomly split $\{(\mathbf{x}_k^d,c_k^d)\}$ into subsets $\mathcal{D}_{1\le j\le b_d}$
  randomly split $\{\mathbf{x}_r^k\}$ into subsets $\mathcal{R}_{1\le j\le b_r}$
  # Iterate over all minibatches
  for j in range(b) **do**
    # Start from beginning should you reach the last subset in $\mathcal{D}_{b_k}$ or $\mathcal{R}_{b_r}$, respectively (Happens if $b_r\neq b_d$):
    Set $j_d=j \bmod b_d$, $j_r=j \bmod b_r$
    # Compute losses on subsets
    $\mathcal{L}=\frac{1}{|\mathcal{R}_{j_d}|}\sum_{\mathbf{x}^d,c^d\in\mathcal{D}_{j_d}}\left(c(\mathbf{x}^d)-c^d\right)^2$
    $\mathcal{L}$ += $\frac{1}{|\mathcal{R}_{j_r}|}\sum_{\mathbf{x}\in\mathcal{R}_{j_r}}|\partial_t c(\mathbf{x})-D\Delta c(\mathbf{x})|^p$
    # update parameters θ
    θ -= $\eta\nabla_\theta\mathcal{L}$
    # update diffusion coefficient D
    D -= $\eta\nabla_D\mathcal{L}$
  end for
end for

S5.2 Residual based refinement

Algorithm 2 Refinement step with the RAR procedure as in "Procedure 2.2" in[7] adapted to the nomenclature in our work.

Input: The set of N_r PDE points $\mathcal{P}$, PDE residual $r(x,t)$, number m of points to add per refinement step, number n of points to test the residual

Output: refined set of PDE points $\mathcal{P}$

1: Compute the absolute value of the PDE residual $|r(x,t)|$ at n random samples $\mathcal{S} = \{(x_1,t_1),\ldots,(x_n,t_n)\}$ from $\Omega_r \times \tau$
2: Sort $\mathcal{S}$ by decreasing residual $|r(x,t)|$ and keep only the first m points in $\mathcal{S}_m$
3: **return** The refined set of $N_r + m$ points $\mathcal{P} \cup \mathcal{S}_m$

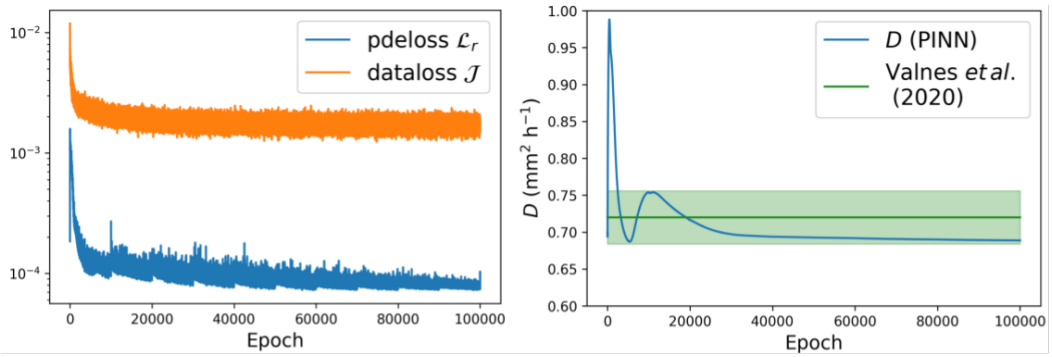

Figure S4. (Left) Convergence plots for the PINN losses trained with RAR on MRI data. (Right) Diffusion coefficient during PINN training. Exponential learning rate decay from 10^{-4} to 10^{-5} with RAR and $p = 1$.

Algorithm 3 Refinement step with the RAE procedure, a modification of the RAR procedure as described under "Procedure 2.2" in[7].

Input: The set of N_r PDE points $\mathcal{P}$, PDE residual $r(x,t)$, number m of points to add per refinement step, number n of points to test the residual

Output: refined PDE points $\mathcal{P}$

1: Compute the absolute value of the PDE residual $|r(x,t)|$ at n random samples $\mathcal{S} = \{(x_1,t_1),\ldots,(x_n,t_n)\}$ from $\Omega_P \times \tau$
2: Sort $\mathcal{S}$ by decreasing residual $|r(x,t)|$ and keep only the first m points in $\mathcal{S}_m$
3: Compute the PDE residual $|r(x,t)|$ at the points in $\mathcal{R}$
4: Sort $\mathcal{R}$ by increasing residual $|r_{\mathcal{R}}(x,t)|$ and keep only the first $N_r - m$ points in $\mathcal{R}_{N_r-m}$
5: **return** The set of N_r refined points $\mathcal{R}_{N_r-m} \cup \mathcal{S}_m$

References

1. Valnes, L. M. *et al.* Apparent diffusion coefficient estimates based on 24 hours tracer movement support glymphatic transport in human cerebral cortex. *Sci. Reports* **10**, 9176, DOI: 10.1038/s41598-020-66042-5 (2020). Number: 1 Publisher: Nature Publishing Group.

2. Fischl, B. FreeSurfer. *NeuroImage* **62**, 774–781, DOI: 10.1016/j.neuroimage.2012.01.021 (2012).

3. Mardal, K.-A., Rognes, M. E., Thompson, T. B. & Valnes, L. M. Simulating Anisotropic Diffusion in Heterogeneous Brain Regions. In Mardal, K.-A., Rognes, M. E., Thompson, T. B. & Valnes, L. M. (eds.) *Mathematical Modeling of the Human Brain: From Magnetic Resonance Images to Finite Element Simulation*, Simula SpringerBriefs on Computing, 97–107, DOI: 10.1007/978-3-030-95136-8_6 (Springer International Publishing, Cham, 2022).

4. Project, T. C. *{CGAL} User and Reference Manual* (CGAL Editorial Board, 2022), 5.4 edn.

5. Alnæs, M. *et al.* The fenics project version 1.5. *Arch. Numer. Softw.* **3** (2015).

6. Glorot, X. & Bengio, Y. Understanding the difficulty of training deep feedforward neural networks. In *Proceedings of the Thirteenth International Conference on Artificial Intelligence and Statistics*, 249–256 (JMLR Workshop and Conference Proceedings, 2010). ISSN: 1938-7228.

7. Lu, L., Meng, X., Mao, Z. & Karniadakis, G. E. DeepXDE: A deep learning library for solving differential equations. *SIAM Rev.* **63**, 208–228, DOI: 10.1137/19M1274067 (2021). Publisher: Society for Industrial and Applied Mathematics.

8. Kingma, D. P. & Ba, J. Adam: A Method for Stochastic Optimization. *arXiv:1412.6980 [cs]* (2017). ArXiv: 1412.6980.

9. Goodfellow, I., Bengio, Y. & Courville, A. *Deep Learning* (MIT Press, 2016). http://www.deeplearningbook.org.

10. Mitusch, S. K., Funke, S. W. & Dokken, J. S. dolfin-adjoint 2018.1: automated adjoints for FEniCS and Firedrake. *J. Open Source Softw.* **4**, 1292, DOI: 10.21105/joss.01292 (2019).

11. Kadeethum, T., Jørgensen, T. M. & Nick, H. M. Physics-informed neural networks for solving inverse problems of nonlinear biot's equations: Batch training. In *54th US Rock Mechanics/Geomechanics Symposium* (OnePetro, 2020).

12. Mathews, A. *et al.* Uncovering turbulent plasma dynamics via deep learning from partial observations. *Phys. Rev. E* **104**, 025205, DOI: 10.1103/PhysRevE.104.025205 (2021).

13. Paszke, A. *et al.* Pytorch: An imperative style, high-performance deep learning library. *Adv. neural information processing systems* **32** (2019).

14. Wu, C., Zhu, M., Tan, Q., Kartha, Y. & Lu, L. A comprehensive study of non-adaptive and residual-based adaptive sampling for physics-informed neural networks. *arXiv preprint arXiv:2207.10289* (2022).

Paper II

Human brain solute transport quantified by glymphatic MRI-informed biophysics during sleep and sleep deprivation

Vegard Vinje, Bastian Zapf, Geir Ringstad, Per Kristian Eide, Marie E. Rognes, Kent-Andre Mardal

Submitted for publication

II

Paper III

Medical Image Registration using optimal control of a linear hyperbolic transport equation with a DG discretization

Bastian Zapf, Johannes Haubner, Lukas Baumgärtner, Stephan Schmidt

Submitted for publication

III

Paper IV

Quantifying cerebrospinal fluid tracer concentration in the brain

Bastian Zapf, Lars Magnus Valnes, Kent-Andre Mardal

Book chapter under revision for *MRI2FEM II: from magnetic resonance images to computational brain mechanics*, Simula Springer Briefs on Computing

IV